國立臺灣海洋大學

河海工程學系

碩士學位論文

指導教授：陳正宗 終身特聘教授

映像法於含圓及球形邊界拉普拉斯問題格林
函數之研究

A Study on the Green's functions for Laplace problems with circular and spherical boundaries by using the image method

研究生：謝宏治 撰

中華民國 98 年 7 月

映像法於含圓及球形邊界拉普拉斯問題格林函數
之研究

A Study on the Green's functions for Laplace problems with circular and spherical boundaries by using the image method

研 究 生：謝宏治　　　　Student：Hung-Chih Shieh

指導教授：陳正宗　　　　Advisor：Jeng-Tzong Chen

國 立 臺 灣 海 洋 大 學
河 海 工 程 學 系
碩 士 論 文

A Thesis
Submitted to Department of Harbor and River Engineering
College of Engineering
National Taiwan Ocean University
In Partial Fulfillment of the Requirements
for the Degree of
Master of Science
in
Harbor and River Engineering
July 2009
Keelung, Taiwan, Republic of China

中 華 民 國 98 年 7 月

國 立 臺 灣 海 洋 大 學

博碩士論文紙本及全文上網授權書

（提供授權人裝訂於紙本論文書名頁之次頁用）

本授權書所授權之論文為授權人在國立臺灣海洋大學
河海工程學系＿＿＿＿＿＿＿＿組 97 學年度第＿＿＿學期取得碩士學位之論文。

記錄編號：G0M96520027
論文題目：映像法於含圓及球形邊界拉普拉斯問題格林函數之研究
指導教授：陳正宗

茲同意將授權人擁有著作權之上列論文全文電子檔(含摘要)，依下述授權範圍，以非專屬、無償授權國立臺灣海洋大學圖書館，不限地域、時間與次數，以微縮、光碟或其他各種數位化方式將上列論文重製，並得將數位化之上列論文及論文電子檔以上載網路方式，提供讀者基於個人非營利性質之線上檢索、閱覽、下載或列印。

■ 讀者基於非營利性質之線上檢索、閱覽、下載或列印上列論文，應依著作權法相關規定辦理。

論文全文上載網路公開之範圍及時間：

校內區域網路	■ 立即公開
校外網際網路	■ 立即公開
紙本公開陳列範圍及時間：	■ 茲同意將本著作立即公開陳列上架，並同意因遺失或損毀重製。

授 權 人：謝宏治
學　　　號：M96520027
E-mail ：M96520027@mail.ntou.edu.tw
親筆簽名或蓋章：＿＿＿＿＿＿＿＿＿＿＿＿＿＿＿
中　華　民　國　　　　年　　　月　　　日

國家圖書館
博碩士論文電子檔案上網授權書

本授權書所授權之論文爲授權人在國立臺灣海洋大學河海工程學系 97 學年度第＿＿＿學期取得碩士學位之論文。

記錄編號：GOM96520027
論文題目：映像法於含圓及球形邊界拉普拉斯問題格林函數之研究
指導教授：陳正宗

茲同意將授權人擁有著作權之上列論文全文（含摘要），非專屬、無償授權國家圖書館，不限地域、時間與次數，以微縮、光碟或其他各種數位化方式將上列論文重製，並得將數位化之上列論文及論文電子檔以上載網路方式，提供讀者基於個人非營利性質之線上檢索、閱覽、下載或列印。

☐ 上列論文爲授權人向經濟部智慧財產局申請專利之附件或相關文件之一（專利申請案號：　　　　　　　　　　　），請於　　年　　月　　日後再將上列論文公開或上載網路。

☐ 因上列論文尚未正式對外發表，請於　　年　　月　　日後再將上列論文公開或上載網路。

授權人：謝宏治

親筆簽名及蓋章：＿＿＿＿＿＿＿＿＿＿＿　　　民國　　年　　月　　日

身分證字號：H123317622
電話：　　　　　　　傳真：
聯絡地址：桃園縣平鎮市湧豐里2鄰中豐路山頂段90巷29號
E-Mail：M96520027@mail.ntou.edu.tw

謝 誌

　　七百多天的日子即將進入了尾聲，回想初來乍到的樣子，那時候對於當一個研究生是既期待又害怕，就在這樣的心情之下進入了力學聲響振動實驗室中，在這兩年的求學過程之中讓我受到最多影響的莫過於 陳正宗 終身特聘教授，從老師對於學問與研究的嚴謹態度都是以前我所欠缺的，因此在完成論文的同時我才了解到要寫出一個好的論文是需要以非常嚴謹的態度去面對。而除了作論文外對於其他的事物也應該如此；感謝老師在這兩年之中願意不辭辛勞的指導使我能夠了解到做研究的樂趣，除了學業外老師也常告訴我們好的身體是研究的基石，所以有空閒的時候老師常常會帶我們出去郊外爬山，老師與師母更常會帶好吃的點心來慰勞我們疲勞的胃。在研究所的日子中能夠進入力學聲響振動實驗室是我最值得也是最驕傲的決定。

態度決定高度，毅力決定能力；

登高必自卑，行遠必自邇。

　　論文口試的過程中，承蒙宜蘭大學土木工程系-李洋傑博士、中華大學土木與工程資訊系-呂志宗博士、宜蘭大學土木工程系-陳桂鴻博士、屏東科技大學教學資源中心-徐文信博士、中華技術學院機械工程系-李為民博士、高雄海洋科技大學造船工程系-陳義麟博士、中華技術學院航空機械系-呂學育博士以及本校河海工程系-岳景雲博士與范佳銘博士，不吝指教並提供寶貴的意見使文章能夠成為一本讓我自己驕傲的作品，在此深表謝意。

　　而在求學以及撰寫論文的過程中除了憑藉著自已的毅力與努力之外，更要感謝那些一路上給予我鼓勵與支持的人們：阿德與周董學長的幫忙讓我在學業及論文研究方面可以更加的事半功倍，讓我能有機會追隨學長們的背影來學習，更不能忘記初到基隆時的生活食宿問題也多虧了學長們的幫忙，真是非常感謝；不能不提到與我一起奮鬥努力的同窗好友兼師兄弟的羿州與聖凱(高手)，雖然常有人說研究是孤獨的，但是有你們的陪伴讓我得到了不一樣的體驗，或許將來還會懷念一同去吃宵夜以及一起熬夜寫作業、寫論文的時光；有了好的論文如果沒有可以發表的舞台也是枉然的，感謝建鋒、振鈞、胤祥、文哲及宇志在最後幫我們準備了最棒的舞台，讓口試委員與我能夠在最好的環境與狀態來討論本篇論文；圍捷、明修、豐任、小愛、毓玲、雅馨、雅鈞與佑勳，謝謝你們一路上的加油與鼓

ㄚ炎 Hung-Chih Shieh

2009/07/29 於力學聲響振動實驗室

Contents

Table captions

Figure captions

Notations

∇^2	Laplacian operator
$\delta(\mathrm{x}-\mathrm{s})$	Dirac-delta function
B	Boundary
$G(\mathbf{x},\mathbf{s})$	Green's function
D	Domain of interest
D^c	Complementary domain
R_s	Distance between the source point and ith center of the circle
ρ_i	Radius of the ith circle
r	distance between the source point s and the field point x, $$r \equiv |x-s|$$
s	Source point
x	Field point
(R_s,θ)	Polar coordinate of s
(ρ,ϕ)	Polar coordinate of x
θ	Polar angle measured with respect to the x direction
$U(\mathbf{x},\mathbf{s})$	Kernel function in the singular formulation
$U^I(\mathbf{x},\mathbf{s})$	Degenerate kernel function of $U(\mathbf{x},\mathbf{s})$ for $R_s \geq \rho$
$U^E(\mathbf{x},\mathbf{s})$	Degenerate kernel function of $U(\mathbf{x},\mathbf{s})$ for $\rho > R_s$
$u(s)$	Potential function at the source point s
$u(x)$	Potential function at the field point x
ξ	the curves are family of circular (sphere) passing through two focuses
η	The curve are family of circular (sphere)
s_{c1}, s_{c2}	Frozen image point
c_1, c_2	Focuses of bipolar (bispherical) coordinates
N	Number of the image point
R_i	Distance between the image source point and ith center of the circle
$c_1(N), c_2(N)$	The strengths of frozen image point
$e(N)$	The strengths of rigid body term
ε_m	The Neumann factor
w_i	The weighting of the kth image point
s_i	Number of the image source
α_j	The jth unknown coefficient of MFS

p_j	The weighting of Trefftz method
Φ_j	The *jth* T-complete function
N_T	The number of T-complete functions
c	The half distance between two focuses
r_{c1}, r_{c2}	Distance between the focus and circular (sphere) boundary
$T(\mathbf{x}, \mathbf{s})$	Kernel function in the singular formulation
$T^I(\mathbf{x}, \mathbf{s})$	Degenerate kernel function of $T(\mathbf{x}, \mathbf{s})$ for $R_s > \rho$
$T^E(\mathbf{x}, \mathbf{s})$	Degenerate kernel function of $T(\mathbf{x}, \mathbf{s})$ for $\rho > R_s$
$t(s)$	Normal derivative of $u(s)$ at s, $\dfrac{\partial u(s)}{\partial n_s}$
$t(x)$	Normal derivative of $u(x)$ at x, $\dfrac{\partial u(x)}{\partial n_x}$
n	Normal vector
n_s	Normal vector at the source point s
n_x	Normal vector at the field point x

中 文 摘 要

本論文以映像法求解含圓形及球形邊界拉普拉斯方程式之格林函數與無源點之邊界值問題。文中我們可將映像法視為基本解法(MFS)的一種特例，並透過映像法找出圓形與球形邊界問題的最佳點源位置。以二維同心圓環與三維同心圓球為例，透過加法定理來驗證 Trefftz 法及基本解法在數學上的等效性。此外，以三個二維的例子(偏心圓，半無限域含圓型孔洞與無限域含兩個圓型孔洞)說明，我們可以發現雙極座標系統的兩個焦點與映像法最後兩個凝固點的位置是一致的。同樣的，三維的例子中亦可找到映像法最後的凝固點與雙球座標系統之焦點的位置相同。關於三維映像法的點源強度，我們可透過基本解展開成退化核函數的形式來求得。最後，我們使用映像法求解二維及三維的對稱與反對稱邊界值問題。在三維的例子中，兩個位於球心的起始點未知強度可在一開始就由邊界條件決定。如果映射的組數夠多，最後兩個凝固映像點的強度將會趨近於零。然而，在二維的例子則完全不同，經由理論與數值計算其唯二非零強度就在兩個焦點上。

關鍵字: 映像法、格林函數、邊界值問題、拉普拉斯方程式、基本解法(MFS)、加法定理、Trefftz 法、雙極座標系統，退化核函數

Abstract

In this thesis, we solve the Green's function and boundary value problems (BVPs) without source for the Laplace equation with circular and spherical boundaries by using the image method. We find that the image method is a special case of the method of fundamental solutions (MFS), and the optimal locations of sources in the MFS can be determined by using the image method. The optimal locations are dependent on the source location and the geometry of problems. In the concentric sphere case, the solutions derived by the Trefftz method and the MFS are found to be mathematically equivalent by using the addition theorem. Moreover, it is found that final image points in the image method terminate at the two focuses of the bipolar coordinates for all the three cases of two-dimensional, an eccentric annulus, a half plane with a circular hole and an infinite domain with two circular holes. Similarly, it is found that the final two image locations freeze at the two focuses in the bispherical coordinates for the three-dimensional case where the weighting of image source can be determined by using the degenerate kernel. Finally, we solve the symmetrical and anti-symmetrical BVPs for the two and three dimensional cases by using the image method. For the three-dimensional case, we have found the strengths of the two initial sources at the two centers that can be determined by matching BC in advance, and the final strengths at the two strengths of frozen images approaches zero if the number of images becomes infinite. However, the two-dimensional case is not the same of the three-dimensional case, only two nonzero strengths are found at the two focuses after theoretical study and numerical calculate.

Keywords: image method, Green's function, boundary value problem (BVP), Laplace equation, method of fundamental solutions (MFS), addition theorem, Trefftz method, bipolar coordinates, degenerate kernel

Chapter 1 Introduction

1.1 Motivation of the research and literature review

The Green's function has been studied and applied in many fields by mathematicians as well as engineers [36, 48]. It's a long history that, many researchers studied the circular boundary value problems (BVPs), such as circular apertures and/or inclusions. As a result of the aforementioned consideration, many theoretical studies concerning the circular boundary problems in engineering problems have appeared in the literature. A number of problems in engineering problems can be modeled, such as the steady state heat conduction problem [23, 26], electrostatic potential [4, 5], torsion bar problems [9, 47], temperature in case of the displacement of an infinite medium under remote uniformly shear [1, 24, 29, 30, 31], velocity potential in a steady flow of an ideal fluid [3, 35, 45] and the pure torsion of an elastic bar by equilibrated end torques [9, 47] are examples in which the Laplace equation is satisfied; acoustics, membrane vibration [32] and water wave problems [20] governed by the Helmholtz equation; plate vibration [33, 34] and Stokes' flow [50] formulated by the biharmonic equation. The Laplace equation arises in many branches of physics, from which it recruits a wide group of researchers.

In order to solve engineering problems, researchers and engineers have paid more attention on the development of several numerical methods. Therefore, many numerical methods were developed such us the finite element method (FEM), the finite difference method (FDM), the boundary element method (BEM) and meshless method. The FEM given domain is viewed as a collection of subdomains, and over each subdomain the governing equation is approximated by any of the traditional variational methods. The main reason behind seeking approximate solution on a collection of subdomain is the fact that it is easier to represent a complicated function as a collection of geometrically simple subdomains. However, a few problems are not easy tasks for FEM that another numerical method, thus BEM is developed. The BEM uses Green's theorem to reduce

the dimensionality of the problem such as a 3-D problem is reduced to a surface problems, a surface problem is reduced to a line problem. In the recent years, the meshless method can avoid the singularity or hypersingularity problem of BEM. Meshless method does not need the conception of elements, it is mesh-free for a model creation to solve engineering problems. Figure 1-1 depicts the mesh of FEM, BEM and meshless method for two-dimensional domain. In the BEM, the method of fundamental solutions (MFS) and Trefftz method are one kinds of the meshless methods. Figure 1-2 shows the collocation point of the MFS and Trefftz method.

The main concern of this thesis is that the optimal location of the MFS sources can be obtained by using the image concept. The image method is a technique that is widely known to solve Green's function in theoretical physics [51]. When considering problems of obtaining Green's functions for a bounded domain, the reflection is described by one or successive image sources, and the position and sign of the image sources are chosen so that the boundary conditions can be satisfied [7]. A simple image method for one-dimensional string is demonstrated in Fig. 1-3. The image method is an approach to construct a Green's function for a part of domain bounded by planes, circles or spherical surface in terms of the corresponding fundamental solution in the full space. In certain cases, it is possible to obtain the exact solution for a concentrated source in a domain through superimposing the infinite plane or space solution for the given source and its image sources [38, 39]. The Greenberg's book introduced the image method to solve the Laplace problem with circular boundaries [27]. An anisotropic film-substrate system solution of the edge dislocation was solved by using the image method [59]. The image solution of dielectric plate problem was also obtained [55]. However, they all focused on the Green's function with plane or a circular (sphere) boundary only.

In this thesis, we obtain semi-analytical and analytical solutions of the Green's functions for Laplace problems with circular (spherical) boundaries by using the image method and bipolar (bispherical) coordinates system in conjunction with the addition theorem. In addition, we can link the image method and the MFS for Laplace problems by using the addition theorem. The analytical solutions of the three-dimensional problems were

derived by using the Trefftz method and the bispherical coordinate system, respectively. Also, the semi-analytical solutions were obtained by using the image method. The solutions derived by using the Trefftz method and MFS were proved to be mathematically equivalent for the 3-D case. Furthermore, it is found that final location of the image points terminate at the two focuses of the bipolar (bispherical) coordinates for both the two-dimensional and three-dimensional cases. Finally, not only Green's function but also BVPs without sources are considered.

1.2 Organization of the thesis

The frame of the thesis is shown in Fig. 1-4. In this thesis, we solve the Green's function and BVPs for the Laplace equation with circular and spherical boundaries by using the image method. We obtain the analytical solutions for two-dimensional and three-dimensional cases by using bipolar and bispherical coordinates, respectively.

In Chapter 2, we focus on the application in deriving the solution of the Green's function for the Laplace equation with circular boundaries by using the image method. The image method can be seen as a special case of the MFS with only at most four unknown strengths which are required to be determined. The optimal locations of sources in the MFS can be captured by using the image method and their positions are dependent on the source location and the geometry of problems. Moreover, it is found that final locations of image points in the image method terminate at the two focuses of the bipolar coordinates for all the two-dimensional cases.

In Chapter 3, an image solution is obtained for the Green's function with spherical boundaries. Furthermore, the mathematical equivalence between solutions derived by using the Trefftz method and the MFS for concentric spheres are examined. Also, the analytical solution is obtained by using the bispherical coordinates for the non-concentric spheres. Similarly, it is found that the final two images freeze at the two focuses in the bispherical coordinates for the three-dimensional cases as well as 2-D case in Chapter 2. In Chapter 4, we employ the image method to solve BVPs without sources. Not only 2-D and 3-D problems but also the symmetric and anti-symmetric

cases are considered. To verify the contour plot, analytical solutions by using bispherical and bipolar coordinates in the Lebedev et al.'s book [43] are compared with. Finally, we draw out some concluding remarks item by item and reveal some further topics in Chapter 5.
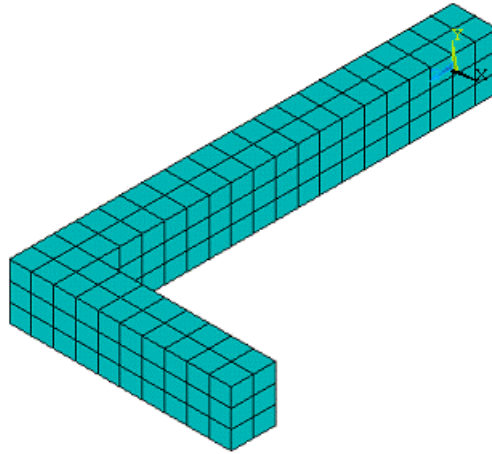
(a) FEM
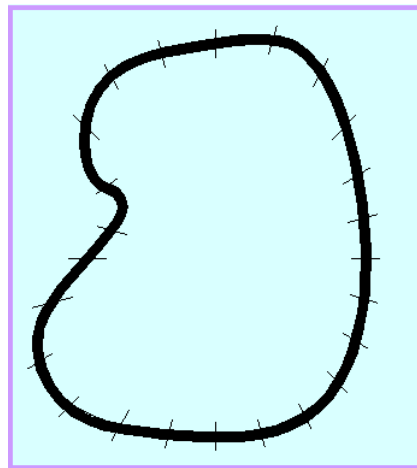
(b) BEM
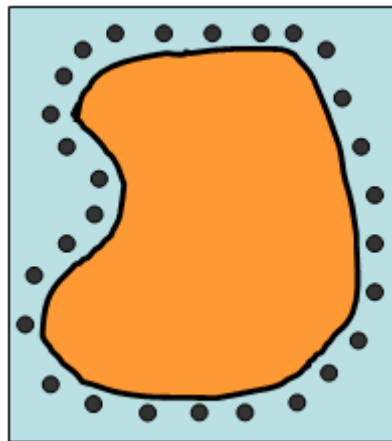
(c) meshless method

Fig. 1-1 Model creation by using (a) FEM, (b) BEM and (c) meshless method.
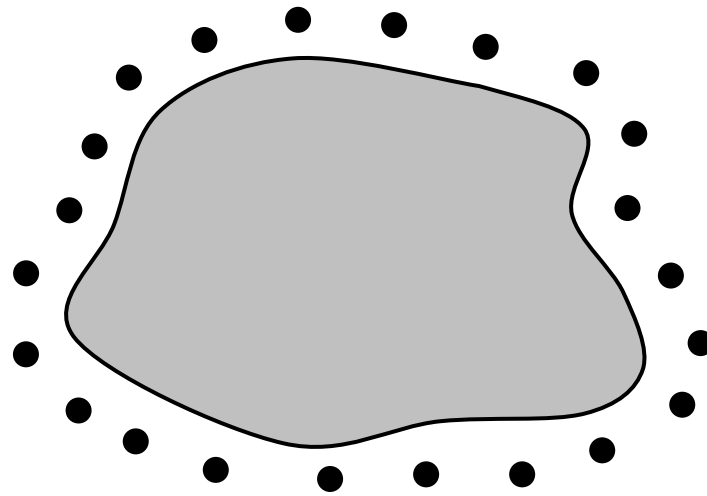
(a) MFS
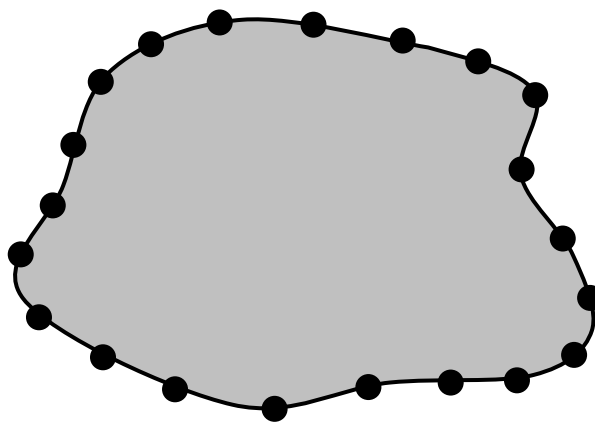
(b) Trefftz method

Fig. 1-2 The collocation point of the MFS and Trefftz method.
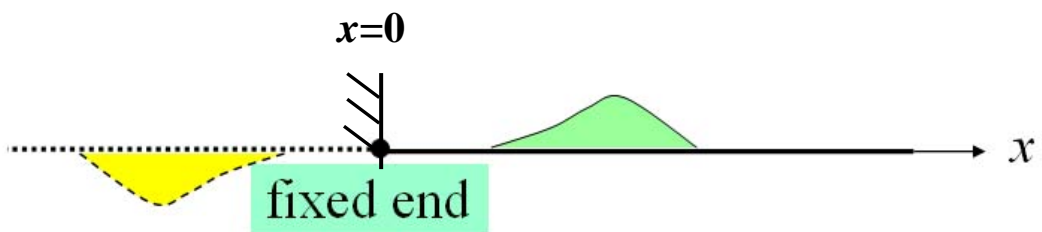
Fig. 1-3 A simple image method for one-dimensional string.
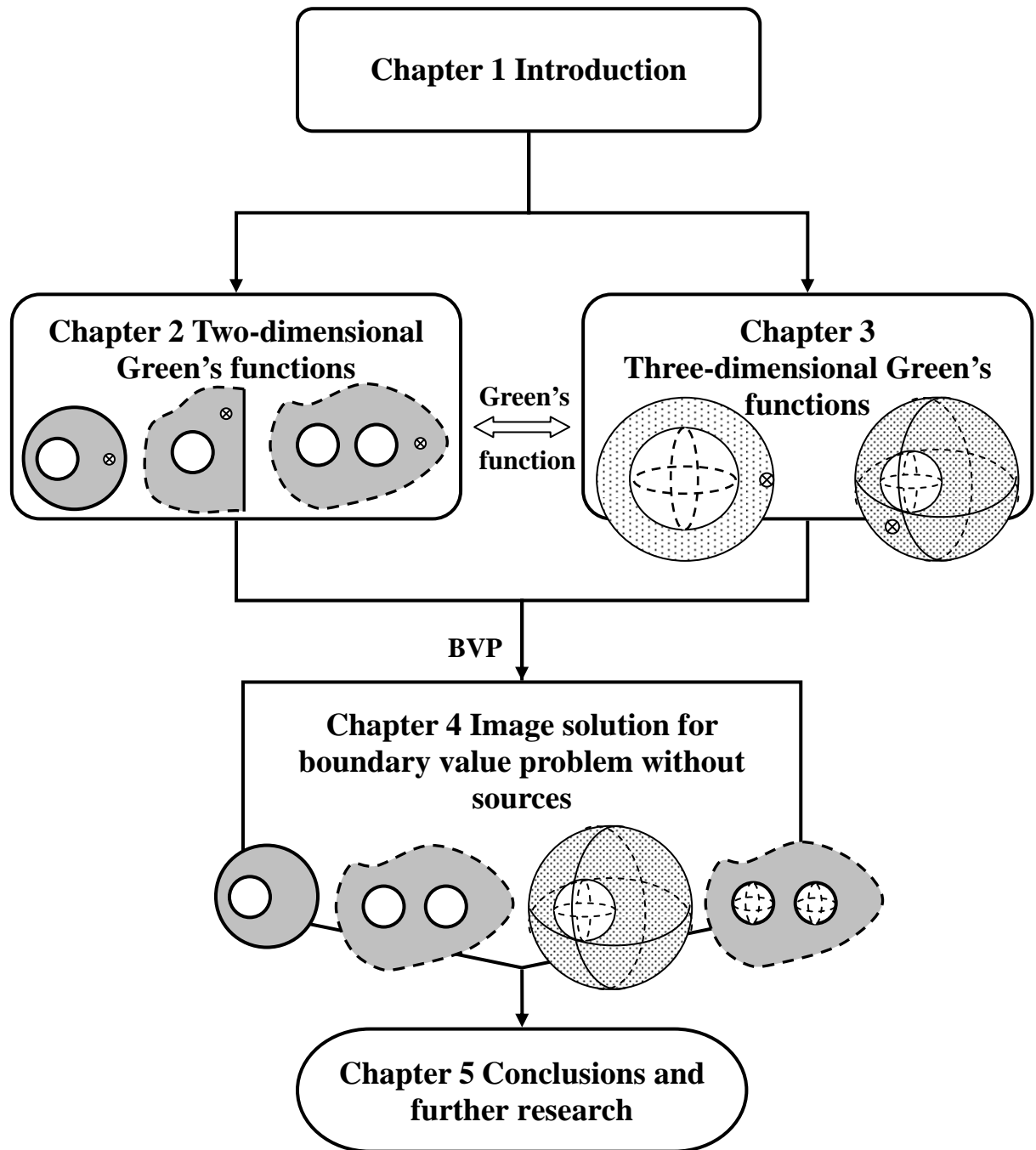
Fig. 1-4 The frame of this thesis

Chapter 2 Derivation of two-dimensional Green's functions for Laplace problem with circular boundaries

Summary

Green's functions of Laplace problems with circular boundaries are solved by using analytical and semi-analytical approaches. For the analytical solution, we derive the Green's function by using the bipolar coordinates. The image method is a semi-analytical approach. It is interesting to find that the two frozen images for the eccentric annulus by using the image method are located on the two focuses in the bipolar coordinates. This finding also occurs for the cases of a half plane with a circular hole and an infinite plane with two circular holes. The image method can be seen as a special case of the MFS with only at most four unknown strengths to be determined. The optimal locations of sources in the MFS can be captured by using the image method and they are dependent on the source location and the geometry of problems. Three illustrative examples were demonstrated to verify this point. Agreement among the results is observed.

2.1 Introduction

A number of physical and engineering problems governed by the Laplace equation in two independent variables, e.g., steady-state heat conduction, electrostatic potential and fluid flow, were solved by using conformal mapping to obtain an analytical solution. Besides, we can formulate the same problems by using special curvilinear coordinates to obtain a solution, e.g., bipolar coordinates and elliptic coordinates. Carrier and Pearson [8] employed the bilinear transformation of conformal mapping to solve certain kinds of potential problems. An eccentric case was mapped to an annular domain. For a polygonal shape, it can also be mapped to a regular region by using the

Schwarz-Christoffel transformation [42]. For the regular geometry, it is easy to solve the Laplace problem by using the polar or Cartesian coordinates. Muskhelishivili [52] gave us a detailed description how an eccentric annulus can be mapped into concentric annulus by using a simple form of linear fractional transformation. Chen and Weng [21] also used the similar method to solve eccentric annulus problems. Although a bilinear transformation was used, the mapping functions were not exactly the same between the one of Carrier and Pearson [8] and that of Muskhelishivili [52]. Problems of eccentric annulus or a half plane with a circular hole usually use the bipolar coordinates to derive the analytical solution [28]. Ling [47], Timoshenko and Goodier [58], and Lebedev et al. [43] all presented an analytic solution of using the bipolar coordinates for the torsion of an eccentric bar. However, the mapping functions were not exactly the same. One is a cotangent function [47], another is a hyperbolic tangent function [43] and the other is a hyperbolic cotangent function [58]. After the bipolar coordinate system is introduced, the problem of special domain can be solved by using the separation of variables. Although Carrier and Pearson [8], Muskhelishivili [52], Ling [47], Timoshenko and Goodier [58] have solved the eccentric Laplace problems, their approaches are very similar but they are not the same. Chen et al. [17] found that all the forgoing approaches can be unified after suitable transformations, translation, rotation and taking *log* in the conformal mapping. However, we will focus on the Green's function instead of BVP without sources in this chapter.

Green's function has been studied and applied in science and engineering by mathematicians as well as engineers, respectively [48]. A computer-friendly solution for the potential generated by a point source in the ring-shaped region was studied by Melnikov and Arman [49]. In order to derive the Green's function, Thomson [57] proposed the concept of reciprocal radii to find the image source to satisfy the homogeneous Dirichlet boundary condition by using the image method. Greenberg [27] and Riley et al. [53] employed a trick to satisfy the condition for two special points, then the image location can be determined. Chen and Wu [18] proposed a natural and logical way to find the location of image and the strength by employing the degenerate

kernel. The image method is a classical approach for constructing the Green's function. In certain cases, it is possible to obtain the exact solution for a concentrated source in a domain through superimposing the infinite plane solution for the given source and its image source. Although the scope of this method is limited, it yields a great deal of insight into the solution when it works [39]. Here, we will extend to a semi-analytical approach once the closed-form solution using the image method is not possible. Our goal is to broaden the scope of the image method.

In this chapter, we have three issues. First, the image method is seen as a special case of the MFS, since its image singularities locate outside the domain. Second, the optimal locations of the MFS sources are found to be dependent on the source location and the geometry of the problems. Third, it is found that the two frozen images of the image method are located on the two focuses in the bipolar coordinates. By using the bipolar coordinates and the image method, three cases, an eccentric annulus, a half plane with a circular hole and an infinite domain with two holes are solved. The bipolar coordinates are reviewed for the eccentric ring in Section 2.2. In Section 2.3, the image method is employed to derive the Green's function in problems with circular boundaries. Numerical results are given in Section 2.4. Finally, a conclusion is drawn in Section 2.5.

2.2 Geometric characterization of the bipolar coordinates

The relation between the bipolar coordinates (ξ, η) and the Cartesian coordinates (x, y) [17] are defined by

$$x + iy = ic \cot(\frac{1}{2}\zeta), \quad \zeta = \xi + i\eta, \tag{2-1}$$

where c is a positive constant. Equation (2-1) yields

$$x = c\frac{\sinh \eta}{\cosh \eta - \cos \xi}, \quad y = c\frac{\sin \xi}{\cosh \eta - \cos \xi}, \tag{2-2}$$

where $-\pi \le \xi < \pi$, $-\infty < \eta < \infty$. By eliminating ξ in Eq. (2-2), we obtain a circle with the center at $(c \coth \eta, 0)$ and the radius $c \operatorname{csch} \eta$ as shown below:

$$(x - c \coth \eta)^2 + y^2 = c^2 \operatorname{csch}^2 \eta .$$
(2-3)

Elimination of η from Eq. (2-2) results in the other circle with the center at $(0, c \cot \xi)$ and the radius of $c \csc \xi$ as given below:

$$x^2 + (y - c \cot(\xi))^2 = c^2 \csc^2(\xi) .$$
(2-4)

From Eqs. (2-3) and (2-4), the bipolar coordinates are shown in Fig. 2-1(a). Denoting by (r_{c1}, θ_1) and (r_{c2}, θ_2), we have

$$x + iy + c = r_{c1} e^{i\theta_1}, \quad x + iy - c = r_{c2} e^{i\theta_2} ,$$
(2-5)

$$\eta = \log(r_{1c} / r_{c2}), \quad \xi = \theta_2 - \theta_1 .$$
(2-6)

It follows that a curve $\xi = $ constant is a family of circles passing through the poles $(\pm c, 0)$. The curve of $\eta = $ constant shows a curve for which $r_{c1} / r_{c2} = $ constant. The eccentric annulus is shown in Fig. 2-1(b). The outer radius b, inner radius a and the distance d are determined from Eq. (2-3) as shown below:

$$a = c \operatorname{csch}(\eta_1) ,$$
(2-7)
$$b = c \operatorname{csch}(\eta_2) ,$$
(2-8)
$$d = c[\coth(\eta_2) - \coth(\eta_1)] .$$
(2-9)

To describe an eccentric annulus in the bipolar coordinates, the three parameters, c, η_1 and η_2 are determined as shown below:

$$c = \frac{\sqrt{a^4 + b^4 - 2a^2 b^2 - 2d^2(a^2 + b^2) + d^4}}{2d} ,$$
(2-10)

$$\eta_1 = \sinh^{-1}\left(\frac{c}{a}\right) ,$$
(2-11)

$$\eta_2 = \sinh^{-1}\left(\frac{c}{b}\right) ,$$
(2-12)

where η_1 and η_2 denote the inter and outer circles, respectively. Then, we can describe an eccentric annulus by using the bipolar coordinates. In this case, the Green's function was derived in terms of the bipolar coordinates as shown below [28]:

$$G(\xi,\eta;\xi_s,\eta_s) = \begin{cases} \dfrac{1}{2\pi}\left[\dfrac{(\eta_1-\eta)(\eta_2-\eta_s)}{\eta_1-\eta_2}\right. \\ \qquad \left. +2\sum_{n=1}^{\infty}\dfrac{\sinh n(\eta_1-\eta)\sinh n(\eta_2-\eta_s)}{n\sinh n(\eta_1-\eta_2)}\cos n(\xi-\xi_s)\right], \eta_1\geq\eta\geq\eta_s, \\ \\ \dfrac{1}{2\pi}\left[\dfrac{(\eta-\eta_2)(\eta_s-\eta_1)}{\eta_1-\eta_2}\right. \\ \qquad \left. +2\sum_{n=1}^{\infty}\dfrac{\sinh n(\eta_2-\eta)\sinh n(\eta_1-\eta_s)}{n\sinh n(\eta_1-\eta_2)}\cos n(\xi-\xi_s)\right], \eta_s\geq\eta\geq\eta_2, \end{cases} \tag{2-13}$$

where (ξ_s,η_s) is the position of the source point.

2.3 Image method

For a problem of two-dimensional eccentric annulus as shown in Fig. 2-2, the Green's function $G(x, s)$ satisfies

$$\nabla^2 G(x,s)=\delta(x-s), \quad x\in\Omega, \tag{2-14}$$

where Ω is the domain of interest, x is the field point and δ denotes the Dirac-delta function for the source at s. For simplicity, the Green's function is considered to be subject to the Dirichlet boundary conditions. In this case, we obtain the location of image point by using the fundamental solution and matching the boundary condition. The eccentric annulus can be seen as a combination of interior and exterior problems as shown in Fig. 2-3. The source point and the image point are s and s' in Fig. 2-3, respectively. When matching the homogeneous Dirichlet boundary conditions for the interior or exterior boundaries, position of the image source is at $(a^2/R_s,\theta)$, where $s=(R_s,\theta)$. We consider the fundamental solution $U(x,s)$ that is governed by

$$\nabla^2 U(x,s)=2\pi\delta(x-s). \tag{2-15}$$

Then, we obtain the fundamental solution as follows:
$$U(x,s)=\ln r, \tag{2-16}$$

where r is the distance between s and x $(r\equiv|x-s|)$. Based on the separable property of the addition theorem or the so-called degenerate kernel, the fundamental solution

$U(x,s)$ can be expanded into a series form by separating the field point $x(\rho,\phi)$ and source point $s(R_s,\theta)$ in the polar coordinates,

$$U(x,s) = \begin{cases} U^I(\rho,\phi;R_s,\theta) = \ln R_s - \sum_{m=1}^{\infty} \frac{1}{m}(\frac{\rho}{R_s})^m \cos m(\theta-\phi), \ R_s \geq \rho, \\ U^E(\rho,\phi;R_s,\theta) = \ln \rho - \sum_{m=1}^{\infty} \frac{1}{m}(\frac{R_s}{\rho})^m \cos m(\theta-\phi), \ R_s < \rho. \end{cases} \tag{2-17}$$

The semi-analytical approach can solve the Green's function of eccentric case. Following the successive image process, it is found that the final two image locations freeze at the s_{c1} and s_{c2}. The Green's functions for the three cases (a) an eccentric annulus, (b) a half plane with a circular hole and (c) an infinite plane with two holes are represented by

$$G(x,s) = \frac{1}{2\pi} \Bigg\{ \ln|x-s| - \lim_{N\to\infty} \Bigg[\sum_{i=1}^{N} \Big(\ln|x-s_{4i-3}| + \ln|x-s_{4i-2}| - \ln|x-s_{4i-1}| - \ln|x-s_{4i}| \Big) $$
$$+ c_1(N)\ln|x-s_{c1}| + c_2(N)\ln|x-s_{c2}| + e(N) \Bigg] \Bigg\}, \tag{2-18}$$

where s_{4i-3}, s_{4i-2}, s_{4i-1} and s_{4i} are the successive image locations [14], $e(N)$ can be understood as a rigid body term, $c_1(N)$ and $c_2(N)$ are the singularity strengths of the two frozen points at s_{c1} and s_{c2} which can be determined by matching the boundary conditions. Table 2-1 demonstrates that the frozen image points s_{c1} and s_{c2} happen to be the focuses in the bipolar coordinates.

2.4 Illustrative examples and discussions

Case 1: An eccentric case (a special case: annular case [49])

The problem sketch of an eccentric annulus is shown in Fig. 2-2. The location of image source and bipolar coordinates are shown in Fig. 2-4(a). The source point is located at $s = (0, 0.75)$. The centers of two holes are set at (0, 0) and (-4, 0), and radii are 0.4 and 1.0 for the inner and outer boundaries, respectively. Following the success of annulus case for the iterative images, we now extend to the eccentric case. In a similar way of finding the successive images for matching the inner and outer boundary conditions [14], the solution can be superimposed by using Eq. (2-18). Finally, we can find that the final frozen image points and the focuses of the bipolar coordinates are the same.

After collocating some points to match the boundary conditions, all the unknown coefficients can be determined. The results are compared well with the analytical solution by using the bipolar coordinates. The contour plots by using the present method of Eq. (2-18), the bipolar coordinates of Eq. (2-13) and the null-field BIEM [11] are shown in Fig. 2-5.

Case 2: A half plane with a circular hole

Figure 2-4(b) depicts the Green's function for the half plane with a hole and the Dirichlet boundary condition. The source point is located at $s=(3, 0)$. The center and radius of the hole is $(0, 0)$ and $a=1$. The $d/2=1.25$ is the distance from the center to the ground line. Similarly, the analytical and semi-analytical solutions are obtained by using the bipolar coordinates and the image method, respectively. The results agree well with those of the null-field BIEM [11] in Fig. 2-6.

Case 3: An infinite plane with two circular holes

Following the success of the eccentric annulus case for the iterative images, we now extend to the infinite plane with two circular holes as shown in Table 2-1. The problem sketch of the infinite plane with two circular holes is shown in Fig. 2-4(c). The source point is located at $s=(3.85, 0)$. The centers of two holes are set at $(0, 0)$ and $(2.1, 0)$, their radii are 0.4 and 1.0, respectively. In a similar way of finding the image for matching boundary conditions [14], an image solution is derived. We also found that the final frozen image points approach to the focuses of the bipolar coordinates. Based on the image solution for an infinite plane with a circular hole subject to the Neumann BC, an extra source at the center of hole is required. This motivates us to put sources at two centers of the holes to obtain acceptable results. Therefore, Eq. (2-18) is extended to

$$G(x,s) = \frac{1}{2\pi} \left\{ \ln|x-s| + \lim_{N\to\infty} \left[\left(\sum_{i=1}^{N} \ln|x-s_{2i-1}| + \ln|x-s_{2i}| \right) + c_1(N)\ln|x-s_{c1}| + c_2(N)\ln|x-s_{c2}| \right. \right.$$
$$\left. \left. + d_1(N)\left[\ln|x-s_{d1}| + \sum_{j=1}^{M} \ln|x-s_j^1| \right] + d_2(N)\left[\ln|x-s_{d2}| + \sum_{j=1}^{M} \ln|x-s_j^2| \right] \right] \right\},$$

(2-19)

where the s_{d1} and s_{d2} are located at the two centers of holes, s_j^1 and s_j^2 are the

successive images due to s_{d1} and s_{d2}, respectively. The results agree well with those of the null-field BIEM [11] and the conventional MFS in Fig. 2-7. It is interesting to find that the final images also freeze at focuses in the bipolar coordinates. The results are summarized in Table 2-1.

2.5 Conclusions

In this chapter, Green's functions were derived using the bipolar coordinates and the image method. It is found that final image points terminate at the two focuses of the bipolar coordinates for all the three cases, an eccentric annulus, a half plane with a circular hole and an infinite plane with two circular holes. The optimal source distribution in MFS is dependent on the given geometry and the source location. An image method can guide as to search for an optimal source location of MFS and can determine the strengths of sources except the two frozen images. Three examples were demonstrated to find all the image sources for constructing the Green's function. The dimension in the linear algebraic equation is at most four in all the examples. Agreement is observed after comparing with other solutions.

Table 2-1 Frozen points of the image method and focuses in the bipolar coordinates.

Cases / Method	(1)	(2)	(3)

Image method	$G(x,s)=\dfrac{1}{2\pi}\left\{\ln|x-s|+\lim_{N\to\infty}\left[(\sum_{m=1}^{N}-\ln|x-s_{4i-3}|-\ln|x-s_{4i-2}|+\ln|x-s_{4i-1}|\right.\right.$ $\left.\left.+\ln|x-s_{4i}|)+c_1(N)\ln|x-s_{c1}|+c_2(N)\ln|x-s_{c2}|+e(N)]\right\}$		$G(x,s)=\dfrac{1}{2\pi}\left\{\ln|x-s|+\lim_{N\to\infty}\left[\left(\sum_{i=1}^{N}\ln|x-s_{2i-1}|\right.\right.\right.$ $+\ln|x-s_{2i}|)+c_1(N)\ln|x-s_{c1}|+c_2\ln|x-s_{c2}|$ $+d_1(N)\left[\ln|x-s_{d1}|+\sum_{j=1}^{M}\ln|x-s_j^1|\right]$ $\left.\left.\left.+d_2(N)\left[\ln|x-s_{d2}|+\sum_{j=1}^{M}\ln|x-s_j^2|\right]\right]\right\}\right.$

	$x_1-d=\dfrac{a^2}{x_2-d},\ x_2=\dfrac{b^2}{x_1+d}$	$x_1=\dfrac{a^2}{x_2},\ \ x_2=d-x_1,\ \text{(when } b=a)$	$d-x_1=\dfrac{a^2}{d-x_2},\ x_2=\dfrac{b^2}{x_1}$

$$c=\frac{(x_2-x_1)}{2}=\frac{\sqrt{a^4-2a^2b^2+b^4-2a^2d^2-2b^2d^2+d^4}}{2d}\Rightarrow\frac{\sqrt{d^2-4a^2}}{2}(a=b)$$

Bipolar Coordinates	
	$$c=\frac{\sqrt{a^4-2a^2b^2+b^4-2a^2d^2-2b^2d^2+d^4}}{2d}$$

16

(a) Bipolar coordinates system (poles located on ($\pm 1, 0$))
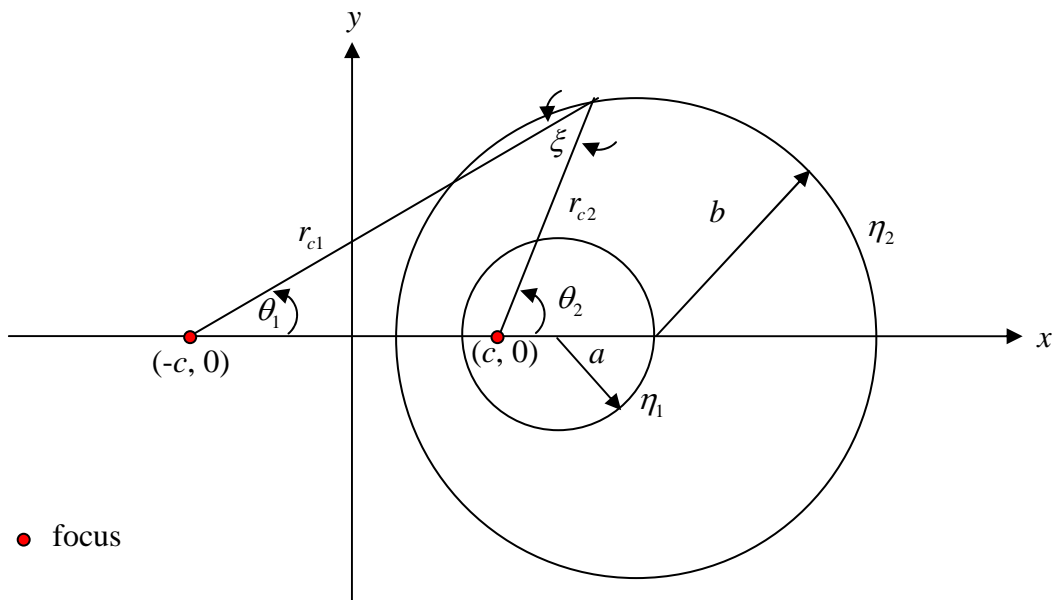
(b) Geometry relation of bipolar coordinates.

Figure 2-1 The sketch of curve family (a) bipolar coordinate system, (b) geometric relation of bipolar coordinates.
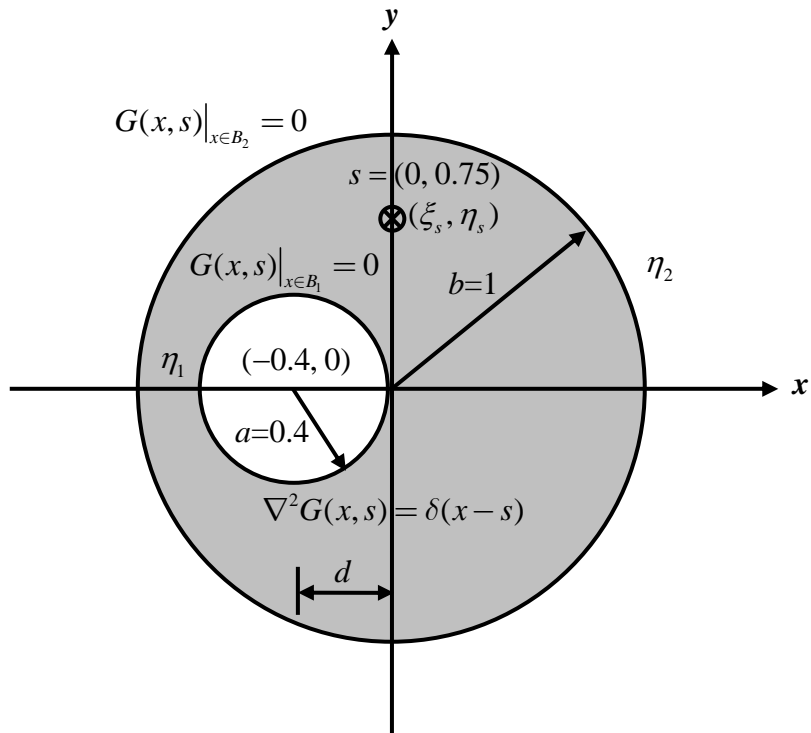
Figure 2-2 Problem sketch for the Green's function of an eccentric annulus.
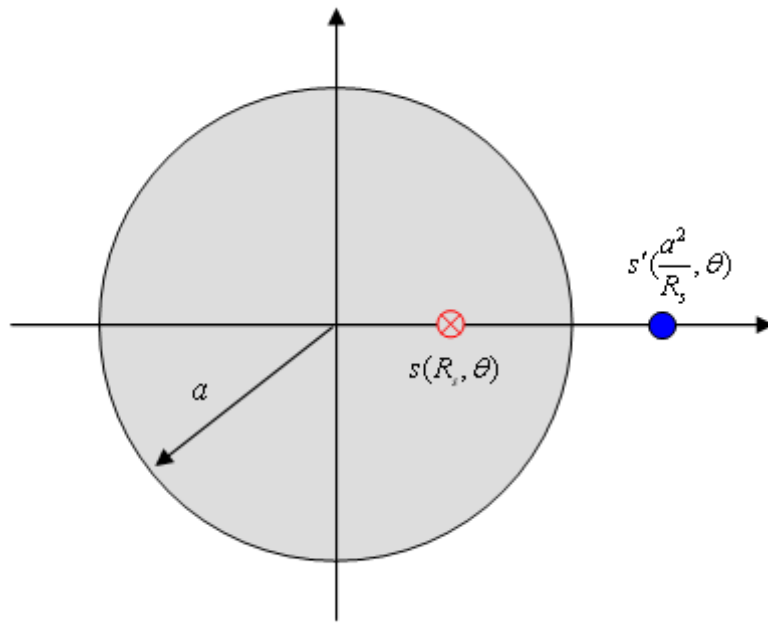
(a)
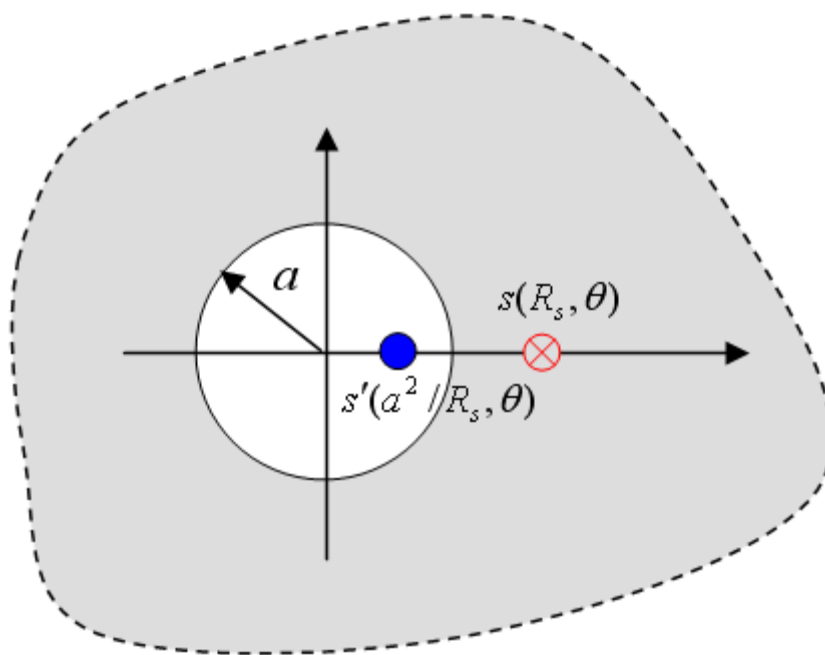
(b)

Figure 2-3 Sketch of position of image point (a) an interior case, and (b) an exterior case.
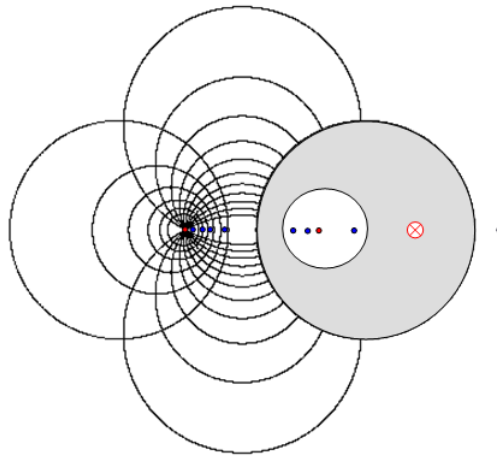
(a) an eccentric annulus
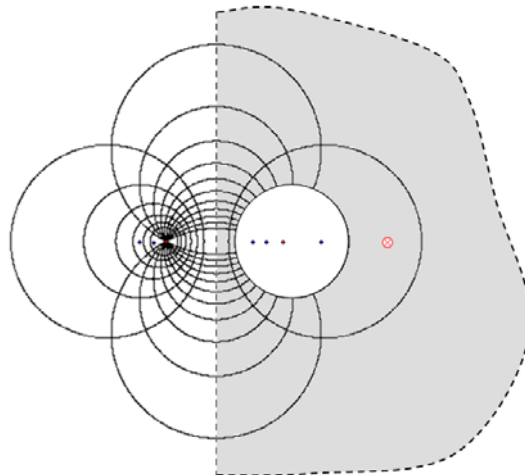
(b) a half plane with a circular hole
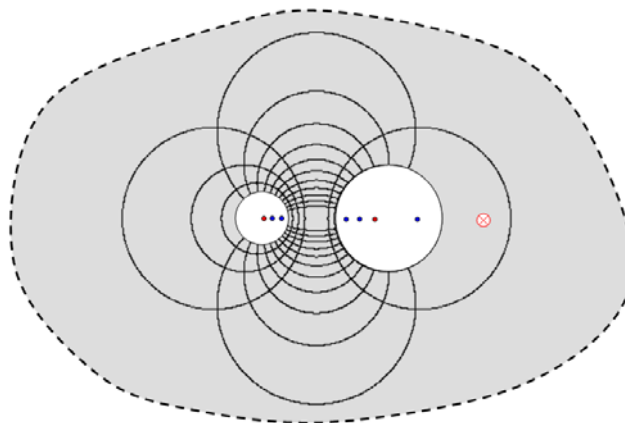
(c) an infinite plane with two circular holes

Figure 2-4 Final images and the focuses of the bipolar coordinate (a) an eccentric annulus, (b) a half plane with a circular hole and (c) an infinite plane with two circular holes.
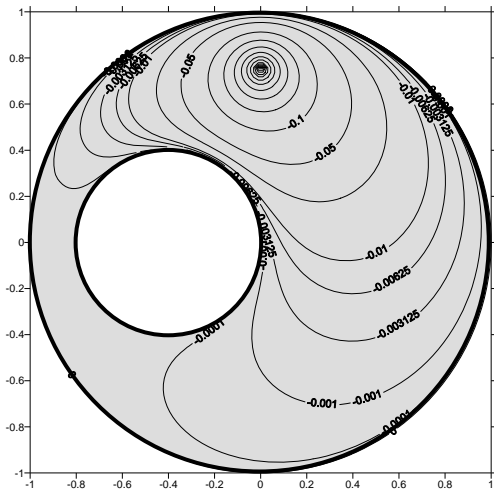
(a) an analytical solution
using bipolar coordinates
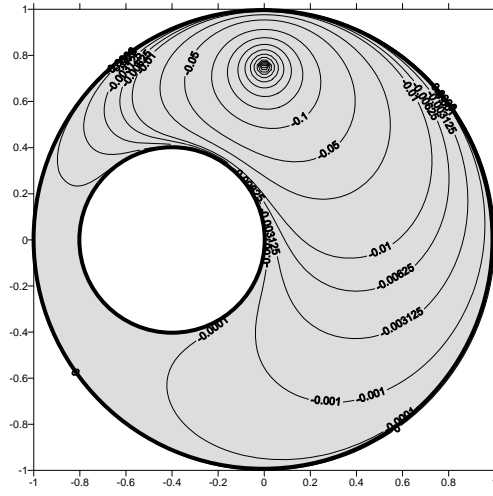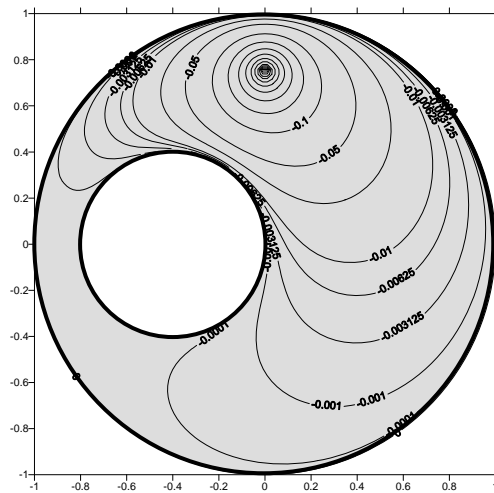
(b) image solution

(c) solution using superposition
technique and the null-field BIEM
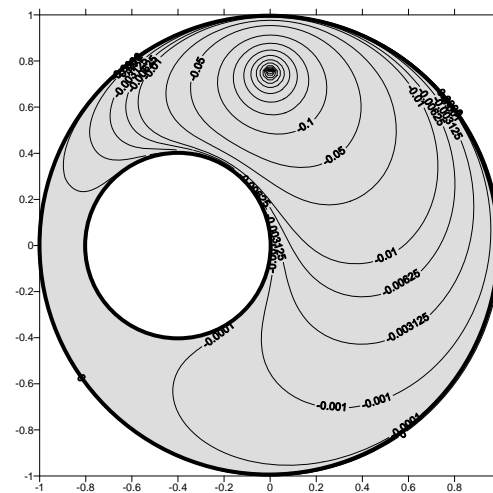
(d) solution using the Green's third
identity in the null-field BIEM

Figure 2-5 Green's function using (a) an analytical solution using bipolar coordinate,
(b) image solution, (c) solution using superposition technique and the null-field
BIEM [11] and (d) solution using the Green's third identity in the null field BIEM.
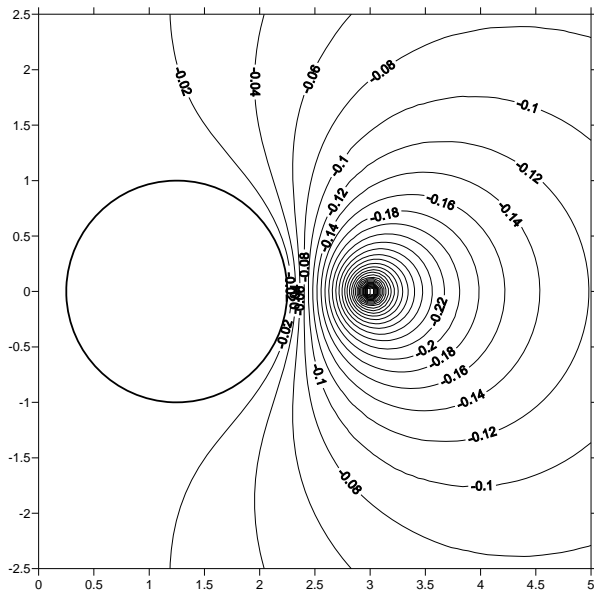
(a) an analytical solution using bipolar coordinates
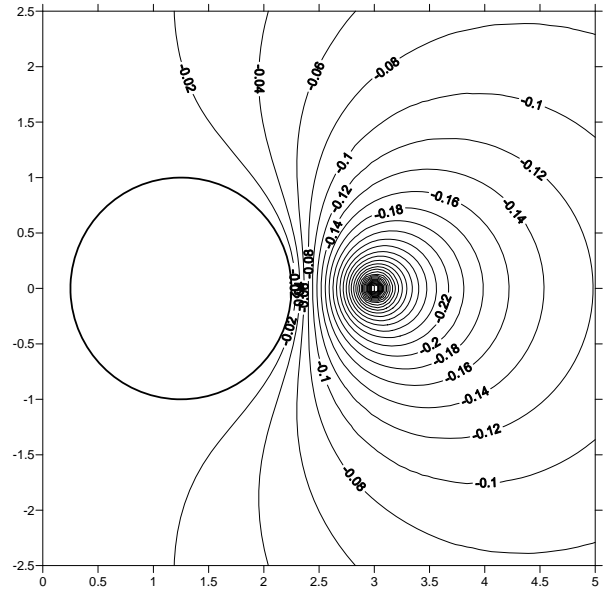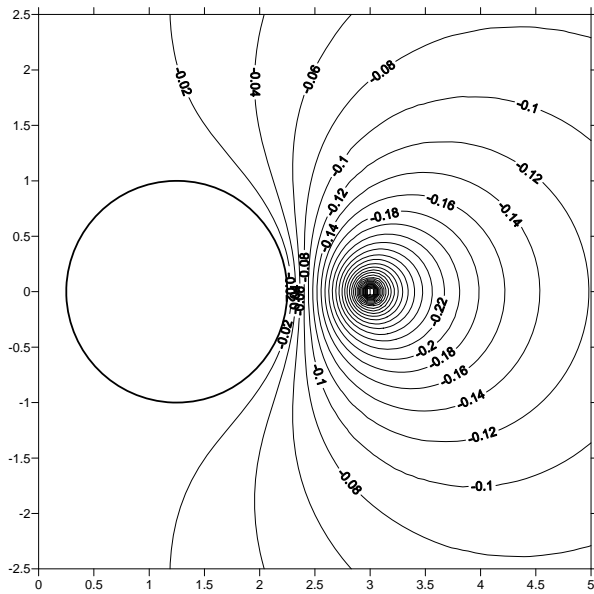
(b) image solution

(c) solution using superposition technique and the null-field BIEM
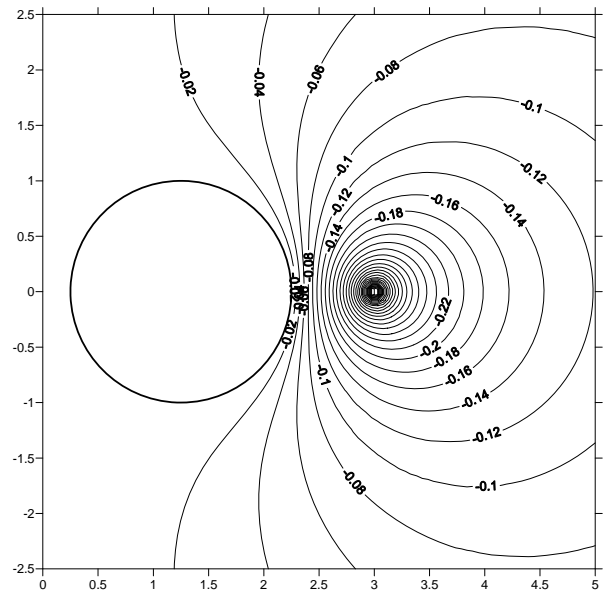
(d) solution using the Green's third identity in the null-field BIEM

Figure 2-6 Green's function using (a) an analytical solution using bipolar coordinate, (b) image solution, (c) solution using superposition technique and the null-field BIEM [11] and (d) solution using the Green's third identity in the null field BIEM.
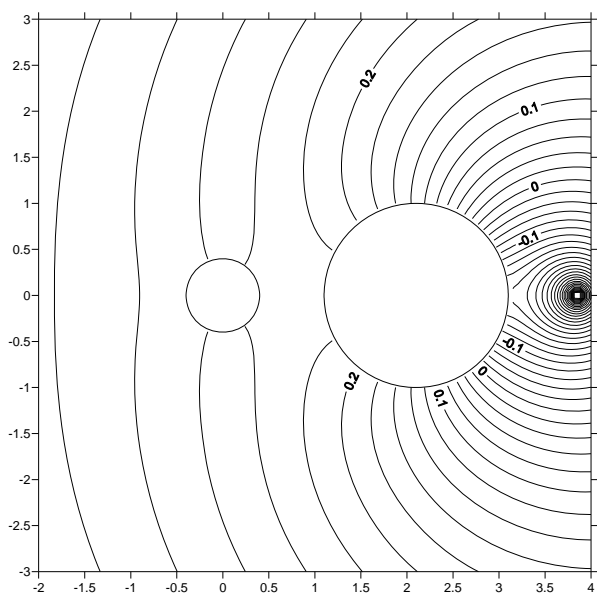
(a) image solution
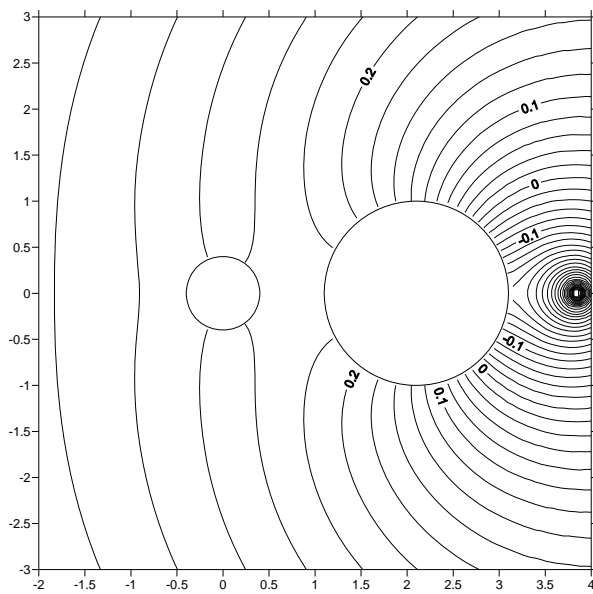
(b) solution using superposition technique and
the null-field BIEM
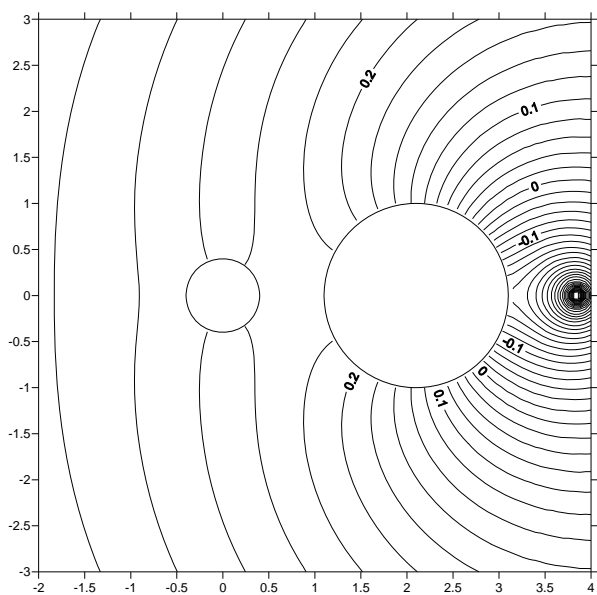
(c) solution using the Green's third identity in
the null-field BIEM
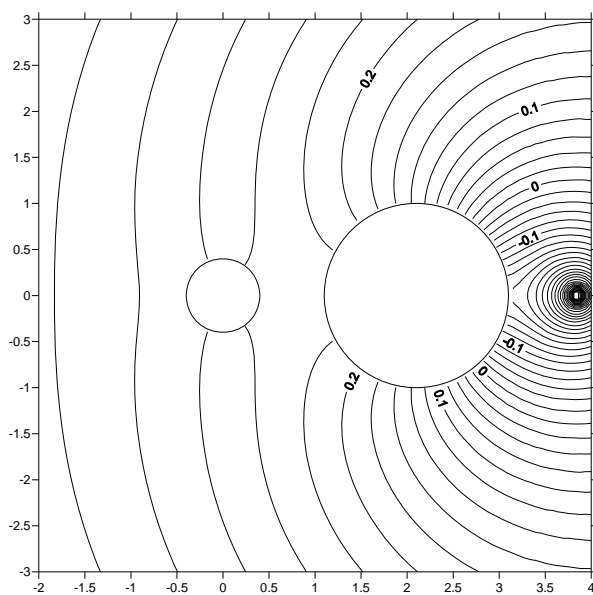
(d) solution of MFS

Figure 2-7 Green's function using (a) image solution, (b) solution using superposition technique
the null-field BIEM [11], (c) solution using the Green's third identity in the null field BIEM and
(d) solution of MFS.

Chapter 3 Derivation of three-dimensional Green's function for Laplace problem with sphere boundaries

Summary

Following the success of the mathematical equivalence between the Trefftz method and the MFS for the annular Green's function [14], we extend to solve the Green's function of 3-D problems in this chapter. The Green's function of the concentric sphere is first derived by using the image method which can be seen as a special case of MFS solutions. Dirichlet boundary conditions are considered. Also, the Trefftz method is employed to derive the analytical solution by using the T-complete sets. By employing the addition theorem, both solutions are found to be mathematically equivalent when the number of Trefftz bases and the number of image points are both infinite. In the successive image process, the final two images freeze at the origin and infinity, where their singularity strengths can be analytically and numerically determined in a consistent manner. The agreement among the three results, including two analytical solutions by using the Trefftz method and the image method, and one numerical solution by using the conventional MFS is observed.

The main result is the analytical derivation of Green's function for the domain bounded by non-concentric spheres in terms of bispherical coordinates. Both surfaces, inner and outer boundaries are specified by the Dirichelet boundary conditions. This work can be seen as an extension study for the Green's function of eccentric annulus derived by Heyda. To verify the solution, a semi-analytical solution using the image method and a numerical solution using the MFS are utilized for comparisons. Good agreement is made.

3.1 Introduction

In 1926, Trefftz presented the Trefftz method for solving boundary value problems by superimposing the functions which satisfy the governing equation [40]. The unknown

coefficients are determined by matching the boundary condition. In the potential theory, it is well known that the MFS can solve potential problems when a fundamental solution is known. This method was proposed by Kupradze [41] in Russia. The MFS can be viewed as an indirect boundary element method containing concentrated sources instead of boundary distributions. The initial idea is to approximate the solution through a linear combination of fundamental solutions where sources are located outside the domain of the problem. Moreover, it has certain advantages over BEM, e.g., no singularity and no boundary integrals are required. Bogomolny [6] studied the stability and error bound of the MFS. Li et al. [46] used the effective condition number to study the ill-poseness of collocation approaches, the MFS and the Trefftz method. They found that the condition number of the MFS is much worst than that of the Trefftz method. Although the Trefftz method and the MFS individually have a long history, the link between the two methods was not discussed in the literature until Chen et al.'s papers [14, 19]. Researchers have paid attention to construct the mathematical relationship between the Trefftz method and MFS since 2006. For example, Schabck [54] found that the MFS with singularity at infinity behaves like the Trefftz base of harmonic polynomials. Chen et al. proved the equivalence between the Trefftz method and the MFS for Laplace and biharmonic problems containing a circular domain [19]. The key point is the use of the degenerate kernel or so-called the addition theorem. They only proved the equivalence by demonstrating a simple circle with angular distribution of singularity to link the two methods. Following the success of deriving the annular Green's function [14], we plan to derive the Green's function of a concentric sphere. Here, we also distribute singularities along the radial direction by using the method of image. Image solutions and Trefftz results for the annular Green's function were obtained [14]. Since a two-dimensional problem can be solved easily by using the complex variable, the image method can be seen as an alternative way to obtain the solution. However, the extension to 3-D problem is limited for the theory of complex variable. The image method can deal with the 3-D problems without any difficulty.

An analytical solution for the Green's function of an annular ring was given in the book of Courant and Hilbert [25]. When the bounding circles of the annular region are no

longer concentric, the reflection principle is not easy to be implemented. In the Lebedev et al.'s book [43], many special coordinates were mentioned to solve problems with a special geometry such as the bipolar coordinates and the bispherical coordinates. Upon introducing the bipolar coordinates as given in [43, 51], the Green's function of an eccentric annulus has been derived by Heyda [28]. Chen et al. [13, 14] employed the image method to revisit the Green's functions for annular (analytical) and eccentric (semi-analytical) cases. In the recent years, the method of fundamental solutions to solve boundary value problem also attracted the attention of researchers since the numerical method is truly meshless. In this paper, we solve the Green's function for the domain bounded by non-concentric spheres using the biospherical coordinates. This solution was not provided in the Lebedev et al.'s book [43] and was not solved by Heyda [28]. The fundamental solution is expanded into a series form in terms of the bispherical coordinates. The solution is decomposed into singular and regular parts. After matching the boundary conditions, the unknown coefficients in the regular part solution can be determined. To verify the accuracy of the analytical solution, one semi-analytical solution using the image method and one numerical solution using the MFS are utilized for comparisons.

In this paper, we focus on proving the mathematical equivalence on the Green's functions for the Laplace problem of a concentric sphere derived by using the Trefftz method and the image method. Both surfaces of inner and outer boundaries are specified by the Dirichlet boundary conditions. By employing the image method and the addition theorem, the mathematical equivalence of the two solutions derived by using the Trefftz method and the image method will be proved when the number of successive image points and the number of the Trefftz bases are both infinite. The image method can be seen as a special case of the conventional MFS, since its image singularities locate outside the domain. The solution by using the image method for constructing the 2-D Green's function also indicates that a free constant is required for the completeness of the solution which is always neglected in the conventional MFS. In the 3-D case, the free constant becomes zero as the number of successive image points become infinity.

3.2 Construction of the Green's function for the domain boundary by concentric sphere by using the image method and the MFS

3.2.1 The image solution

For the problem of concentric sphere as shown in Fig. 3-1, the Green's function satisfies

$$\nabla^2 G(x,s) = \delta(x-s), \quad x \in D,$$ (3-1)

where D is the domain of interest and δ denotes the Dirac-delta function for the source at s. For simplicity, the Green's function is considered to be subject to the Dirichlet boundary condition,

$$G(x,s) = 0, \quad x \in B_1 \cup B_2,$$ (3-2)

where B_1 and B_2 are the inner and outer boundaries of the sphere, respectively. We consider the fundamental solution $U(s,x)$ for a source singularity which satisfies

$$\nabla^2 U(x,s) = \delta(x-s).$$ (3-3)

Then, we obtain the fundamental solution as follows:

$$U(x,s) = \frac{-1}{4\pi r},$$ (3-4)

where r is the distance between s and x ($r \equiv |x-s|$). Based on the separable property of the addition theorem or degenerate kernel, the fundamental solution $U(x,s)$ can be expanded into series form in the spherical coordinates:

$$U(x,s) = \begin{cases} U^i = \dfrac{-1}{4\pi R_s} - \displaystyle\sum_{n=1}^{\infty}\sum_{m=0}^{n} \frac{\varepsilon_m}{4\pi} \frac{(n-m)!}{(n+m)!} \cos\left(m(\bar{\phi}-\phi)\right) P_n^m(\cos\bar{\theta}) P_n^m(\cos\theta) \frac{\rho^n}{R_s^{n+1}}, & R_s \geq \rho, \\[4mm] U^e = \dfrac{-1}{4\pi\rho} - \displaystyle\sum_{n=1}^{\infty}\sum_{m=0}^{n} \frac{\varepsilon_m}{4\pi} \frac{(n-m)!}{(n+m)!} \cos\left(m(\bar{\phi}-\phi)\right) P_n^m(\cos\bar{\theta}) P_n^m(\cos\theta) \frac{R_s^n}{\rho^{n+1}}, & R_s < \rho, \end{cases}$$ (3-5)

where $x = (\rho, \bar{\theta}, \bar{\phi})$, $s = (R_s, \theta, \phi)$, $P_n^m(\bullet)$ is the associated Legendre polynomial, the superscripts of i and e denote the interior and exterior regions, respectively, and ε_m is the Neumann factor which defined by,

$$\varepsilon_m = \begin{cases} 1, & m = 0, \\ 2, & m = 1, 2, \cdots \infty. \end{cases}$$ (3-6)

As mentioned in [16], the interior and exterior Green's functions can satisfy the homogeneous Dirichlet boundary conditions if the image source is correctly selected.

The closed-form Green's functions for both interior and exterior problems are written to be the same form

$$G(x, s; s') = \frac{1}{4\pi}\left(\frac{-1}{|x-s|} + \frac{R_s}{a}\frac{1}{|x-s'|}\right), \quad x \in D, \tag{3-7}$$

where a is the radius of the sphere, $s = (R_s, \pi/2, 0)$, and s' is the image source and its position is at $(a^2/R_s, \pi/2, 0)$ as shown in Fig. 3-2. It is interesting that the formulae for the location of image are the same as the 2-D case [14]. However, the magnitude of strength (R_s/a) is different from the 2-D case [14].

In order to match the inner and outer homogenous Dirichlet boundary conditions, the image relation between the source point and successive image points yields

$$R_1 = \frac{b^2}{R_s}, \quad R_5 = \frac{b^2}{R_s}\frac{b^2}{a^2}, \ldots\ldots, R_{4i-3} = \frac{b^2}{R_s}(\frac{b^2}{a^2})^{i-1},$$

$$R_2 = \frac{a^2}{R_s}, \quad R_6 = \frac{a^2}{R_s}\frac{a^2}{b^2}, \ldots\ldots, R_{4i-2} = \frac{a^2}{R_s}(\frac{a^2}{b^2})^{i-1},$$

$$R_3 = \frac{b^2 R_s}{a^2}, \quad R_7 = \frac{b^2 R_s}{a^2}\frac{b^2}{a^2}, \ldots, R_{4i-1} = \frac{b^2 R_s}{a^2}(\frac{b^2}{a^2})^{i-1}, \tag{3-8}$$

$$R_4 = \frac{a^2 R_s}{b^2}, \quad R_8 = \frac{a^2 R_s}{b^2}\frac{a^2}{b^2}, \ldots, R_{4i} = \frac{a^2 R_s}{b^2}(\frac{a^2}{b^2})^{i-1}.$$

The successive image points for the concentric sphere are shown in Fig. 3-3. After successive image process, the main part of Green's function is expressed by

$$G_m(x, s) = \frac{1}{4\pi}\left\{\frac{-1}{|x-s|} + \lim_{N\to\infty}\sum_{i=1}^{N}\left[\frac{w_{4i-3}}{|x-s_{4i-3}|} + \frac{w_{4i-2}}{|x-s_{4i-2}|} - \frac{w_{4i-1}}{|x-s_{4i-1}|} - \frac{w_{4i}}{|x-s_{4i}|}\right]\right\}, \tag{3-9}$$

where w_k is the weighting of the kth image point which is determined by [16]

$$w_1 = \frac{R_1}{b} = \frac{b}{R_s}, \quad w_5 = \frac{aR_5}{b^2} = \frac{b}{R_s}(\frac{b}{a}), \quad w_9 = \frac{a^2 R_9}{b^3} = \frac{b}{R_s}(\frac{b}{a})^2, \ldots, w_{4i-3} = \frac{b}{R_s}(\frac{b}{a})^{i-1},$$

$$w_2 = \frac{a}{R_s}, \quad w_6 = \frac{a^2}{bR_s} = \frac{a}{R_s}(\frac{a}{b}), \quad w_{10} = \frac{a^3}{b^2 R_s} = \frac{a}{R}(\frac{a}{b})^2, \ldots, w_{4i-2} = \frac{a}{R_s}(\frac{a}{b})^{i-1},$$

$$w_3 = \frac{aR_3}{bR_s} = \frac{b}{a}, \quad w_7 = \frac{a^2 R_7}{b^2 R_s} = \frac{b}{a}(\frac{b}{a}), \quad w_{11} = \frac{a^3 R_{11}}{b^3 R_s} = \frac{b}{a}(\frac{b}{a})^2, \ldots, w_{4i-1} = \frac{b}{a}(\frac{b}{a})^{i-1}, \tag{3-10}$$

$$w_4 = \frac{a}{b}, \quad w_8 = \frac{a^2}{b^2} = \frac{a}{b}(\frac{a}{b}), \quad w_{12} = \frac{a^3}{b^3} = \frac{a}{b}(\frac{a}{b})^2, \ldots\ldots, w_{4i} = \frac{a}{b}(\frac{a}{b})^{i-1}.$$

Satisfaction of the boundary condition by using interpolation functions

We set $G_m(x, s)$ to be the main part of the Green's function in Eq. (3-9). Unfortunately, $G_m(x, s)$ in Eq. (3-9) can not simultaneously satisfy both the inner and outer boundary

conditions of $G_m(x_a, s) = G_m(x_b, s) = 0$, where $x_a = (a, \bar{\theta}, \bar{\phi})$, $x_b = (b, \bar{\theta}, \bar{\phi})$, $0 \leq \bar{\theta} \leq \pi$, $0 \leq \bar{\phi} \leq 2\pi$. In order to satisfy both the inner and outer boundary conditions, an alternative method is introduced such that we have

$$G(x,s) = G_m(x,s) - \left(\frac{b(\rho - a)}{\rho(b-a)} \right) G_m(x_b, s) - \left(\frac{a(b-\rho)}{\rho(b-a)} \right) G_m(x_a, s), \quad a \leq \rho \leq b, \quad (3\text{-}11)$$

where $\left(b(\rho - a) / \rho(b-a) \right)$ and $\left(a(b-\rho) / \rho(b-a) \right)$ are the interpolation functions, $G_m(x_b, s) = -(\frac{a}{b})^N \frac{1}{b}$ and $G_m(x_a, s) = \frac{-1}{R_s}(\frac{a}{b})^N$. Therefore, Eq. (3-11) can be simplified to

$$G(x,s) = \frac{1}{4\pi} \left\{ \frac{-1}{|x-s|} + \lim_{N \to \infty} \sum_{i=1}^{N} \left[\frac{w_{4i-3}}{|x-s_{4i-3}|} + \frac{w_{4i-2}}{|x-s_{4i-2}|} - \frac{w_{4i-1}}{|x-s_{4i-1}|} - \frac{w_{4i}}{|x-s_{4i}|} \right] \right.$$
$$\left. + C + D\frac{1}{\rho} \right\}, \quad (3\text{-}12)$$

where $C = (\frac{a}{b})^N \left[\frac{a-R_s}{R_s(a-b)} \right]$ and $D = (\frac{a}{b})^N \left[\frac{a(R_s-b)}{R_s(a-b)} \right]$. Equation (3-12) indicates that not only image singularities at s_{4i-3}, s_{4i-2}, s_{4i-1} and s_{4i}, but also one singularity at the origin and one rigid body term for one singularity at infinity are required. The Green's function in Eq. (3-12) satisfies the governing equation and boundary conditions at the same time. It is found that a conventional MFS always loses a free constant and completeness may be questionable.

Satisfaction of boundary conditions to determine two singularity strengths at the origin and infinity

After successive image process, the final two image locations freeze at the origin and infinity. There are two strengths of singularities to be determined. Therefore, the Green's function is rewritten as

$$G(x,s) = \frac{1}{4\pi} \left\{ \frac{-1}{|x-s|} + \lim_{N \to \infty} \left[\sum_{i=1}^{N} \left(\frac{w_{4i-3}}{|x-s_{4i-3}|} + \frac{w_{4i-2}}{|x-s_{4i-2}|} - \frac{w_{4i-1}}{|x-s_{4i-1}|} - \frac{w_{4i}}{|x-s_{4i}|} \right) \right. \right.$$
$$\left. \left. + c(N) + \frac{d(N)}{\rho} \right] \right\}, \quad (3\text{-}13)$$

where the final two images locate at the center of sphere and infinity with strength of $c(N)$ and $d(N)$, respectively, which can be analytically and numerically determined by matching the inner and outer boundary conditions.

After matching the inner and outer boundary conditions, the unknown coefficients $c(N)$ and $d(N)$ are determined by using the numerical method and analytical approach are shown in Fig. 3-4. Agreement is made.

3.2.2 The conventional MFS [41]

In the method of fundamental solutions, the Green's function $G(x,s)$ is superimposed by using the fundamental solutions $U(x,s)$, as follows:

$$G(x,s) = \frac{-1}{4\pi r} + \sum_{j=1}^{N_M} \alpha_j U(x,s_j), \ \ x \in D, \tag{3-14}$$

where the N_M is the number of source points which are distributed outside the domain, α_j is the jth unknown coefficient. By similarly matching the boundary conditions in Eq. (3-2), the unknown coefficient α_j can be determined. Then, we have a numerical solution. By comparing Eq. (3-13) with Eq. (3-14), the image method of Eq. (3-13) can be seen as a special MFS of Eq. (3-14) with optimal locations and specified strengths for the singularities except the two strengths at two frozen points.

3.3 Derivation of the Green's function for the domain bounded by concentric spheres using the Trefftz method

The problem of a concentric sphere in Fig. 3-5 can be decomposed into two parts. One is an infinite space with a concentrated source (fundamental solution) in Fig. 3-5(a) and the other is subject to specified boundary conditions as shown in Fig. 3-5(b). The first-part solution can be obtained from the fundamental solution. Here, the second part is solved by using the Trefftz method. The solution can be superposed by using the Trefftz bases as shown below:

$$G_T(x,s) = \sum_{j=1}^{N_T} p_j \Phi_j, \tag{3-15}$$

where p_j is the weighting, Φ_j is the jth T-complete function and N_T is the number of T-complete functions. Here, the T-complete functions are given as 1,

$\rho^n P_n^m(\cos\overline{\theta})\cos(m\overline{\phi})$ and $\rho^n P_n^m(\cos\overline{\theta})\sin(m\overline{\phi})$ for the interior case and $1/\rho$, $\rho^{-(n+1)}P_n^m(\cos\overline{\theta})\cos(m\overline{\phi})$ and $\rho^{-(n+1)}P_n^m(\cos\overline{\theta})\sin(m\overline{\phi})$ for the exterior case. The second-part solution can be represented by

$$G_T(x,s) = A_{00} + \frac{B_{00}}{\rho} + \sum_{n=1}^{\infty}\sum_{m=0}^{n}[A_{nm}\rho^n P_n^m(\cos\overline{\theta})\cos(m\overline{\phi}) + B_{nm}\rho^{-(n+1)}P_n^m(\cos\overline{\theta})\cos(m\overline{\phi})$$
$$+ C_{nm}\rho^n P_n^m(\cos\overline{\theta})\sin(m\overline{\phi}) + D_{nm}\rho^{-(n+1)}P_n^m(\cos\overline{\theta})\sin(m\overline{\phi})], \tag{3-16}$$

where A_{00}, B_{00}, A_{nm}, B_{nm}, C_{nm} and D_{nm} are unknown coefficients. By matching the boundary conditions, the unknown coefficients can be determined. Then, the series-form Green's function is obtained by superimposing the solutions of $U(x,s)$ and $G_T(x,s)$ as shown below:

$$G(x,s) = \frac{-1}{4\pi|x-s|} + A_{00} + \frac{B_{00}}{\rho}$$
$$+ \sum_{n=1}^{\infty}\sum_{m=0}^{n}[A_{nm}\rho^n P_n^m(\cos\overline{\theta})\cos(m\overline{\phi}) + B_{nm}\rho^{-(n+1)}P_n^m(\cos\overline{\theta})\cos(m\overline{\phi})$$
$$+ C_{nm}\rho^n P_n^m(\cos\overline{\theta})\sin(m\overline{\phi}) + D_{nm}\rho^{-(n+1)}P_n^m(\cos\overline{\theta})\sin(m\overline{\phi})], \tag{3-17}$$

where the unknown coefficients are obtained as shown below:

$$\begin{Bmatrix} A_{00} \\ B_{00} \end{Bmatrix} = \begin{Bmatrix} \dfrac{R_s - a}{4\pi R_s(b-a)} \\[3mm] \dfrac{a(b-R_\xi)}{4\pi R_s(b-a)} \end{Bmatrix}, \tag{3-18}$$

$$\begin{Bmatrix} A_{nm} \\ B_{nm} \end{Bmatrix} = \begin{Bmatrix} \dfrac{\varepsilon_m}{4\pi}\dfrac{(n-m)!}{(n+m)!}\left[\dfrac{R_s^{2n+1} - a^{2n+1}}{R_s^{n+1}\left(b^{2n+1}-a^{2n+1}\right)}\right]P_n^m(\cos\theta)\cos(m\phi) \\[4mm] \dfrac{\varepsilon_m}{4\pi}\dfrac{(n-m)!}{(n+m)!}\left[\dfrac{a^{2n+1}\left(b^{2n+1}-R_s^{2n+1}\right)}{R_s^{n+1}\left(b^{2n+1}-a^{2n+1}\right)}\right]P_n^m(\cos\theta)\cos(m\phi) \end{Bmatrix}, \tag{3-19}$$

$$\begin{Bmatrix} C_{nm} \\ D_{nm} \end{Bmatrix} = \begin{Bmatrix} \dfrac{\varepsilon_m}{4\pi}\dfrac{(n-m)!}{(n+m)!}\left[\dfrac{R_s^{2n+1} - a^{2n+1}}{R_s^{n+1}\left(b^{2n+1}-a^{2n+1}\right)}\right]P_n^m(\cos\theta)\sin(m\phi) \\[4mm] \dfrac{\varepsilon_m}{4\pi}\dfrac{(n-m)!}{(n+m)!}\left[\dfrac{a^{2n+1}\left(b^{2n+1}-R_s^{2n+1}\right)}{R_s^{n+1}\left(b^{2n+1}-a^{2n+1}\right)}\right]P_n^m(\cos\theta)\sin(m\phi) \end{Bmatrix}, \tag{3-20}$$

It is interesting to find that Eq. (3-18) can be included into Eq. (3-19) since we introduce the Neumann factor and set *n=m=0*. We will prove the equivalence of solutions derived by using the Trefftz method and the image method (special MFS) in the next section.

3.4 Mathematical equivalence for the solutions derived by the MFS and Trefftz method

3.4.1 Method of fundamental solutions (image method)

The image method can be seen as a special case of the conventional MFS, since its singularities are located outside the domain. The Green's function of Eq. (3-13) can be expanded into a series form by separating the field point x and source point s for the fundamental solution in the spherical coordinates of Eq. (3-5) as shown below:

$$
\begin{aligned}
G(x,s) = &\frac{1}{4\pi}\left[\frac{-1}{|x-s|}+\frac{R_s-a}{R_s(b-a)}+\frac{a(b-R_s)}{R_s\rho(b-a)}\right] \\
&+\sum_{i=1}^{\infty}\sum_{n=1}^{\infty}\sum_{m=0}^{n}\frac{\varepsilon_m}{4\pi}\frac{(n-m)!}{(n+m)!}\left[w_{4i-3}\left(\frac{\rho^n}{R_{4i-3}^{n+1}}\right)+w_{4i-2}\left(\frac{R_{4i-2}^n}{\rho^{n+1}}\right)\right. \\
&\left.-w_{4i-1}\left(\frac{\rho^n}{R_{4i-1}^{n+1}}\right)-w_{4i}\left(\frac{R_{4i}^n}{\rho^{n+1}}\right)\right]\cos[m(\bar{\phi}-\phi)]P_n^m(\cos\bar{\theta})P_n^m(\cos\theta).
\end{aligned}
\tag{3-21}
$$

By using Eqs. (3-8) and (3-10), the series containing four geometry series with the same ratio of $(a/b)^{2n+1}$ which is smaller than one in Eq. (3-13) can be rearranged into

$$
\begin{aligned}
G(x,s) = &\frac{1}{4\pi}\left[\frac{-1}{|x-s|}+\frac{R_s-a}{R_s(b-a)}+\frac{a(b-R_s)}{R_s\rho(b-a)}\right] \\
&+\sum_{n=1}^{\infty}\sum_{m=0}^{n}\frac{\varepsilon_m}{4\pi}\frac{(n-m)!}{(n+m)!}\left[\frac{R_s^{2n+1}\rho^{2n+1}-a^{2n+1}\rho^{2n+1}+a^{2n+1}b^{2n+1}-a^{2n+1}R_s^{2n+1}}{R_s^{n+1}\rho^{n+1}(b^{2n+1}-a^{2n+1})}\right] \\
&\cos[m(\bar{\phi}-\phi)]P_n^m(\cos\bar{\theta})P_n^m(\cos\theta),
\end{aligned}
\tag{3-22}
$$

after expanding all the image singularities of $-1/r$ functions. It is interesting to find that the optimal location may not be the expansion type of Fig. 3-6(a) or angular distribution of Fig. 3-6(b) but a lump singularity in one radial direction shown in Fig. 3-6(c) as mentioned by Antunes [2]. In this paper, our image location in the MFS only distribute along the radial direction which agrees with the optimal location in [2]. This finding agrees with the experience in the annular case [14] and the present case of a concentric sphere.

3.4.2 Trefftz method

Substitution of Eqs. (3-18)-(3-20) into Eq. (3-17) yields

$$G(x,s) = \frac{1}{4\pi}\left[\frac{-1}{|x-s|} + \frac{R_s - a}{R_s(b-a)} + \frac{a(b-R_s)}{R_s\rho(b-a)}\right]$$
$$+ \sum_{n=1}^{\infty}\sum_{m=0}^{n}\frac{\varepsilon_m}{4\pi}\frac{(n-m)!}{(n+m)!}\left[\frac{R_s^{2n+1}\rho^{2n+1} - a^{2n+1}\rho^{2n+1} + a^{2n+1}b^{2n+1} - a^{2n+1}R_s^{2n+1}}{R_s^{n+1}\rho^{n+1}(b^{2n+1} - a^{2n+1})}\right] \quad (3\text{-}23)$$
$$\cos[m(\bar{\phi}-\phi)]P_n^m(\cos\bar{\theta})P_n^m(\cos\theta),$$

After comparing Eq. (3-22) with Eq. (3-23), it is found that the two solutions, Eqs. (3-13) and (3-17) are proved to be mathematically equivalent by using the addition theorem when the number of images and the number of Trefftz bases are both infinite. To verify the Trefftz and image solutions, the conventional MFS is utilized for comparison. The distribution of collocation nodes and images (sources of MFS) is shown in Fig. 3-7. Contour plots by using the three approaches are shown in Fig. 3-8. Good agreement is observed.

3.5 Derivation of the Green's function for non-concentric spheres

3.5.1 Geometric characterization of the bispherical coordinates

Many curvilinear coordinates were mentioned to deal with problems of special geometry [43]. For example, the bipolar coordinates are suitable for the eccentric annulus as shown in Fig. 3-9. The relation between the Cartesian coordinates (x, y) and the bipolar coordinates (ξ, η) can be linked by

$$x = c\frac{\sinh(\eta)}{\cosh(\eta) - \cos(\xi)}, \; y = c\frac{\sin(\xi)}{\cosh(\eta) - \cos(\xi)}, \quad (3\text{-}24)$$

where c is the half distance between two focuses. Similarly, the non-concentric spheres problem can be described by using the bispherical coordinates as shown in Fig. 3-10. The bispherical coordinates are obtained by rotating the bipolar axes about the line between two focuses, and the relationship to the Cartensian coordinates is shown below:

$$x = c\frac{\sin(\xi)\cos(\phi)}{\cosh(\eta) - \cos(\xi)}, \; y = c\frac{\sin(\xi)\sin(\phi)}{\cosh(\eta) - \cos(\xi)}, \; z = c\frac{\sinh(\eta)}{\cosh(\eta) - \cos(\xi)}, \quad (3\text{-}25)$$

where $0 < \xi < \pi$, $-\infty < \eta < \infty$, $-\pi < \phi < \pi$, and

$$\xi = \theta_2 - \theta_1, \eta = \ln\left(r_{c1}/r_{c2}\right), \phi = \arctan(y/x). \quad (3\text{-}26)$$

It follows that the curves $\xi = $ constant are a family of spheres passing through two focuses $(0, \pm c, 0)$ which can be described by

$$(r_{xy} - c\cot(\xi))^2 + z^2 = c^2 \csc^2(\xi), \tag{3-27}$$

where $r_{xy} = \sqrt{x^2 + y^2}$. The curve of $\eta = $ constant are also a family of spheres with the center at $y = c\coth(\eta)$, which can also be described by

$$(y - c\coth(\eta))^2 + r_{xy}^2 = c^2 \operatorname{csch}^2(\eta). \tag{3-28}$$

The inner radius a, outer radius b and the distance h between two centers for the non-concentric spheres are given by

$$a = c\operatorname{csch}(\eta_1), \tag{3-29}$$
$$b = c\operatorname{csch}(\eta_2), \tag{3-30}$$
$$h = c[\coth(\eta_2) - \coth(\eta_1)], \tag{3-31}$$

in Fig. 3-10, respectively. In order to describe the non-concentric spheres in the bispherical coordinates, the three parameters, c, η_1 and η_2 are determined as follows,

$$c = \frac{\sqrt{a^4 + b^4 - 2a^2b^2 - 2h^2(a^2 + b^2) + h^4}}{2h}, \tag{3-29}$$

$$\eta_1 = \sinh^{-1}\left(\frac{c}{a}\right), \tag{3-30}$$

$$\eta_2 = \sinh^{-1}\left(\frac{c}{b}\right). \tag{3-31}$$

The coordinates of two focuses are obtained as shown below:

$$c_1 = (0, \ -c, \ 0), \tag{3-32}$$
$$c_2 = (0, \ c, \ 0). \tag{3-33}$$

For this case, the Green's function was derived in terms of the bispherical coordinates as shown below [43]:

$$
G(\xi,\eta,\phi;\xi_s,\eta_s,\phi_s) = \begin{cases}
\dfrac{1}{2\pi c}h_x h_s \displaystyle\sum_{n=0}^{\infty}\sum_{m=0}^{n}\varepsilon_m \dfrac{(n-m)!}{(n+m)!}P_n^m(\cos(\xi_s)) \\[2mm]
\quad P_n^m(\cos(\xi))\cos\big[m(\phi-\phi_s)\big] \\[2mm]
\quad \dfrac{\sinh\big[(n+\tfrac{1}{2})(\eta_1-\eta)\big]\sinh\big[(n+\tfrac{1}{2})(\eta_2-\eta_s)\big]}{\sinh\big[(n+\tfrac{1}{2})(\eta_1-\eta_2)\big]} \\[2mm]
\quad ,\ \eta_1 \geq \eta \geq \eta_s, \\[4mm]
\dfrac{1}{2\pi c}h_x h_s \displaystyle\sum_{n=0}^{\infty}\sum_{m=0}^{n}\varepsilon_m \dfrac{(n-m)!}{(n+m)!}P_n^m(\cos(\xi_s)) \\[2mm]
\quad P_n^m(\cos(\xi))\cos\big[m(\phi-\phi_s)\big] \\[2mm]
\quad \dfrac{\sinh\big[(n+\tfrac{1}{2})(\eta_2-\eta)\big]\sinh\big[(n+\tfrac{1}{2})(\eta_1-\eta_s)\big]}{\sinh\big[(n+\tfrac{1}{2})(\eta_1-\eta_2)\big]} \\[2mm]
\quad ,\ \eta_s \geq \eta \geq \eta_2,
\end{cases}
\tag{3-34}
$$

where the subscript s for ξ, η and ϕ denotes the location of source in the bispherical coordinates, and the factors h_x and h_s are defined by

$$
h_x = \sqrt{\cosh(\eta)-\cos(\xi)}, \tag{3-35}
$$

$$
h_s = \sqrt{\cosh(\eta_s)-\cos(\xi_s)}. \tag{3-36}
$$

3.5.2 Image method – semi-analytical solution

For the problem of non-concentric spheres as shown in Fig. 3-11, the Green's function satisfies

$$
\nabla^2 G(x,s) = \delta(x-s), \quad x \in D, \tag{3-37}
$$

where D is the domain, δ denotes the Dirac-delta function, x is the field point and s is the source point. The specified boundary condition is the Dirichlet type,

$$
G(x,s) = 0, \quad x \in B_1 \cup B_2, \tag{3-38}
$$

where B_1 and B_2 are the inner and outer boundaries, respectively. The semi-analytical approach can solve the Green's function of non-concentric case. Following the successive image process that image points for the non-concentric spheres is shown in Fig. 3-12, it is found that the final two image locations freeze at the s_{c1} and s_{c2}. The image solution for non-concentric spheres is below:

$$G(x,s) = \frac{1}{4\pi}\left\{\frac{-1}{|x-s|} + \lim_{N\to\infty}\left[\sum_{i=1}^{N}\left(\frac{w_{4i-3}}{|x-s_{4i-3}|} + \frac{w_{4i-2}}{|x-s_{4i-2}|} - \frac{w_{4i-1}}{|x-s_{4i-1}|} - \frac{w_{4i}}{|x-s_{4i}|}\right)\right.\right.$$
$$\left.\left. + \frac{c_1(N)}{|x-s_{c1}|} + \frac{c_2(N)}{|x-s_{c2}|}\right]\right\}, \ x \in D, \qquad (3\text{-}39)$$

where $c_1(N)$ and $c_2(N)$ are the singularity strengths of the two frozen points at s_{c1} and s_{c2} which can be determined by matching the boundary conditions. Then, we have the image solution of Eq. (3-39) which belongs to a semi-analytical solution.

3.6 Illustrative examples and discussions

Case 1: Green's function for a domain bounded by non-concentric spheres (**a concentrated source at the *z* axis**)

In the first case, a Green's function for non-concentric spheres and its location of the concentrated source is at the z axis as shown in Fig. 3-13. The distance from the center of outer sphere to the source point is equal to 2.5. The two radii of inner and outer spheres are $a = 2$ and $b = 5$, respectively. The two centers of inner and outer spheres are $(0, 0, c\coth(\eta_1))$ and $(0, 0, c\coth(\eta_2))$, the distance h between two centers is equal to 2. The distribution of fictitious sources is shown in Fig 3-14. Figures 3-15(a) to 8(c) show the potential contours by using the bispherical coordinates (an analytical solution), the image method (a semi-analytical solution) and the method of fundamental solutions (a numerical solution). The distribution of image points is shown in Fig. 3-12, while the sources distribution of the MFS is shown in Fig. 3-14. The frozen images happen to be the two focuses in the bispherical coordinates. It is found that the results of three approaches match well.

Case 2: Green's function for a non-concentric spheres (**a concentrated source at S_2**)

In the second case, the concentrated source is moved to $s_2 = (2.5, 0, c\coth(\eta_2))$ as shown in Fig. 3-16. The other parameters of geometry are the same with the case 1. Also, the frozen images terminate at the two focuses in the bispherical coordinates. Figures 3-17(a) to (c) show the potential contours by using three approaches. Similarly, good agreement is made after comparing other results.

3.7 Concluding remarks

In this chapter, not only the image method (a special MFS) but also the Trefftz method was employed to solve the Green's function of 3-D Laplace problems bounded by concentric spheres. The two solutions using the Trefftz method and MFS for the fixed-fixed case were proved to be mathematically equivalent by using the addition theorem or so-called degenerate kernel. Also, the solution of image method shows the existence of the free constant which is always overlooked in the conventional MFS although it becomes zero as the number of images approaches infinity. Finally, we also found the final two frozen image points at the origin and infinity where their strengths can be determined numerically and analytically in a consistent manner. Contour plots by using the three approaches, Trefftz method, image method and MFS, agree well.

In other cases, analytical Green's functions for the three-dimensional Laplace problems were derived. After comparing with the semi-analytical solution using the image method and the numerical solution determined by the method of fundamental solutions, the agreement was observed to verify the accuracy of the analytical solution. This analytical solution can provide a benchmark example for the Green's function of 3-D Laplace problems.
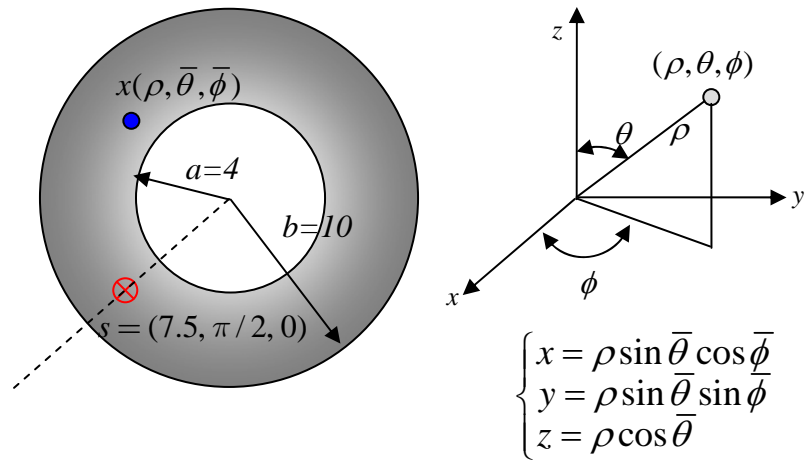
Figure 3-1 Sketch of an annular sphere subject to a concentrated load.
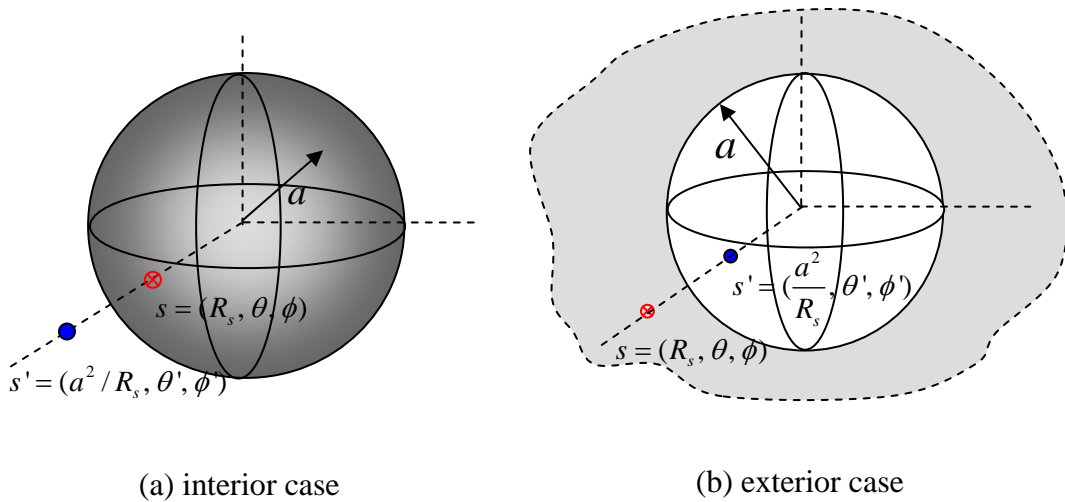

(a) interior case

(b) exterior case

Figure 3-2 Sketch of position of image point (a) interior case and (b) exterior case.
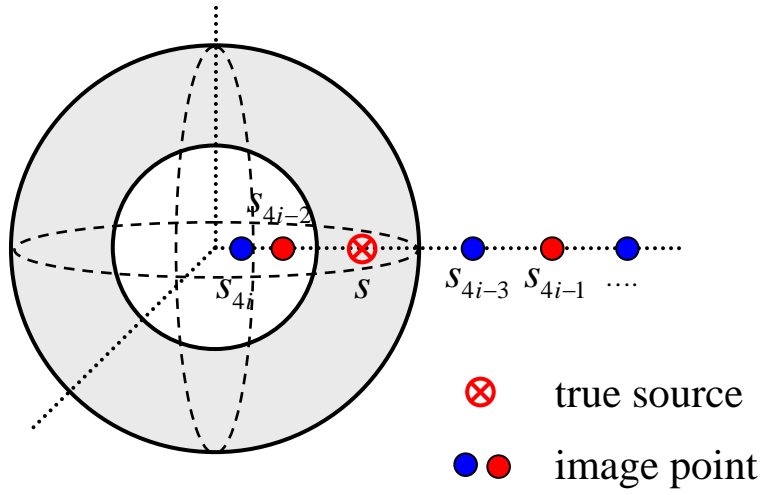
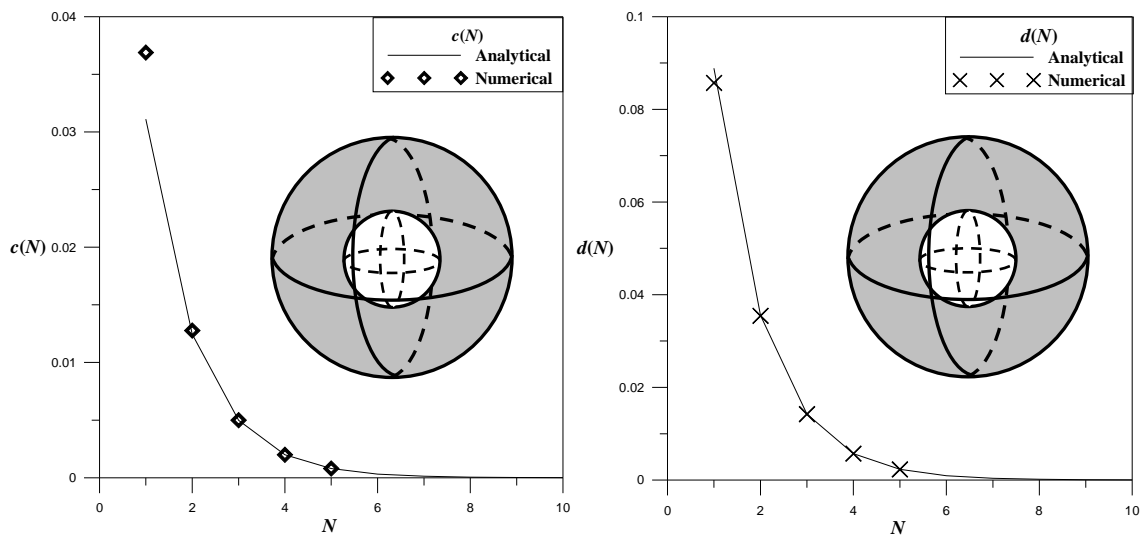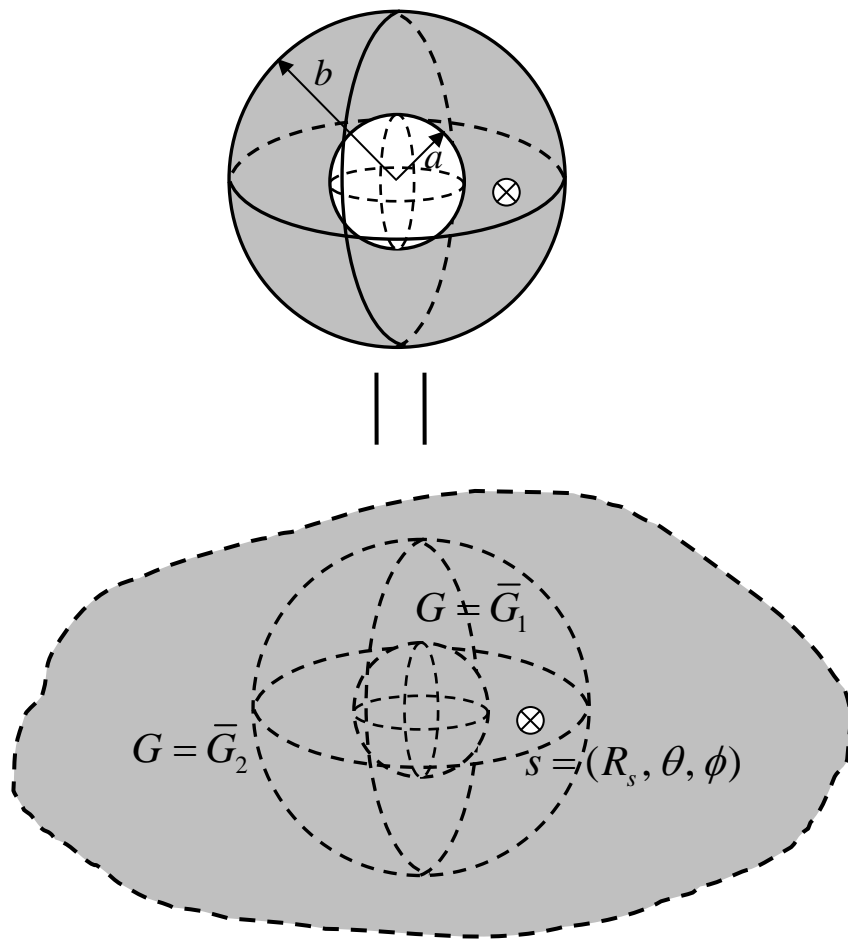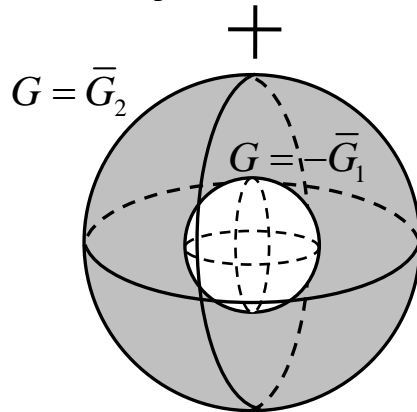Figure 3-3 Successive images for an annular problem.

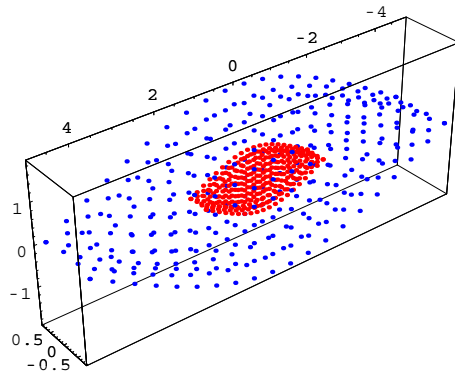Figure 3-4 Coefficients of $c(N)$ and $d(N)$ versus N for the fixed-fixed case.

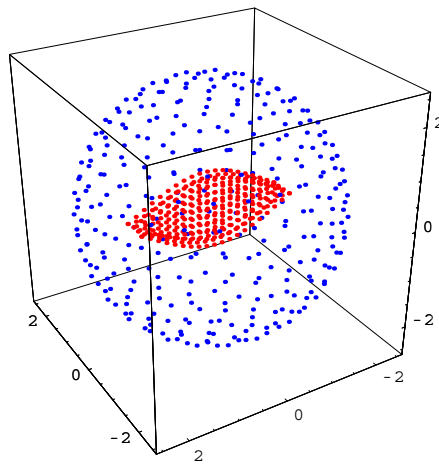(a) an infinite space with a concentrated source

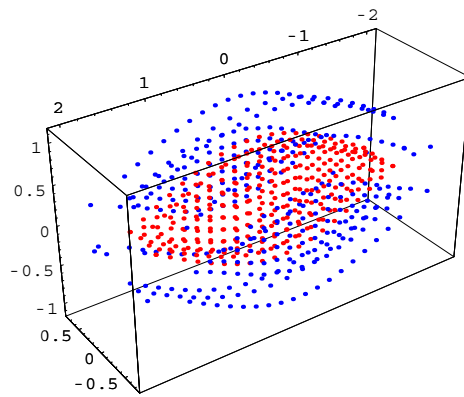(b) a concentric sphere subject to the Dirichlet boundary condition

Figure 3-5 Sketch of the superposition approach. (a) an infinite space with a concentrated source. (b) a concentric sphere subject to the Dirichlet boundary condition.
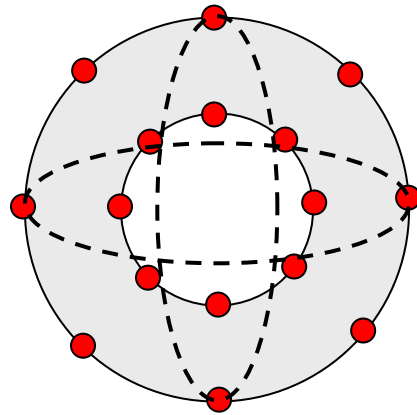
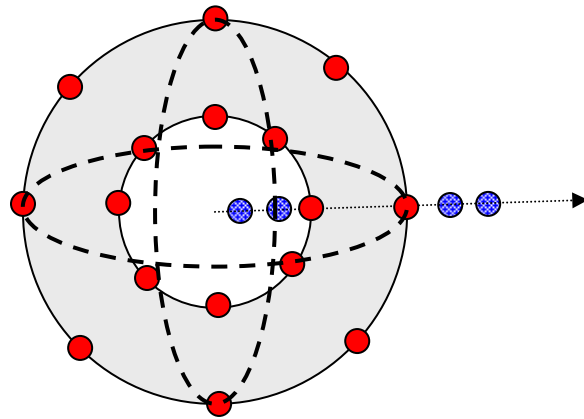(a) Expansion

(b) Sphere

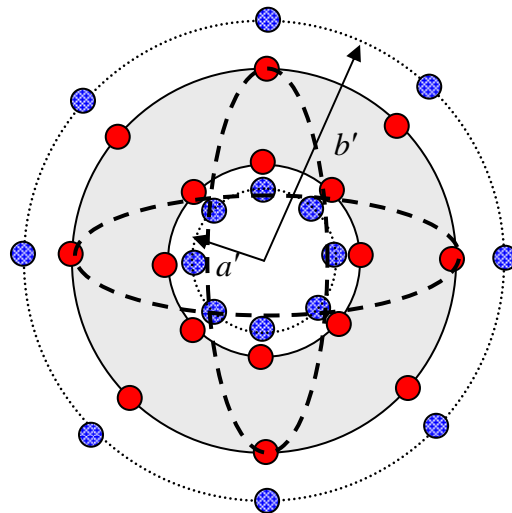(c) Lump (Optimal case)

Figure 3-6 Optimal locations for conventional MFS [2].

(a) Trefftz method

(b) Image method (Special MFS, radial distribution of singularities)

(c) Conventional MFS (angular distribution of singularities)

Figure 3-7 Sketches of (a) Trefftz method, (b) image method and (c) MFS.
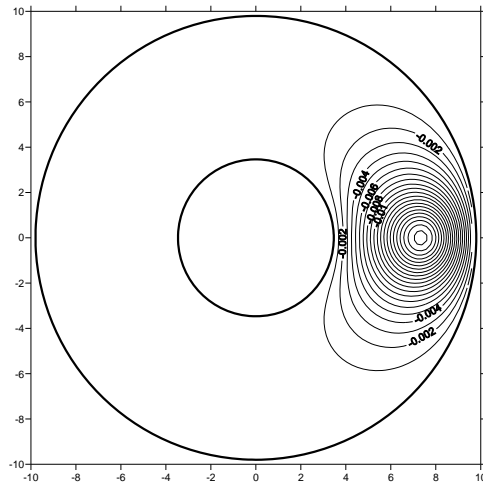
Figure 3-8(a) Potential contour by using the bispherical coordinates ($z = 2$ plane).
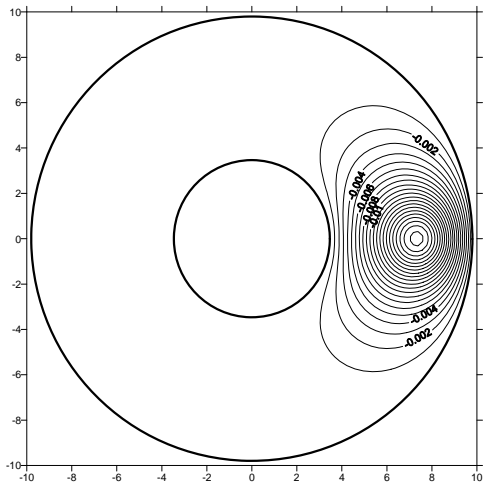
Figure 3-8(b) Potential contour by using the image method ($z = 2$ plane).
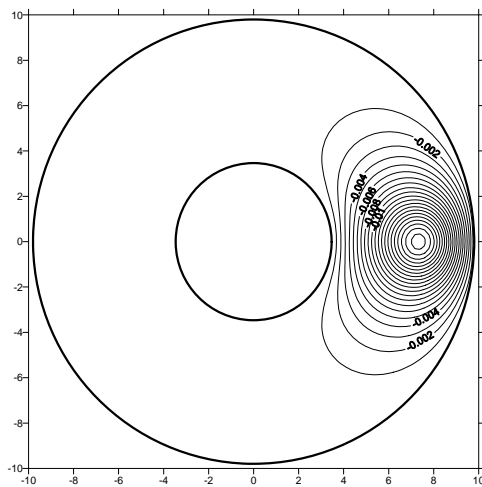
Figure 3-8 (c) Potential contour by using the MFS ($z = 2$ plane).

43
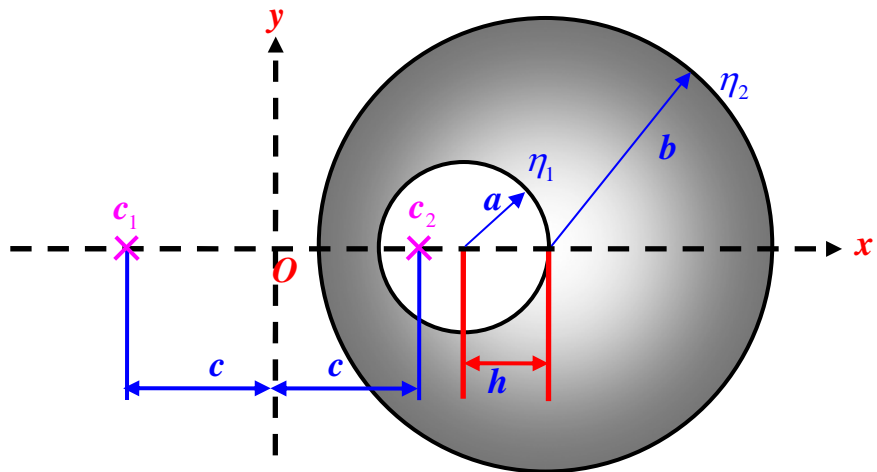
Figure 3-9 An eccentric annulus in the bipolar coordinate system (2-D case).
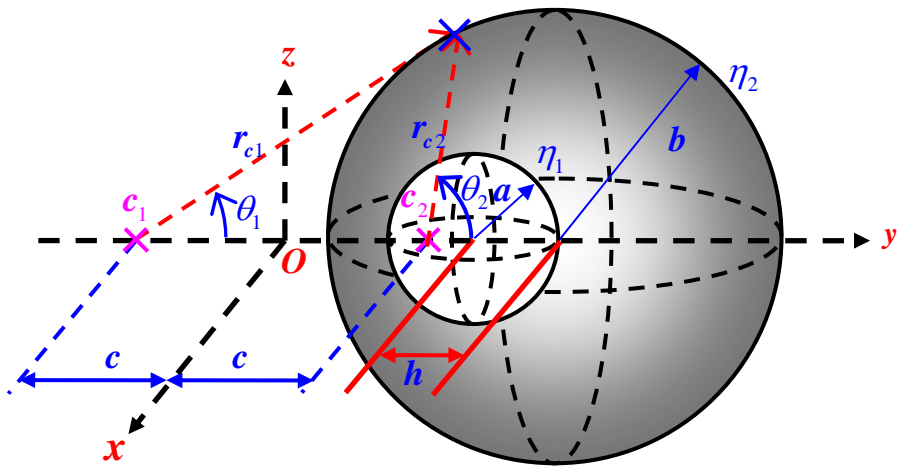
Figure 3-10 A non-concentric problem in the bispherical coordinate system (3-D case).
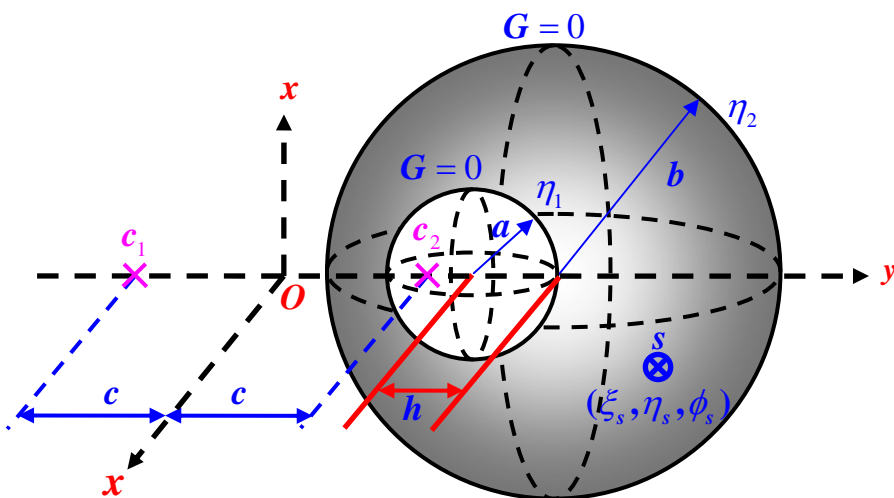
Figure 3-11 A Green's function for a domain bounded by non-concentric spheres.
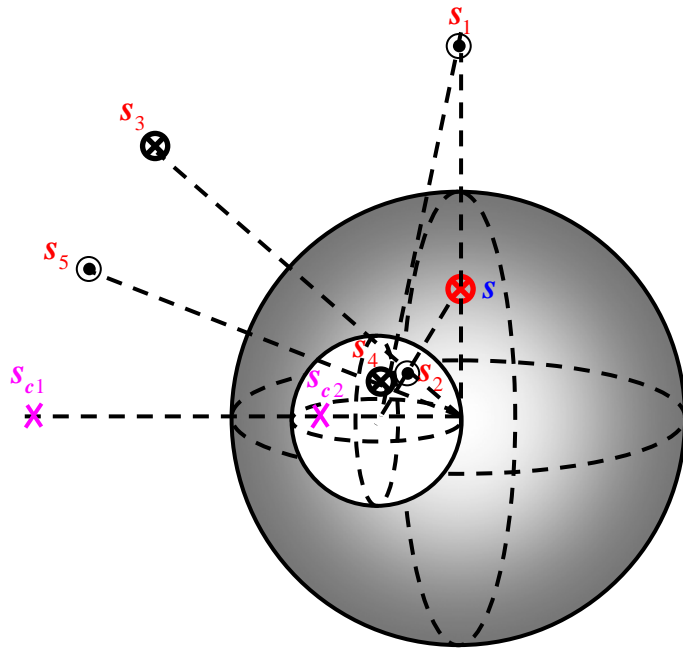
Figure 3-12 Successive image points of the non-concentric sphere and two frozen images at s_{c1} and s_{c2}.
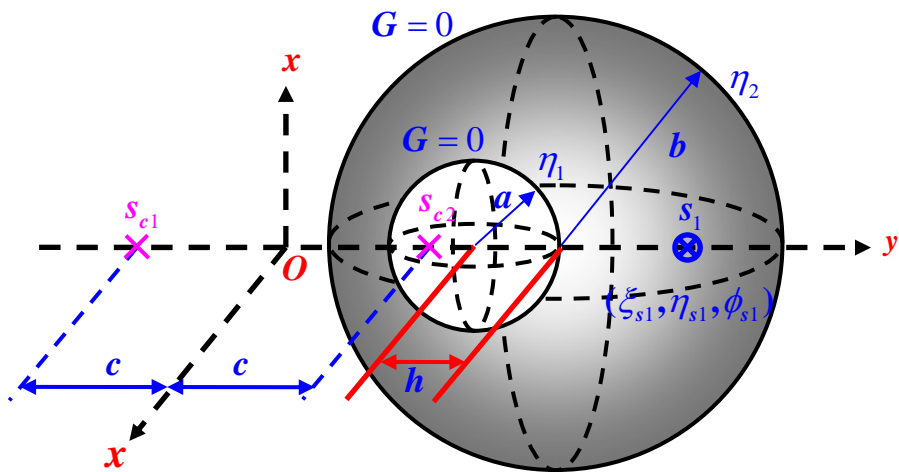
Figure 3-13 A non-concentric sphere with a concentrated source at the z axis.
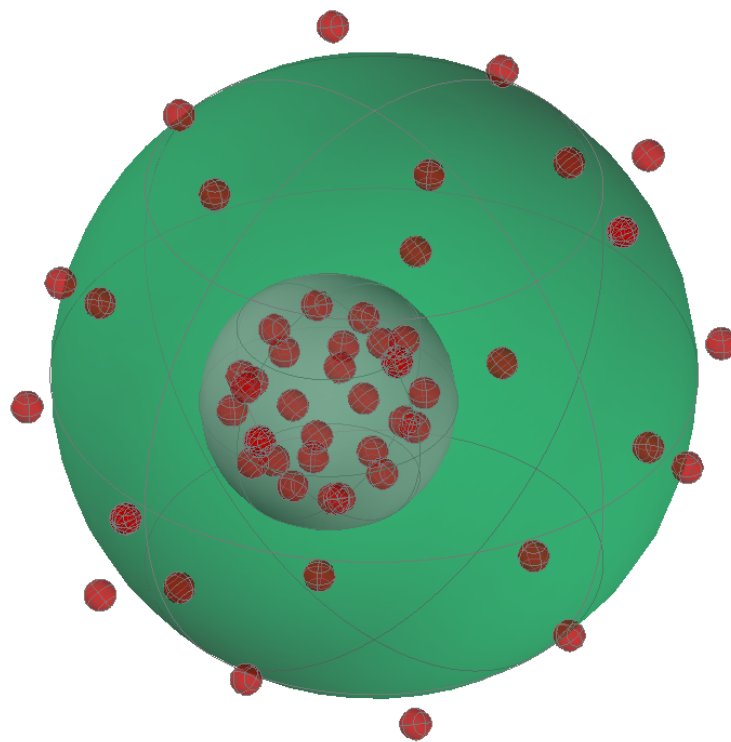
fictitious sources

Figure 3-14 Distribution of fictitious sources of the MFS.
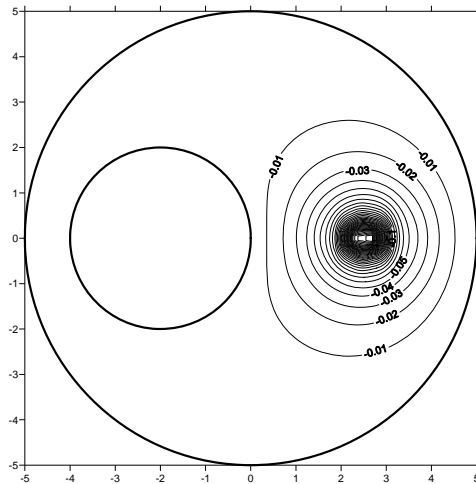
Figure 3-15(a) Potential contour by using the bispherical coordinates ($z = 0$ plane)
(an analytical solution).
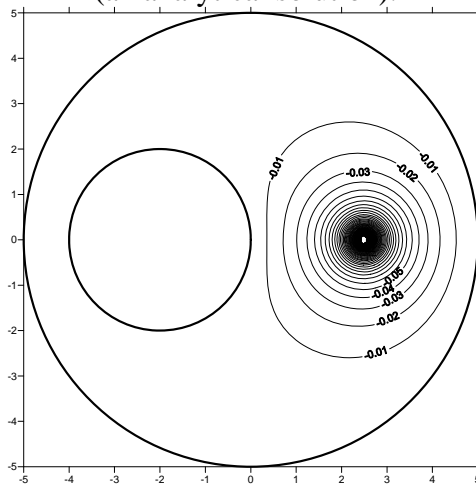
Figure 3-15(b) Potential contour by using the image method ($z = 0$ plane)
(a semi-analytical solution).
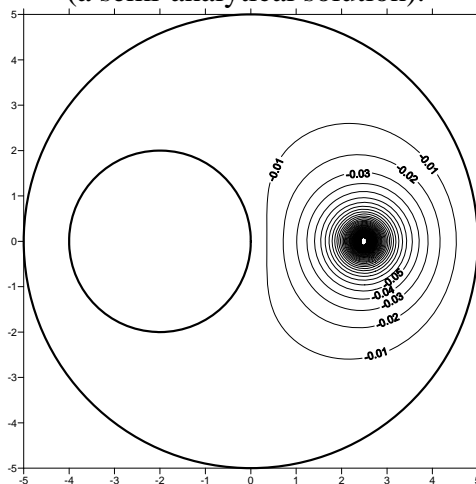
Figure 3-15(c) Potential contour by using the MFS ($z = 0$ plane)
(a numerical solution).

47
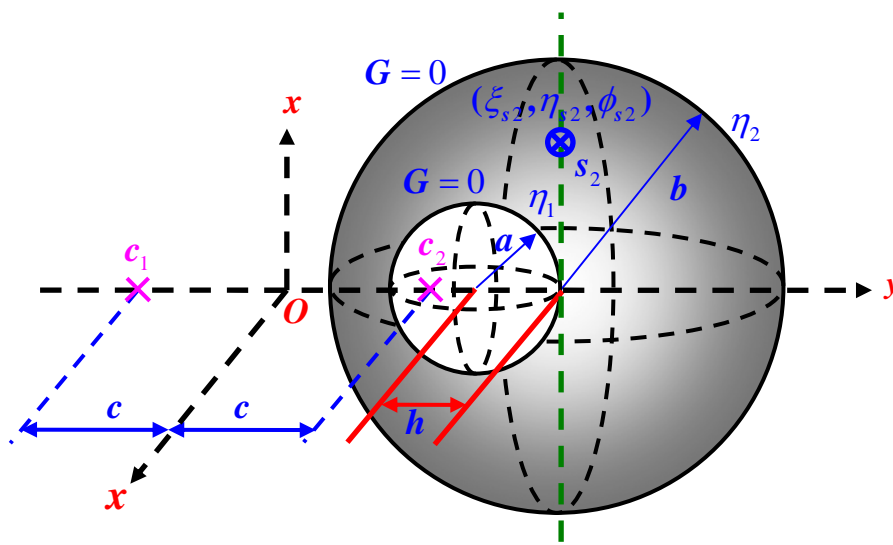
Figure 3-16 A non-concentric sphere with a concentrated source at $s_2 = (\xi_{s2}, \eta_{s2}, \phi_{s2})$.
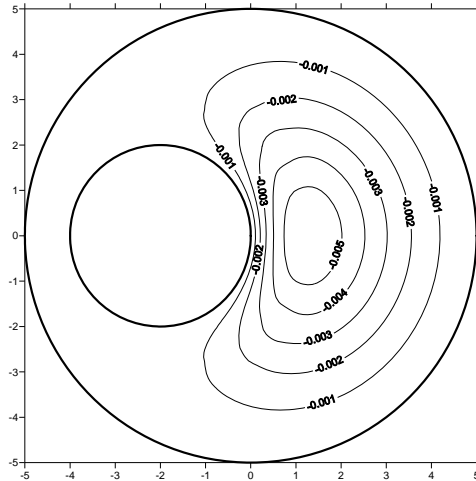
Figure 3-17(a) Potential contour by using the bispherical coordinates $(z = 0$ plane)

(an analytical solution).
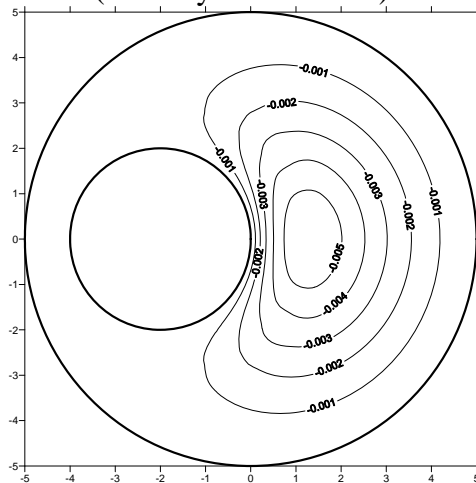
Figure 3-17(b) Potential contour by using the image method $(z = 0$ plane)

(a semi-analytical solution).
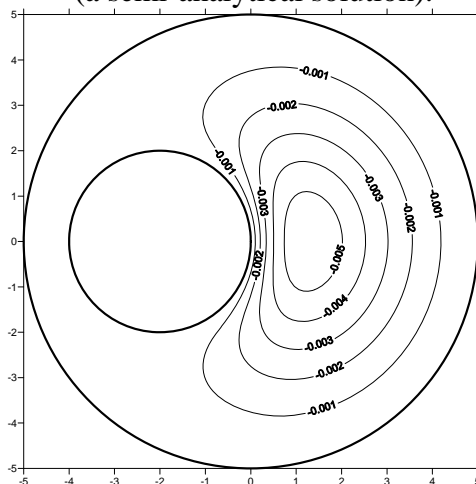
Figure 3-17(c) Potential contour by using the MFS $(z = 0$ plane)

(a numerical solution).

49

Chapter 4 Image solutions for boundary value problems without sources

Summary

In this chapter, we employ the image method to solve BVPs without sources. Two and three dimensional problems as well as symmetric and anti-symmetric cases are considered. By treating the image method as a special case of MFS, only at most four unknown strengths, distributed at the center, two locations of frozen images and one free constant, need to be determined. Besides, the optimal locations of sources are determined. For the symmetric and anti-symmetric cases, only two coefficients are required to match the two boundary conditions. The convergence rate versus number of image group is numerically performed. The differences of the image solutions between 2-D and 3-D problems are addressed. It is found that the two-dimensional solution in terms of the bipolar coordinates is mathematically equivalent to that of the simplest MFS with only two sources and one free constant. Finally, several examples are demonstrated to see the validity of the image method for BVPs.

4.1 Introduction

The image method is a popular approach in the theoretical physics [51] and has commonly been used in multidisciplines such as electro-magnetics, acoustics and optics. When solving problems by using the Green's functions for a bounded domain, the reflection is described by one or successive image sources, and the position and sign of the image sources is chosen so that the boundary conditions can be satisfied [7]. Green's function for a part of domain bounded by planes, circles or spherical surface in terms of the corresponding fundamental solution in the full space can be found in the literature [27]. In certain cases, it is possible to obtain the exact solution for a concentrated source in a domain through superimposing the infinite plane or infinite space solution for the given source and its image sources. Although the scope of this method is limited for

50

special geometry, it yields a great deal of insight into the solution when it works [38, 39]. As a result of the aforementioned consideration, many theoretical studies concerning the Green's function in circular and spherical boundaries have appeared in the literature. For example, Green's function for plane boundaries has been investigated [56]. The image method was employed to solve edge dislocation in an anisotropic film-substrate system [59] and dielectric plate [55]. Chen et al. [13, 14] solved Green's functions of annulus or concentric spheres by using the image method. It is found that almost all the related works on the image method deal with the problem with a true source in the domain. Although Cheng's book [22] has employed the image method to solve the boundary value problems (BVPs) of an infinite space with two spherical boundaries, the frozen image locations were not found to be the focuses of the bispherical coordinates. However, we may wonder whether the image method may work for BVPs without sources in the domain. Bispherical and bipolar coordinates were always used to derive the analytical solutions for problems containing boundaries of two spheres or circles [43], respectively. The BVPs of eccentric annulus were solved in a unified way of conformal mapping [17]. Problems with several circular boundaries were solved by using the null-field BIEM [16].

In this chapter, we will illustrate several examples to demonstrate the possible use of image method in solving 2-D and 3-D BVPs without sources. Symmetric, anti-symmetric and eccentric cases are considered. Based on the singularities distributed outside the domain for the image method, it can be seen as a special MFS with optimal locations and strengths of sources. To verify our image idea, analytical solutions by using the bipolar and bispherical coordinates are used to check the accuracy of our results. Besides, numerical results using the conventional MFS and null-field BIEM are also given for comparison. An infinite space with two spherical cavities as well as an infinite plane with two circular holes are both considered. Besides, an eccentric sphere is also given. Also, the static result for a limiting case of two-spheres radiation to simulate Laplace problems is provided for comparison.

4.2 Derivation of the image solution for BVPs

4.2.1 3-D BVP

The problem of an infinite space with two spherical cavities is shown in Fig. 4-1 and the governing equation is

$$\nabla^2 u(x) = 0,\ x \in D, \tag{4-1}$$

where ∇^2 is the Laplacian, $u(x)$ is the potential function and D is the domain of interest. For a two-spheres case, the boundary conditions are

$$u(x) = V_1,\ x \in B_1, \tag{4-2}$$

$$u(x) = V_2,\ x \in B_2, \tag{4-3}$$

where B_1 and B_2 are left and right spherical boundaries with boundary data of V_1 and V_2, respectively. In this case, the analytical solution [43] was derived in terms of the bispherical coordinates as shown below:

$$u(\xi,\eta) = \sqrt{2\cosh\eta - 2\cos\xi} \sum_{n=0}^{\infty} \left[\left(\frac{V_2 + V_1}{2} \right) \frac{\cosh(n + \frac{1}{2})\eta}{\cosh(n + \frac{1}{2})\eta_0} \right. \\ \left. + \left(\frac{V_2 - V_1}{2} \right) \frac{\sinh(n + \frac{1}{2})\eta}{\sinh(n + \frac{1}{2})\eta_0} \right] e^{-(n + \frac{1}{2})\eta_0} P_n(\cos\xi), \tag{4-4}$$

where $\xi = $ constant is a family of spindle-shaped surfaces passing through the poles $(0, \pm c, 0)$, η_0 is on the right spherical boundary, $\eta = $ constant shows a surface of $\ln(r_{c1}/r_{c2}) = $ constant, and $P_n(\bullet)$ is the Legendre polynomial. It contains both symmetric and anti-symmetric problems.

The problem of infinite space with two spherical cavities can be seen as a combination of symmetric and anti-symmetric problems as shown in Fig. 4-2(a) and (b). The fundamental solution of the three-dimensional Laplace equation is shown below:

$$U(x,s) = \frac{-1}{r}, \tag{4-5}$$

52

where r is the distance between the source point s and the field point x ($r \equiv |x-s|$). For the symmetric case, we derive the solution by using the image concept. To satisfy the nonhomogeneous boundary conditions (BCs) on the two spherical surfaces, both artificial sources at the two centers outside the domain are initiated in advance. However, the source at the left (right) center also results a nonzero potential on the right (left) boundary. Therefore, successive images are required to construct the solution as given below:

$$u(x) = \lim_{N \to \infty} \left\{ q^s(N) \left[\left(\frac{1}{r_{o1}} + \frac{1}{r_{o2}} \right) + \sum_{i=1}^{N} \left(\frac{-w_{4i-3}}{|x-s_{4i-3}|} - \frac{w_{4i-2}}{|x-s_{4i-2}|} + \frac{w_{4i-1}}{|x-s_{4i-1}|} + \frac{w_{4i}}{|x-s_{4i}|} \right) \right] \right.$$
$$\left. + \frac{c_1^s(N)}{|x-s_{c_1}|} + \frac{c_2^s(N)}{|x-s_{c_2}|} \right\},$$
(4-6)

where three coefficients of symmetric case, $q^s(N)$, $c_1^s(N)$ and $c_2^s(N)$ are required to be determined by matching the boundary conditions, r_{o1} and r_{o2} are the distances between center and field point. Two frozen images, s_{c1} and s_{c2}, are found after successive images. The locations of two frozen images must simultaneously satisfy

$$\frac{d}{2} + R_{c2} = \frac{a^2}{\left(\frac{d}{2} - R_{c1} \right)}, \quad R_{c1} = R_{c2},$$
(4-7)

where a, d, R_{c1} and R_{c2} are shown in Fig. 4-2. The distance between the two focuses is denoted by

$$|R_{c1} + R_{c2}| = 2c.$$
(4-8)

The parameter c is the half distance between the two focuses in the bispherical coordinates which can be obtained by:

$$c = \frac{\sqrt{d^2 - 4a^2}}{2}.$$
(4-9)

The w_k in Eq. (4-6) is the weighting of the kth image source that can be obtained by using the formula of image location [14] as shown below:

$$w_1 = \frac{a}{d}, \qquad w_5 = \frac{aw_4}{d - R_4}, \cdots, w_{4i-3} = \frac{aw_{4i-4}}{d - R_{4i-4}},$$

$$w_2 = \frac{a}{d}, \qquad w_6 = \frac{aw_3}{R_3}, \cdots\cdots, w_{4i-2} = \frac{aw_{4i-5}}{R_{4i-5}},$$

$$w_3 = \frac{aw_2}{d - R_2}, \; w_7 = \frac{aw_6}{d - R_6}, \cdots, w_{4i-1} = \frac{aw_{4i-2}}{d - R_{4i-2}}, \qquad (4\text{-}10)$$

$$w_4 = \frac{aw_1}{R_1}, \qquad w_8 = \frac{aw_5}{R_5}, \cdots\cdots, w_{4i} = \frac{aw_{4i-3}}{R_{4i-3}}, \qquad i = 2, 3, \ldots, \infty,$$

where R_k is the distance between the kth image source and the center of left cavity, and they are determined by the recurrence relation

$$R_1 = d - \frac{a^2}{d}, \qquad R_5 = d - \frac{a^2}{d - R_4}, \cdots, R_{4i-3} = d - \frac{a^2}{d - R_{4i-4}},$$

$$R_2 = \frac{a^2}{d}, \qquad R_6 = \frac{a^2}{R_3}, \cdots\cdots\cdots, R_{4i-2} = \frac{a^2}{R_{4i-5}},$$

$$R_3 = d - \frac{a^2}{d - R_2}, \; R_7 = d - \frac{a^2}{d - R_6}, \cdots, R_{4i-1} = d - \frac{a^2}{d - R_{4i-2}}, \qquad (4\text{-}11)$$

$$R_4 = \frac{a^2}{R_1}, \qquad R_8 = \frac{a^2}{R_5}, \cdots\cdots\cdots, R_{4i} = \frac{a^2}{R_{4i-3}}, \qquad i = 2, 3, \ldots, \infty.$$

Here, the image solution for an anti-symmetric problem is shown below:

$$u(x) = \lim_{N \to \infty} \left\{ q^a(N) \left[\left(\frac{-1}{r_{o1}} + \frac{1}{r_{o2}} \right) + \sum_{i=1}^{N} \left(\frac{-w_{4i-3}}{|x - s_{4i-3}|} + \frac{w_{4i-2}}{|x - s_{4i-2}|} - \frac{w_{4i-1}}{|x - s_{4i-1}|} + \frac{w_{4i}}{|x - s_{4i}|} \right) \right] \right.$$

$$\left. + \frac{c_1^a(N)}{|x - s_{c_1}|} + \frac{c_2^a(N)}{|x - s_{c_2}|} \right\}, \qquad (4\text{-}12)$$

where the coefficients of the anti-symmetric case, $q^a(N)$, $c_1^a(N)$ and $c_2^a(N)$, are required to be determined by matching the boundary condition, $q^s(N)$ and $q^a(N)$ are the initial strengths for symmetric and anti-symmetric cases, respectively, which can be determined later by matching the boundary conditions. Successive images for the symmetric and anti-symmetric cases were shown in Fig. 4-2.

4.2.2 2-D BVP

Let us consider an infinite plane with two circular holes subject to the anti-symmetric boundary condition. Similarly, the two-dimensional anti-symmetric problem is solved by using the image method in a similar way of three-dimensional case. The fundamental solution of the two-dimensional Laplace equation is given below:

$$U(x,s) = \ln(r).\tag{4-13}$$

For the anti-symmetric case, the boundary conditions are

$$u(x) = V_1 = -V,\ x \in B_1,\tag{4-14}$$

$$u(x) = V_2 = V,\ x \in B_2,\tag{4-15}$$

where B_1 and B_2 are left and right circular boundaries with boundary data of V_1 and V_2, respectively. Therefore, the image solution for the two-dimensional anti-symmetric problem in Fig. 4-3 can be constructed as

$$u(x) = \lim_{N \to \infty} \{ q(N)[(-\ln r_{o1} + \ln r_{o2})$$
$$+ \sum_{i=1}^{N} (\ln|x - s_{4i-3}| - \ln|x - s_{4i-2}| + \ln|x - s_{4i-1}| - \ln|x - s_{4i}|)]$$
$$+ c_1(N)\ln|x - s_{c_1}| + c_2(N)\ln|x - s_{c_2}| + e(N) \},\tag{4-16}$$

where $q(N)$ is an initial strength at the two centers of circular hole which can be determined later by matching the boundary conditions, s_{c1} and s_{c2} are two locations of final two frozen images which are similar to the three-dimensional case, $c_1(N)$ and $c_2(N)$ are their corresponding strengths, $e(N)$ is the rigid body term, the iterative images and their locations are shown in Fig. 4-3. The exact solution [43] in terms of the bipolar coordinates is given below:

$$u(\xi, \eta) = \frac{V}{\ln|r_1 / r_2|} \eta = \frac{V}{\eta_0} \eta.\tag{4-17}$$

4.3 Illustrative examples and discussions

4.3.1 3-D problems

Case 1: An infinite space with two spherical cavities subject to symmetric boundary conditions (symmetric problem of $V_1=V_2=V=1$)

In the first case, the problem sketch for an infinite space with two spherical cavities is shown in Fig. 4-4. The centers of two cavities are set at (0, -2.5, 0) and (0, 2.5, 0), and the radii are both 1. By matching the boundary conditions, the analytical solution [43] can be simplified by using Eq. (4-4) as given below:

55

$$u(\xi,\eta) = \sqrt{2\cosh\eta - 2\cos\xi} \sum_{n=0}^{\infty} \left[V \frac{\cosh(n+\frac{1}{2})\eta}{\cosh(n+\frac{1}{2})\eta_0} \right] e^{-(n+\frac{1}{2})\eta_0 P_n(\cos\xi)}. \tag{4-18}$$

By matching the boundary conditions, all the unknown coefficients in Eq. (4-6), $q^s(N)$, $c_1^s(N)$ and $c_2^s(N)$, can be determined as shown in Fig. 4-5. In the numerical experiment, we found that the coefficient of $q^s(N)$ is equal to 1, since the 3-D fundamental solution is $-1/r$ where r is the distance between s and x ($r \equiv |x-s|$), $\lim_{N\to\infty} c_1^s(N) = 0$ and $\lim_{N\to\infty} c_2^s(N) = 0$. Finally, we can find that the final frozen image points terminate at the focuses of the bispherical coordinates. The contour plots by using Eq. (4-6) the image method Eq. (4-18) in terms of and the bispherical coordinates are shown in Fig. 4-6. It can be observed that our results are compared well with the analytical solution. Also, the static result for limiting solution of two-spheres radiation by using the null-field BIEM [45] is provided for comparison. Good agreement is also made.

Case 2: An infinite space with two spherical cavities subject to anti-symmetric boundary conditions (anti-symmetric problem of $V_1 = -V = -1$, $V_2 = V = 1$)

Figure 4-7 is a sketch of an infinite space with two spherical cavities subject to anti-symmetry boundary conditions instead of the above symmetric case. The geometry data are the same as the case 1 and the analytical solution is obtained as follows:

$$u(\xi,\eta) = \sqrt{2\cosh\eta - 2\cos\xi} \sum_{n=0}^{\infty} \left[V \frac{\sinh(n+\frac{1}{2})\eta}{\sinh(n+\frac{1}{2})\eta_0} \right] e^{-(n+\frac{1}{2})\eta_0 P_n(\cos\xi)}. \tag{4-19}$$

In a similar way of finding the successive images for matching the boundary conditions, the solution can be obtained by using Eq. (4-12). After locating boundary points to match the boundary conditions, all the unknown coefficients, $q^a(N)$, $c_1^a(N)$ and $c_2^a(N)$, versus N can be determined as shown in Fig. 4-8. Similarly, we also found that the final frozen image points happen to be the focuses of the bispherical coordinates. The contour plots by using Eq. (4-12) in the image method and Eq. (4-19) of the analytical solution are shown in Fig. 4-9. The results of our approach are compared well

with the analytical solution by using the bispherical coordinates. Also, the static result for limiting solution of two-spheres radiation using the null-field BIEM [45] is provided for comparison. Good agreement is also made.

Case 3: A non-concentric sphere (V_1=0, V_2=1)

In this case, the two radii of inner and outer spheres are $a = 1$ and $b = 2.5$, respectively. The distance d between the two centers is equal to 1 as shown in Fig. 4-10. After successive images, the image solution can be obtained as shown below:

$$u(x) = \lim_{N \to \infty} \left\{ q(N) \left[\frac{-1}{r} + \sum_{i=1}^{N} \left(\frac{-w_{2i-1}}{|x - s_{2i-1}|} + \frac{w_{2i}}{|x - s_{2i}|} \right) \right] + \frac{c_1(N)}{|x - s_{c_1}|} + \frac{c_2(N)}{|x - s_{c_2}|} + e(N) \right\}. \qquad (4\text{-}20)$$

Since the center of outer sphere is in the domain, we only put an artificial source at the center of inner sphere to satisfy the governing equation. Similarly, two frozen images are found after successive images. The locations of two frozen images are governed by

$$R_{c1} = \frac{b^2}{R_{c2} - d} + d, \ R_{c2} = \frac{a^2}{R_{c1}}, \qquad (4\text{-}21)$$

where R_{c1} and R_{c2} are the y coordinates for the left and right focuses, respectively, as shown in Fig. 4-11. The distance between the two focuses is denoted by

$$|R_{c1} - R_{c2}| = 2c. \qquad (4\text{-}22)$$

The parameter c is the half distance between two focuses in the bispherical coordinates which can be obtained by:

$$c = \frac{\sqrt{a^4 - 2a^2b^2 + b^4 - 2a^2d^2 - 2b^2d^2 + d^4}}{2d}. \qquad (4\text{-}23)$$

After matching the boundary conditions, the unknown coefficients, $q(N)$, $c_1(N)$, $c_2(N)$ and $e(N)$, versus N are shown in Fig. 4-12. The frozen images happen to be the two focuses in the bispherical coordinates. The analytical solution [12] obtained by using the bispherical coordinates is

$$u(\xi, \eta) = \sqrt{2 \cosh \eta - 2 \cos \xi}$$

$$\sum_{n=0}^{\infty} \left[\frac{V_1 \left(e^{2(n+\frac{1}{2})\eta} - e^{2(n+\frac{1}{2})\eta_2} \right) - V_2 \left(e^{2(n+\frac{1}{2})\eta} - e^{2(n+\frac{1}{2})\eta_1} \right)}{e^{2(n+\frac{1}{2})\eta_1} - e^{2(n+\frac{1}{2})\eta_2}} \right] e^{-(n+\frac{1}{2})\eta} P_n(\cos \xi). \qquad (4\text{-}24)$$

Figures 4-13(a), (b) and (c) show the potential contours by using the image method, the bispherical coordinates and the method of fundamental solutions, respectively. It is found that the results of three approaches match well with each other.

4.3.2 2-D problems

Case 4: An infinite plane with two circular holes subject to anti-symmetric BCs ($V_1=-V=-1$, $V_2=V=1$)

It is interesting to find that $q(N)$ for 3-D case can be obtained in advance to fit the boundary condition. We may wonder whether the $q(N)$ of the 2-D problem can be determined in the same way as 3-D case. The problem sketch for an infinite plane with two circular holes subject to anti-symmetric boundary conditions is shown in Fig. 4-14. The distance between the centers of two circular holes is 10, and the radii of two holes are both 1. The frozen images happen to be the two focuses in the bipolar coordinates. After matching the boundary conditions in Eqs. (4-14) and (4-15), the unknown coefficients of $q(N)$, $c_1(N)$, $c_2(N)$ and $e(N)$ versus N are shown in Fig. 4-15. It is interesting to find that the strengths of $q(N)$ and $e(N)$ are zero. Besides, we also observe that $c_1(N)=-c_2(N)$ in numerical experiment and therefore the image solution of the anti-symmetrical case can be written as

$$u(x) = c_1(N)\left[\ln\left|x-s_{c_1}\right| - \ln\left|x-s_{c_2}\right|\right],$$
(4-25)

where the coefficient $c_1(N)$ is determined by matching the boundary condition $\left.(u(x)\right|_{x\in B_2} = V = 1)$ as given below:

$$c_1(N) = \frac{V}{\ln\left|x-s_{c_1}\right| - \ln\left|x-s_{c_2}\right|}, \quad x \in B_2,$$
(4-26)

in which $c_1(N)$ is found to be a constant and is independent of N. It indicates that the analytical solution by using the bipolar coordinates is the same as that of image method (special MFS) with only two sources as follows:

$$u(\xi,\eta) = \frac{V}{\sinh^{-1}\left(\dfrac{c}{a}\right)}\eta.$$
(4-27)

Figures 4-16(a), (b) and (c) show the potential contours by using the image method, the bipolar coordinates and the null-field BIEM [16], respectively. Good agreement of the

58

three approaches is made.

Case 5: An eccentric annulus [16]

The problem sketch for an eccentric annulus is shown in Fig. 4-17 with $V_1=0$ and $V_2=1$. The two of inner and outer circular holes are $a=1$ and $b=2.5$, respectively. The distance d between the two centers is equal to 1. This problem has been solved by using several approaches and a unified point of view by using the conformal mapping was provided in [17]. By putting successive images, the image solution can be obtained as below:

$$u(x) = \lim_{N \to \infty} \{ q(N)[\ln r + \sum_{i=1}^{N}(-\ln|x - s_{2i-1}| + \ln|x - s_{2i}|)]$$
$$+ c_1(N)\ln|x - s_{c_1}| + c_2(N)\ln|x - s_{c_2}| + e(N) \}. \tag{4-28}$$

The coefficients of $q(N)$, $c_1(N)$, $c_2(N)$ and $e(N)$ versus N are shown in Fig. 4-18. The analytical solution obtained by using the bipolar coordinates is given below:

$$u(\xi, \eta) = A\eta + B, \tag{4-29}$$

where

$$A = \frac{V_1 - V_2}{\sinh^{-1}\left(\dfrac{c}{a}\right) - \sinh^{-1}\left(\dfrac{c}{b}\right)}, \tag{4-30}$$

$$B = V_1 - \frac{V_1 - V_2}{\sinh^{-1}\left(\dfrac{c}{a}\right) - \sinh^{-1}\left(\dfrac{c}{b}\right)} \sinh^{-1}\left(\dfrac{c}{a}\right). \tag{4-31}$$
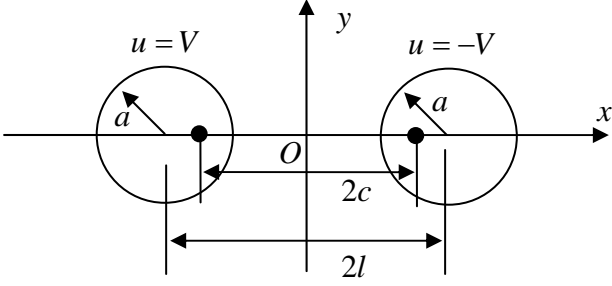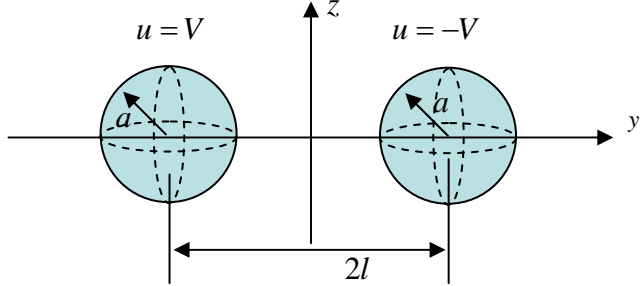
It is also found that the solution derived by the image method and the MFS with only two sources are the same as the analytical solution derived by using bipolar coordinates. Figures 4-19(a), (b) and (c) show the potential contours by using the image method, the bipolar coordinates and the null-field BIEM, respectively. The frozen images happen to be the two focuses in the bipolar coordinates. It is found that the results of three approaches match well. In this case, the optimal number of sources in the MFS is only two and the two positions are found to be exactly located on the focuses in the bipolar coordinates. The image method in this case can be seen as an optimal and simple MFS.

For the 3-D case, the successive strengths become smaller and the final strengths at the two frozen points approach zero for sufficiently large number of images. However, the 2-D case is quite different, i.e., the strengths at the two centers are not $1/\ln(a)$ which satisfies the boundary condition ($u=\ln(a)/\ln(a)=1$). Only two singularities at the two focuses are required. In the cases of 4 and 5, we found the equivalence between the image solution and the analytical solution derived by using the separation of variables in the bipolar coordinates. Table 4-1 shows the comparison of the anti-symmetric problem between two-dimensional and three-dimensional cases. The image method can be seen as a simple MFS in the 2-D case. For the five (2-D and 3-D) cases, all frozen images merge at the focuses.

4.4 Conclusions

In this chapter, five solutions for the two and three dimensional BVPs were obtained by using the image method. For the 3-D case, we have found the strengths of the two initial sources at the two centers that can be determined in advance to satisfy its own boundary condition. The strengths of successive images are then calculated and their values become smaller and smaller. The final strengths of frozen images approach zero for sufficiently large number of successive images. However, the finding in the 3-D case can not be directly applied to the 2-D case. Nonzero strengths at the frozen images are found and the initial strengths of sources at the centers are zero. The image method can provide optimal locations and specified weightings for the conventional MFS. The dimension of the matrix in the linear algebraic equation is at most four by four in the all examples. Agreement is made after comparing the image solution with those of the conventional MFS, the null-field BIEM, the analytical solutions by using the bipolar (2-D) and the bispherical (3-D) coordinates and the static result for limiting case of two-spheres radiation by using the null-field BIEM.

Table 4-1 Anti-symmetric problem of 2-D and 3-D.

Domain	2-D problem	3-D problem
Figure sketch		
Image solution	$u(x) = \lim\limits_{N \to \infty} \{ q(N)[(-\ln r_{o1} + \ln r_{o2})$ $+ \sum\limits_{i=1}^{N} (\ln|x - s_{4i-3}| - \ln|x - s_{4i-2}| + \ln|x - s_{4i-1}| - \ln|x - s_{4i}|)]$ $+ c_1(N)\ln|x - s_{c1}| + c_2(N)\ln|x - s_{c2}|\}$	$u(x) = \lim\limits_{N \to \infty} \left\{ q^a(N)\left[\left(\dfrac{-1}{r_{o1}} + \dfrac{1}{r_{o2}} \right) + \sum\limits_{i=1}^{N} \left(\dfrac{-w_{4i-3}}{|x - s_{4i-3}|} + \dfrac{w_{4i-2}}{|x - s_{4i-2}|} \right. \right. \right.$ $\left. \left. \left. - \dfrac{w_{4i-1}}{|x - s_{4i-1}|} + \dfrac{w_{4i}}{|x - s_{4i}|} \right) \right] + \dfrac{c_1^a(N)}{|x - s_{c_1}|} + \dfrac{c_2^a(N)}{|x - s_{c_2}|} \right\}$
	$q(N) = 0$	$q^a(N) = aV$
Value of coefficient	$c_1(N) = \dfrac{V}{\sinh^{-1}(\dfrac{c}{a})}$, $c_2(N) = \dfrac{-V}{\sinh^{-1}(\dfrac{c}{a})}$	$\lim\limits_{N \to \infty} c_1^a(N) = \lim\limits_{N \to \infty} c_2^a(N) = 0$
Key images	Focus dominant	Pole dominant
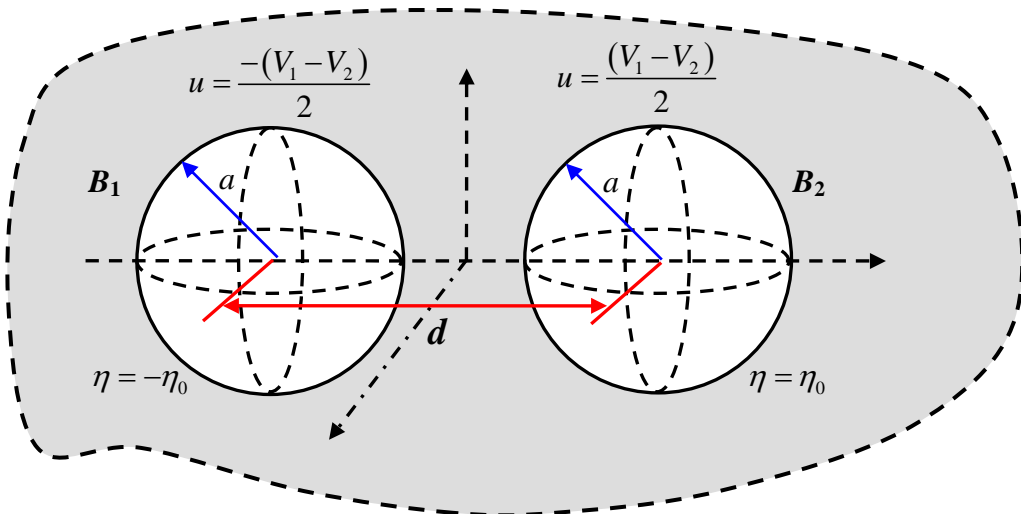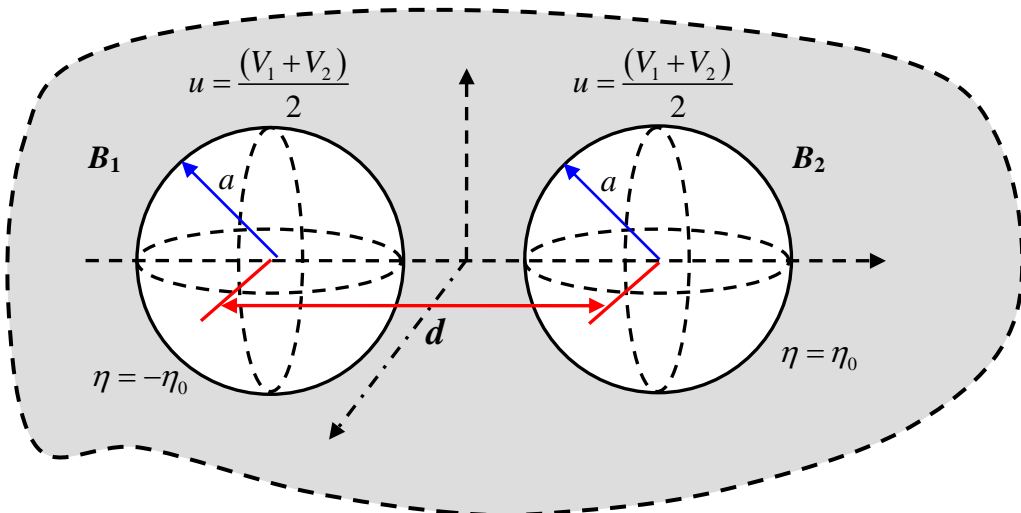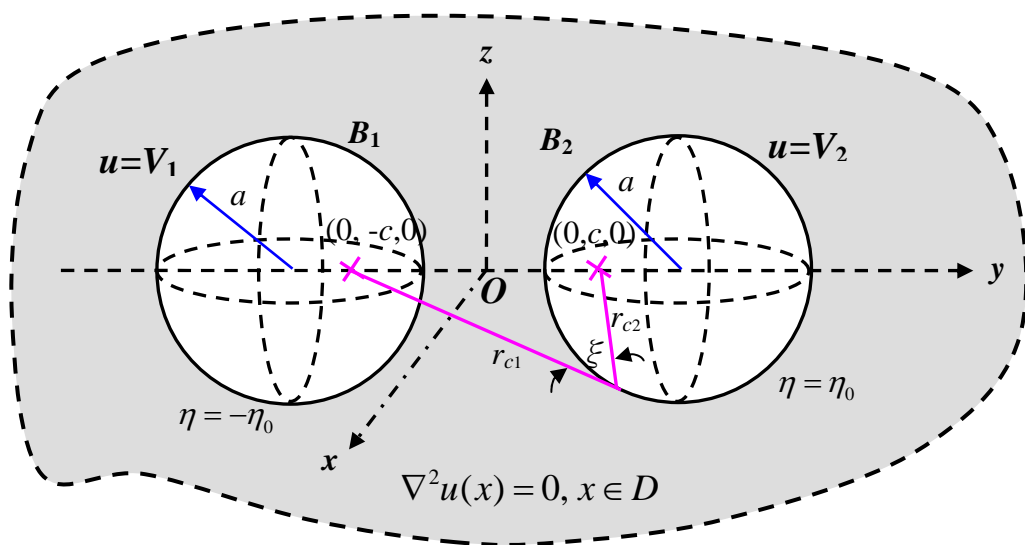
(a) symmetric case

(b) anti-symmetric case

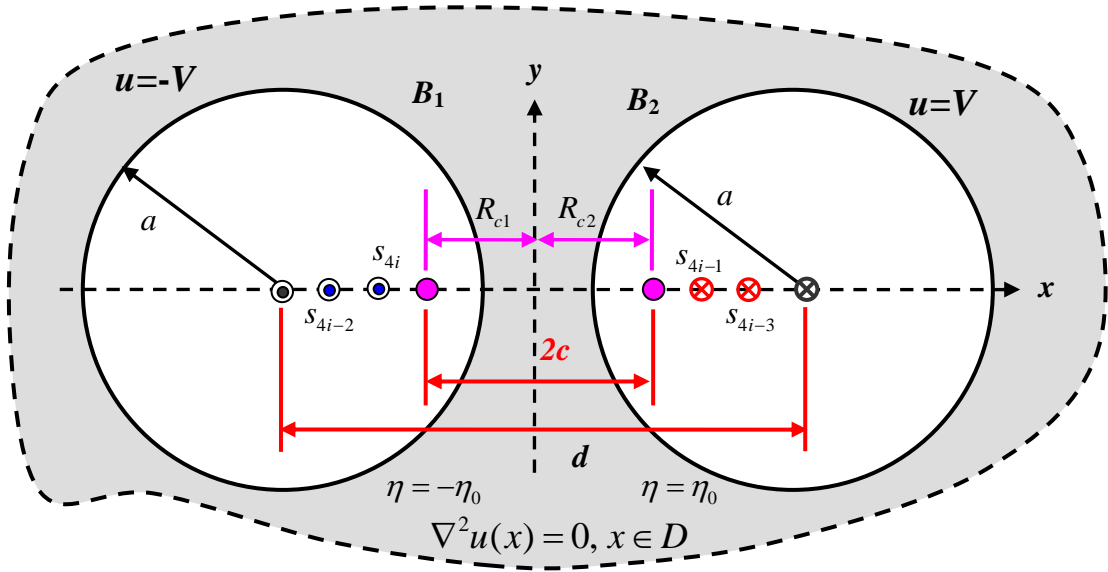Figure 4-2 Successive images for the (a) symmetric and (b) anti-symmetric cases.
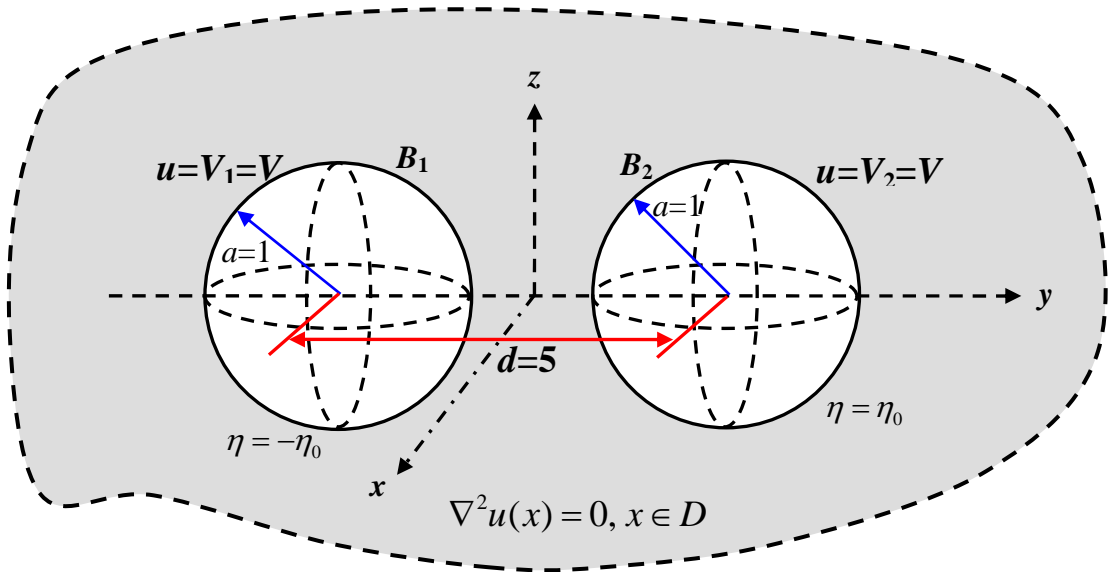
Figure 4-3 Images locations for the 2-D anti-symmetric case.

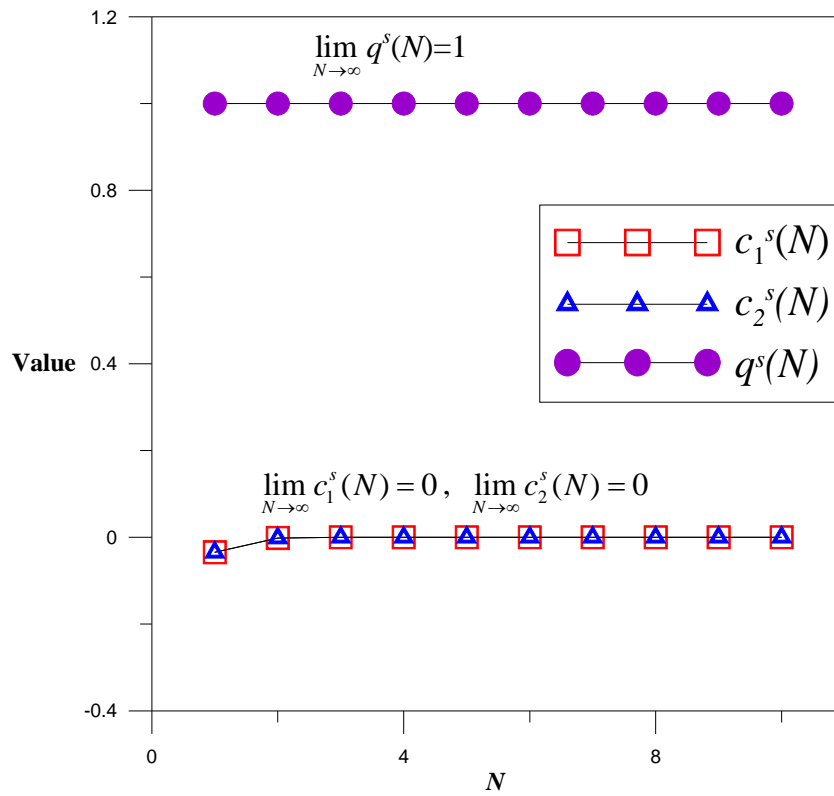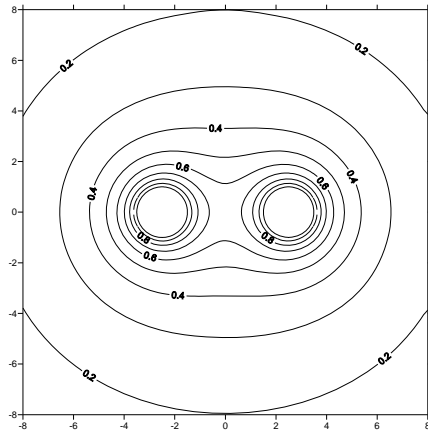

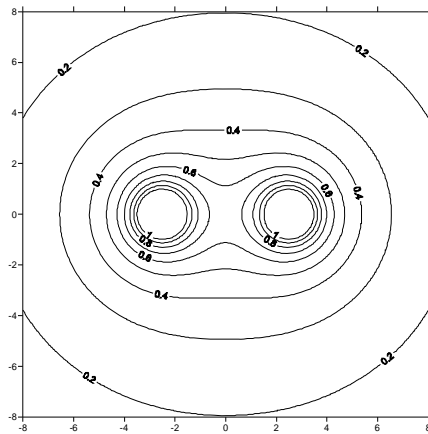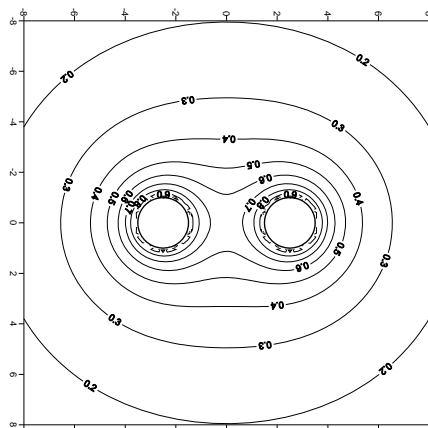Figure 4-4 Problem sketch for the 3-D symmetric problem.

Figure 4-5 Coefficients of $q^s(N)$, $c_1^s(N)$ and $c_2^s(N)$ versus N for an infinite space with two spherical cavities subject to the symmetric boundary condition.

(a) an image solution

(b) an analytical solution using the bispherical coordinates

(c) a limiting case of static solution using the null-field
Figure 4-6 Potential contours (a) an image solution, (b) an analytical solution using the bispherical coordinates and (c) a limiting case of static solution using the null-field BIEM [45] (*x-y* plane).
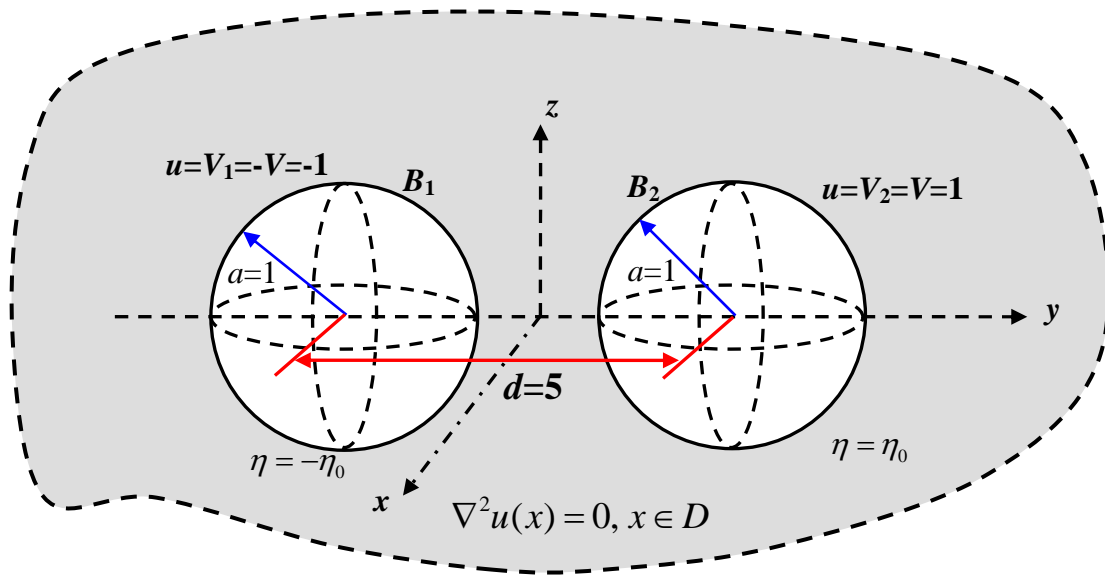
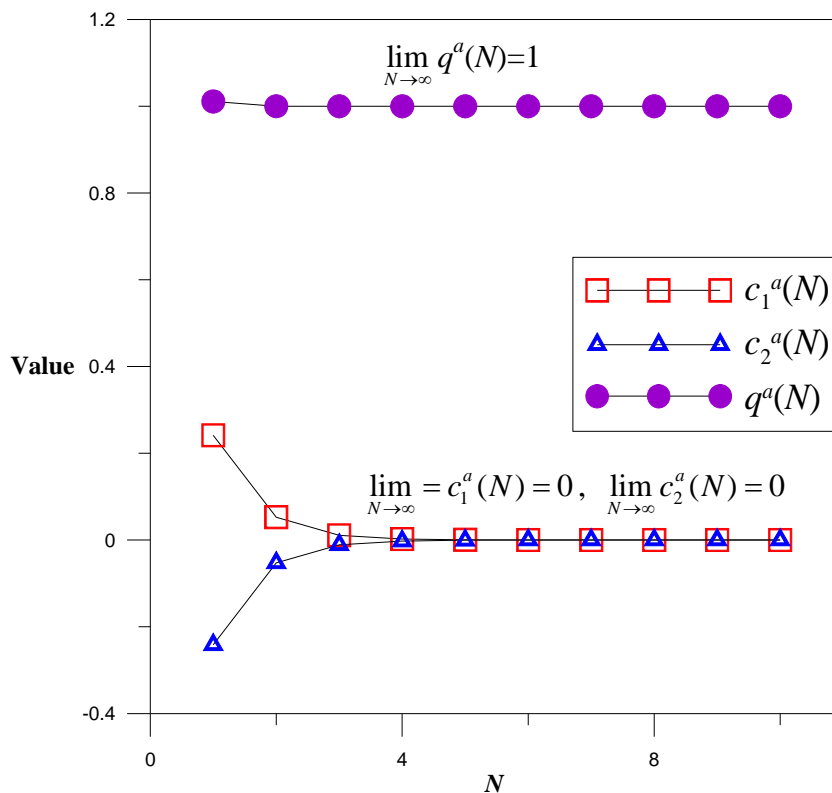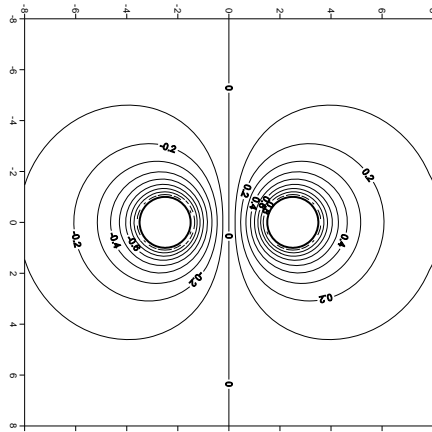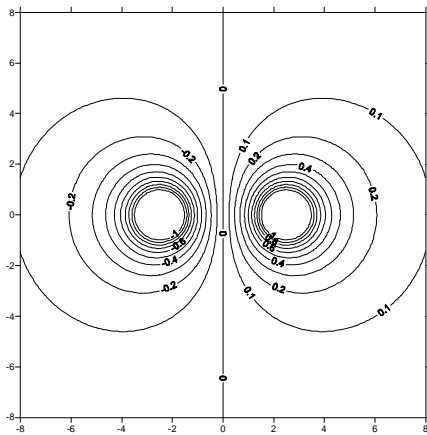Figure 4-7 Problem sketch for the 3-D anti-symmetric problem.

Figure 4-8 Coefficients of $q^a(N)$, $c_1^a(N)$ and $c_2^a(N)$ versus N for an infinite space with two spherical cavities subject to the anti-symmetry boundary condition.

(a) an image solution

(b) an analytical solution using the bispherical coordinates
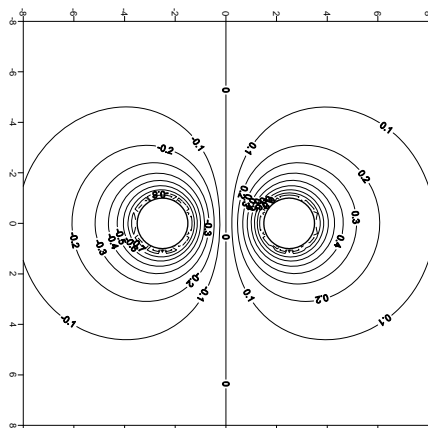
(c) a limiting case of static solution using the null-field
Figure 4-9 Potential contours (a) an image solution, (b) an analytical solution using the bispherical coordinates and (c) a limiting case of static solution using the null-field BIEM [45] (*x-y* plane).
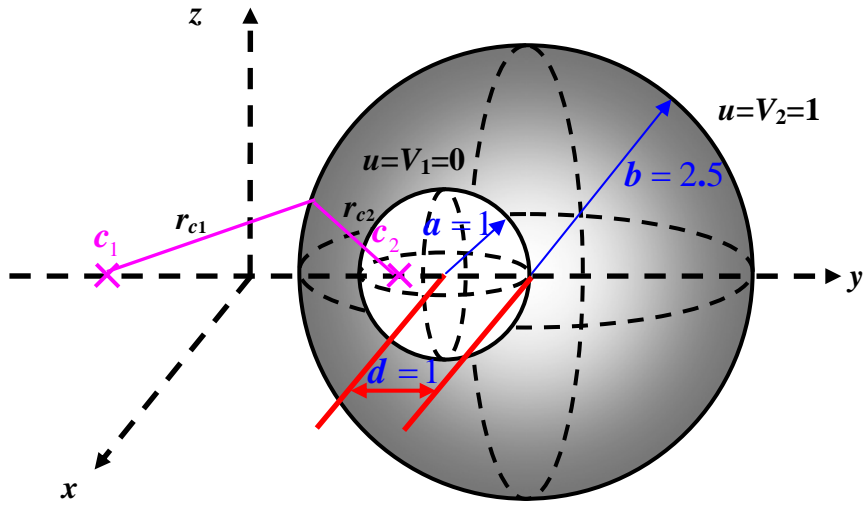
Figure 4-10 Sketch for the problem of non-concentric spheres.
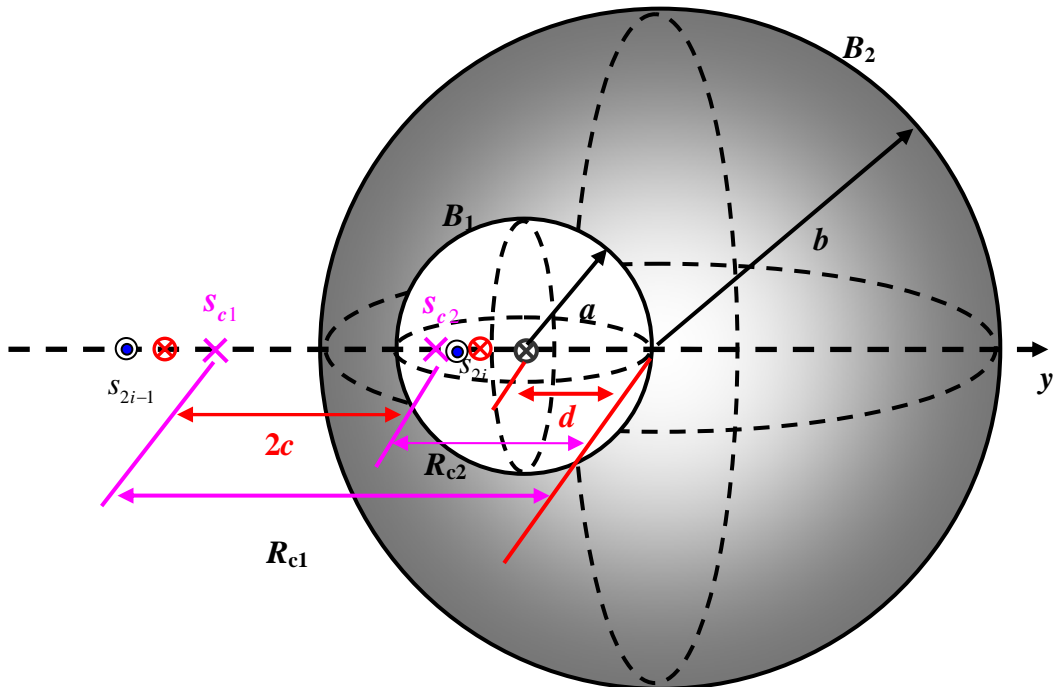
Figure 4-11 Image location for the problem of the non-concentric spheres.
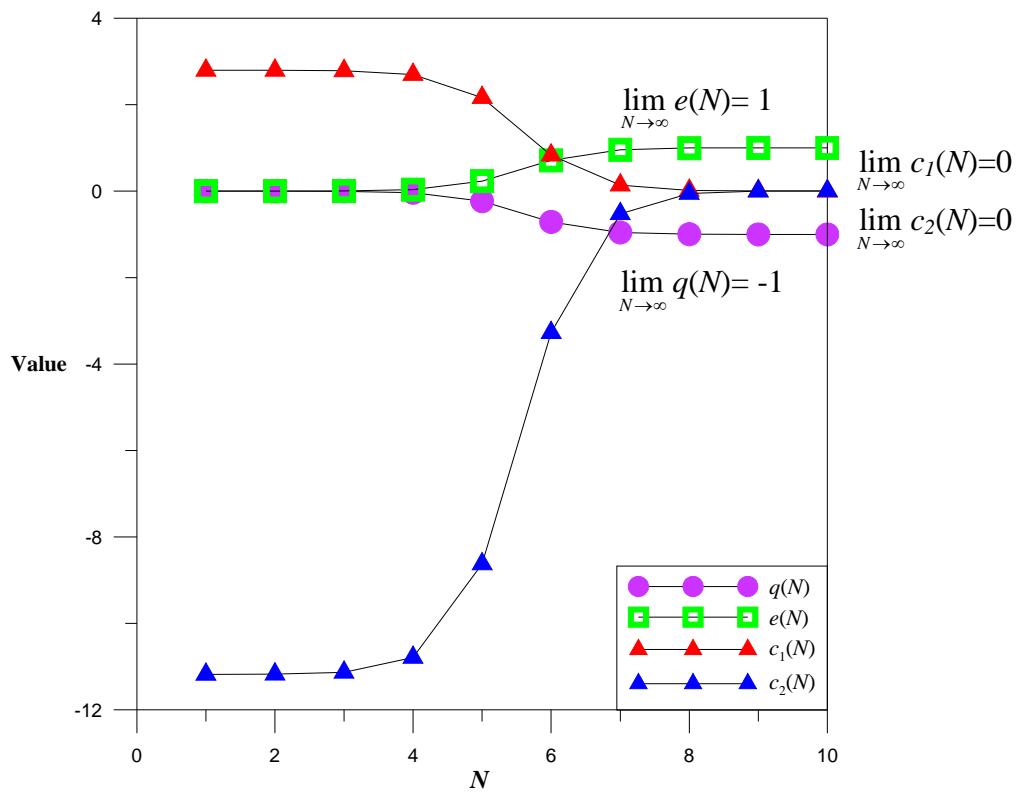
Figure 4-12 Coefficients of $q(N)$, $c_1(N)$, $c_2(N)$ and $e(N)$ versus N for the non-concentric spherical problem.

(a) an image solution

(b) an analytical solution using the bispherical coordinates

(c) a solution by using the MFS

Figure 4-13 Potential contours (a) an image solution, (b) an analytical solution using the bispherical coordinates [12] and (c) a solution by using the MFS (*x-y* plane).
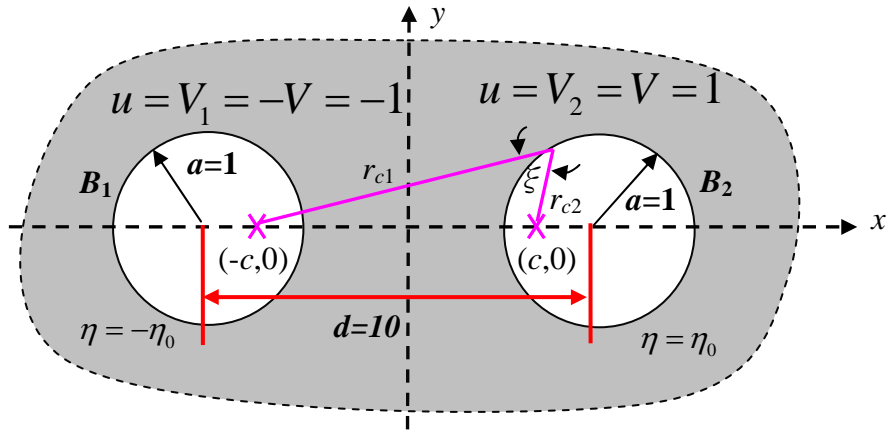
Figure 4-14 An infinite plane with two circular holes in the bipolar coordinate system.
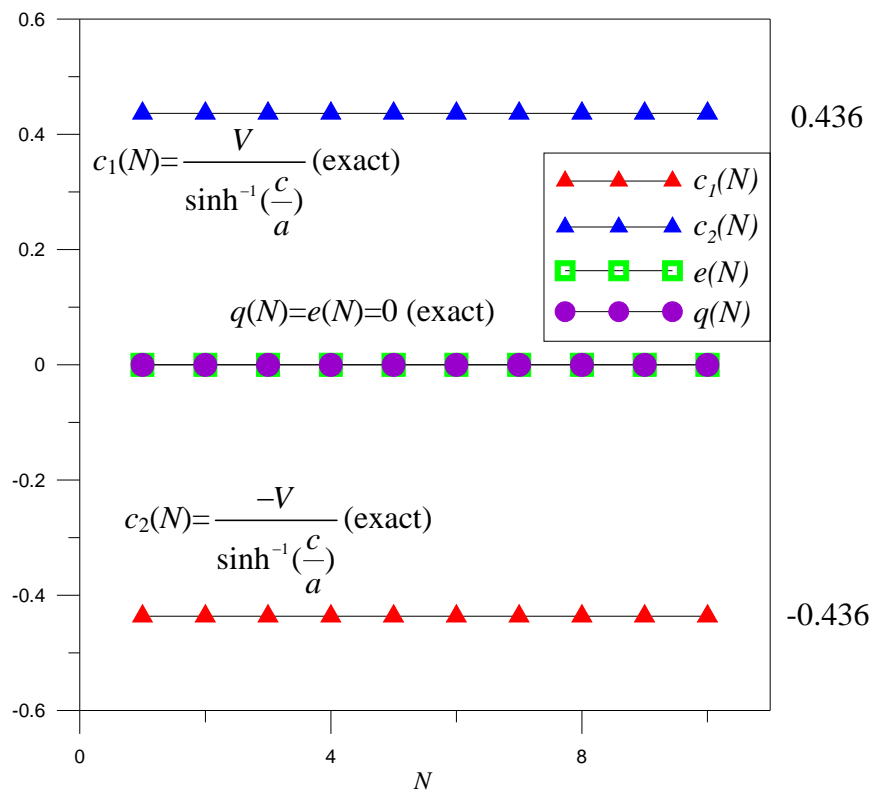
Figure 4-15 Coefficients of $q(N)$, $c_1(N)$, $c_2(N)$ and $e(N)$ versus N for an infinite plane with two circular holes.
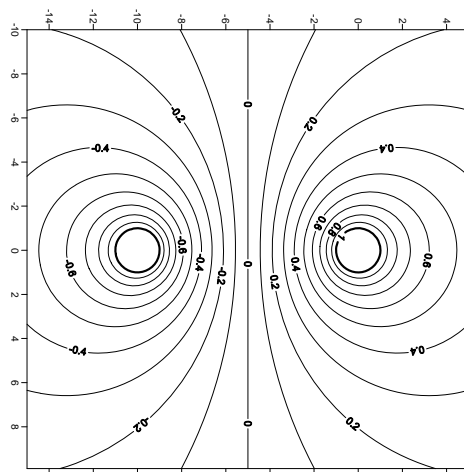
(a) an image solution
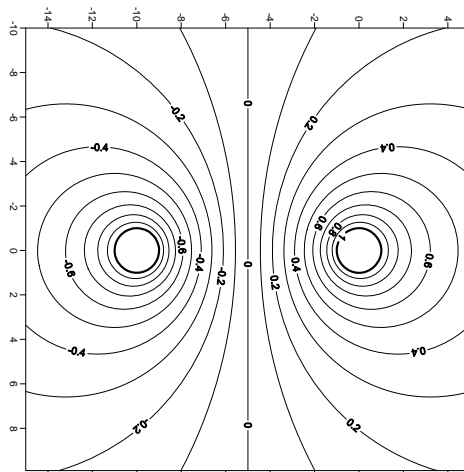
(b) an analytical solution using the bipolar coordinates
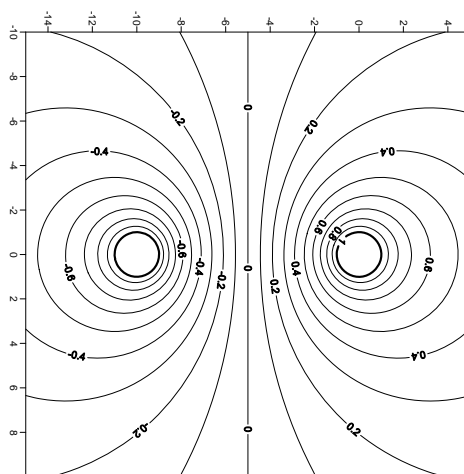
(c) a solution by using the null-field BIEM

Figure 4-16 Potential contours (a) an image solution (b) an analytical solution using the bipolar coordinates and (c) a solution by using the null-field BIEM [16].
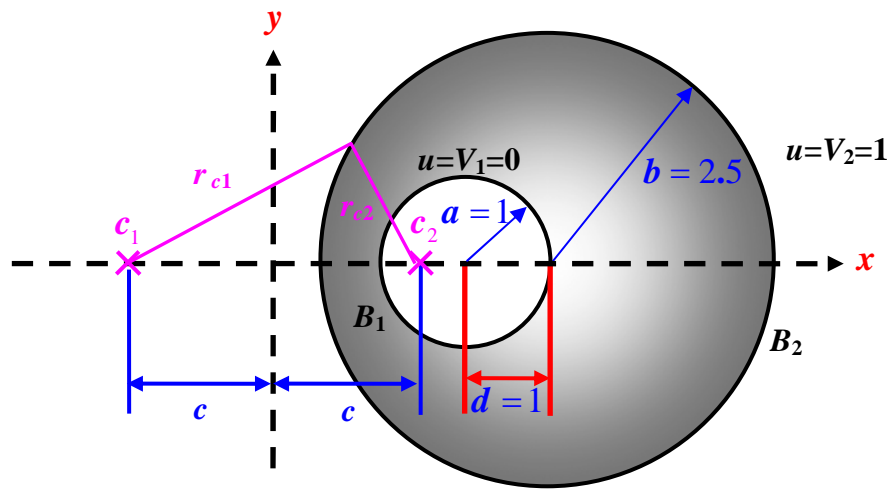
Figure 4-17 Problem sketch for an eccentric annulus.
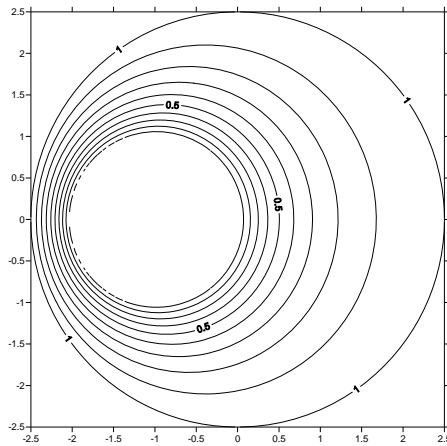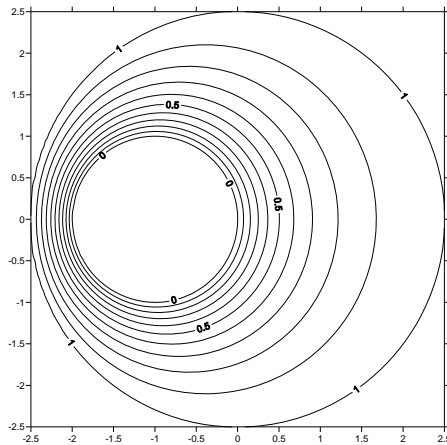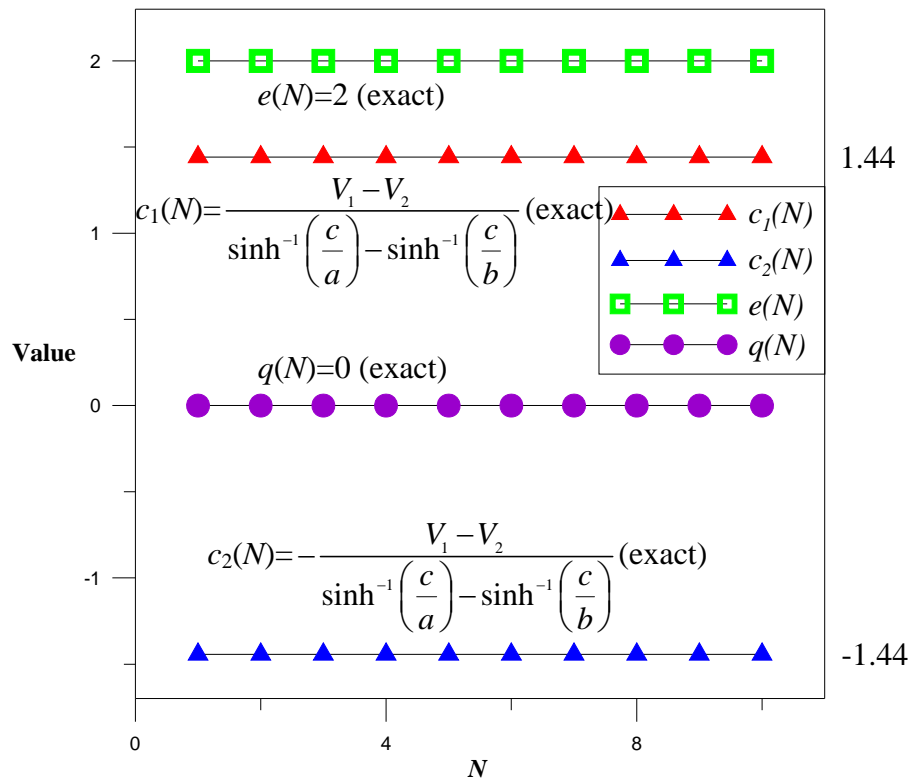

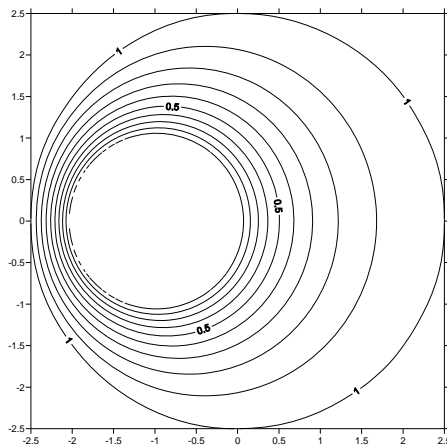Figure 4-18 Coefficients of $q(N)$, $c_1(N)$, $c_2(N)$ and $e(N)$ versus N for the eccentric annulus.
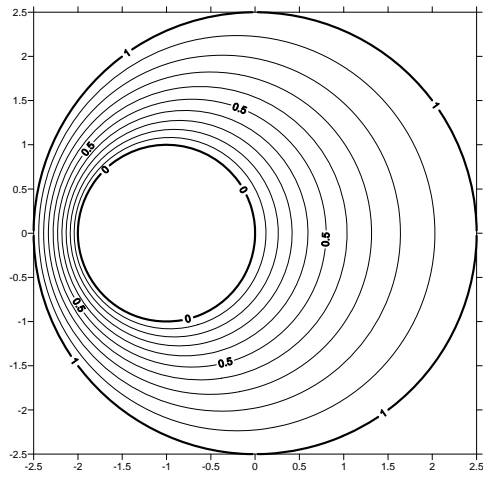
(a) an image solution
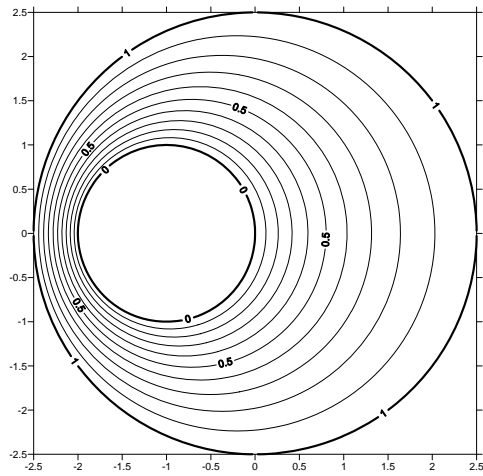
(b) an analytical solution using the bipolar coordinates
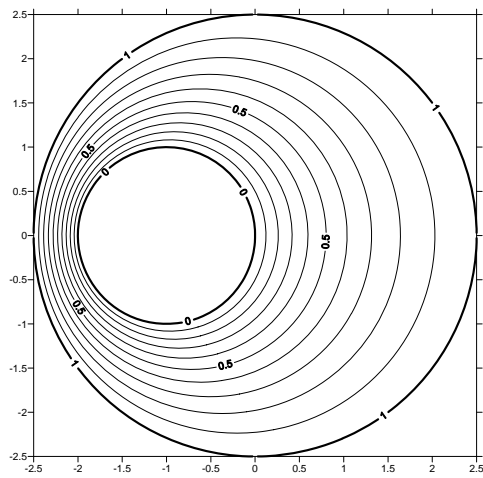
(c) a solution by using the null-field BIEM

Figure 4-19 Potential contours (a) an image solution, (b) an analytical solution using the bipolar coordinates and (c) a solution by using the null-field BIEM [17].

Chapter 5 Conclusions and further research

5.1 Conclusions

The thesis is concerned with the derivation of Green's function and boundary value problems (BVPs) for Laplace equation with circular holes or spherical cavities by using the image method and addition theorem. In the context of this thesis, we have demonstrated that our approach is efficient and effective. Based on the proposed formulation for solving the problems involving circular and/or spherical boundaries, some concluding remarks are drawn below:

1. Numerically speaking, the image method can be seen as a special method of fundamental solution (MFS) since the image singularities locate outside the domain. The optimal location and the strength of source in the MFS can be easily determined by using the image method.

2. In the chapter 2, two frozen images for the three cases, an eccentric annulus, a half plane with a circular hole and an infinite plane with two circular holes are found to be the focuses of the bipolar coordinate system passing the two circles.

3. Regarding the exterior problem subject to the Neumann BC, an extra source at the center of hole is required and successive images also terminate at the two focuses.

4. The dimension of the matrix in the linear algebraic equation is at most four by four in all the examples. Agreement is made after comparing with the results of MFS.

5. In the 3-D case, the weighting of image source can be determined by using the degenerate kernel for interior and exterior problems as shown in Table 2-1.

6. The Green's functions of annular case and concentric sphere can be obtained by

76

using the image method and the Trefftz method. The mathematical equivalence between the solutions derived by using the Trefftz method and the MFS was proved in Chapter 3.

7. It is found that the convergence rate of image method is better than those of Trefftz method and conventional MFS in the concentric sphere case.

8. We derived the Green's function for the 2-D and 3-D Laplace problems by using the image method and addition theorem. Also, the present approach can be utilized to construct boundary value problems (BVPs) without sources for problems with circular or spherical boundaries. The present method is seen as a "semi-analytical" approach since the unknown coefficient in the image method needs to be solved by using linear algebraic system.

9. The symmetric and anti-symmetric solutions for the two and three dimensional BVPs were obtained by using the image method in Chapter 4. For the 3-D case, we have found the strengths of the two initial sources at the two centers that can be determined in advance. The final strengths at the two strengths of frozen images approach zero if the number of images becomes infinite. Nevertheless, the 2-D case is not the same as 3-D case. An example of only two frozen images can construct the exact solution of 2-D BVP. This solution happens to be the Lebedev et al.'s solution by using the bipolar coordinates.

10. A program for deriving the Green's function due to the concentrated source for problems with one or two circular or spherical boundaries involving the Dirichlet and Neumann boundary conditions was developed.

5.2 Further research

In this thesis, our formulation has been applied to derive the Green's function for the concentrated forces and BVPs with circular or spherical boundaries by using the addition theorem and the image method. However, several issues need further investigation as follows:

1. Although the Green's function for the concentrated source was solved by using the image method, we may also employ the image method to solve the screw dislocation problems in the future study.

2. The degenerate kernels are expanded in the polar and spherical coordinates for problems with circular and spherical boundaries, respectively. For boundary value problems with an elliptical hole, further investigation should be done.

3. According to our successful experiences in the image solution for Laplace problems, extension to the Helmholtz and Biharmonic problems may be possible.

4. Whether the image method can be employed to solve the Green's functions with inclusions is also future work. Extension to the Robin BC may be considered.

5. In this thesis, we focus on Green's function and boundary value problem of two circular boundaries. The image solution may be extended to more than three circular boundaries problem. The focuses of any two circular boundaries may provide the optimal location of MFS.

References

[1] Ang W. T. and Kang I., 2000, A complex variable boundary element method for elliptic partial differential equations in a multiply-connected region, *Int. J. Comput. Math.*, Vol. 75, pp. 515－525.

[2] Antunes P. R. S., 2008, The Method of Fundamental Solutions applied to the eigenproblems in partial differential equations, Ph.D. Dissertation, IST, Portugal.

[3] Barnes R. and Jankovic I., 1999, Two-dimensional flow through large numbers of circular inhomogeneities, *J Hydrol*, Vol. 226, pp. 204－210.

[4] Barone M. R. and Caulk D. A., 1982, Optimal arrangement of holes in a two-dimensional heat conductor by a special boundary integral method, *Int. J. Numer. Methods Eng.*, Vol. 18, pp. 675-685.

[5] Blacerzak M. J. and Raynor S., 1961, Steady state temperature distribution and heat flow in prismatic bars with isothermal boundary conditions, *Int. J. Heat Mass Transfer.*, Vol. 3, pp. 113-125.

[6] Bogomolny A., 1985, Fundamental solutions method for elliptic boundary value problems. *SIAM J Numer Anal*, Vol. 22, no. 4, pp. 644-669.

[7] Brunskog J., 2005, Image solution for clamped finite beams, *J. Sound Vib.*, Vol. 287, pp. 1057-1064.

[8] Carrier G. F. and Pearson C. E., 1976, Partial Differential Equation-Theory and Technique, New York: Academic Press, pp. 68-71.

[9] Caulk D. A., 1983, Analysis of elastic torsion in a bar with circular holes by a special boundary integral method, *J. Appl. Mech.*, Vol. 50, pp. 101-108.

[10] Chen J. T. and Chen K. H., 1998, Dual integral formulation for determining the acoustic modes of a two-dimensional cavity with a degenerate boundary, *Eng. Anal. Bound. Elem.*, Vol. 21, No. 2, pp. 105-116.

[11] Chen J. T., Chou K. H. and Kao S. K., 2009, Derivation of Green's function using addition theorem, *Mech. Res. Commun.*, Vol. 36, pp. 351-363.

[12] Chen J. T., Lee J. W. and Shieh H. C., 2009, A Green's function for the domain bounded by non-concentric spheres, Submitted.

[13] Chen J. T., Shieh S. C., Lee J. W. and Lee Y. T., 2009, Image method and method of fundamental solution with optimal location of sources, submitted.

[14] Chen J. T., Lee Y. T., Yu S. R. and Shieh S. C., 2009, Equivalence between Trefftz method and method of fundamental solution for the annular Green's function using the addition theorem and image concept, *Eng. anal. bound. elem.*, Vol. 33, pp. 678-688.

[15] Chen J. T., Shieh H. C., Tsai J. J. and Lee J. W., 2009, Equivalence between Trefftz method and method of fundamental solutions for the Green's function of concentric spheres using the addition theorem and image concept, Submitted.

[16] Chen J. T. and Shen W. C., 2009, Null-field approach for Laplace problems with circular boundaries using degenerate kernels, *Numer. Methods Partial Differ. Equ.*, Vol. 25, no. 1, pp. 63-86.

[17] Chen J. T., Tsai M. H. and Liu C. S., 2009, Conformal mapping and bipolar coordinate for eccentric Laplace problems, *Comput. Appl. Eng. Educ.*, in Press.

[18] Chen J. T. and Wu C. S., 2006, Alternative derivations for the Poisson integral formula, *Int. J. Math. Educ. Sci. Technol.*, Vol. 37, pp. 165-185.

[19] Chen J. T., Wu C. S., Lee Y. T. and Chen K. H., 2007, On the equivalence of the Trefftz method and method of fundamental solutions for Laplace and biharmonic equations, *Comput. Math. Appl.*, Vol. 53, pp. 851–879.

[20] Chen K. H., Chen J. T., Chou C. R. and Yueh C. Y., 2002, Dual boundary element analysis of oblique incident wave passing a thin submerged breakwater, *Eng. Anal. Bound. Elem.*, Vol. 26, pp. 917-928.

[21] Chen T. and Weng I. S., 2001, Torsion of a circular compound bar with imperfect Interface, *Journal of Applied Mechanics*, Transactions of the ASME, Vol. 68, pp. 955-958.

[22] Cheng D. K., 1989, Field and wave electromagetics, Addison-Wesley.

[23] Cheng H. and Greengard L., 1997, On the numerical evaluation of electrostatic field in dense random dispersions of cylinders, *J. Comput. Phys.*, Vol. 136, pp. 629-639.

[24] Chou S. I., 1997, Stress field around holes in antiplane shear using complex variable boundary element method, *ASME J. Appl. Mech.*, Vol. 64, pp. 432－435.

[25] Courant R. and Hilbert D., 1953, Method of Mathematical Physics, Interscience, New York.

[26] Craggs J. W., 1946, The determination of capacity for two-dimensional system of

cylindrical conductors, *Q. J. Math.*, Vol. 17, pp.131-137.

[27] Greenberg M. D., 1971, Application of Green's functions in science and engineering, Prentice-Hill, New Jersey.

[28] Heyda J. F., 1959, A Green's function solution for the case of laminar incompressible flow between non-concentric cylinders, *J. Franklin Inst.*, Vol. 267, pp. 25-34.

[29] Honein E., Honein T., and Herrmann G., 1992, Further aspects of the elastic field for two circular inclusions in antiplane elastostatics, *ASME J. Appl. Mech.*, Vol. 59, pp. 774－779.

[30] Honein E., Honein T., and Herrmann G., 1992, On two circular inclusions in harmonic problem, *Q. Appl. Math.*, Vol. 50, pp. 479－499.

[31] Honein E., Honein T. and Herrmann G., 2000, Energetics of two circular inclusions in anti-plane elastostatics, *Int. J. Solids. Struct.*, Vol. 37, pp. 3667－3679.

[32] Hutchinson J. R., 1985, An alternative BEM formulation applied to membrane vibrations, Boundary Elements VII (Eds. C. A. Brebbia and G. Maier), Berlin: Springer.

[33] Hutchinson J. R., 1988, Vibration of plates, Boundary X (Ed. C. A. Brebbia), Berlin: Springer.

[34] Hutchinson J. R. and Wong G. K. K., 1979, The boundary element method for plate vibrations, Proceedings of the ASCE 7th Conference on Electronic Computation, St. Louis, Missouri., New York, ASCE, pp. 297-311.

[35] Jankovic I. and Barnes R., 1999, Three-dimensional flowthrough large numbers of spheroidal inhomogeneities, *J. Hydrol*, Vol. 226, pp. 224－233.

[36] Jaswon M. A. and Symm G. T., 1977, Integral equation methods in potential theory and electrostatics, Academic Press, New York.

[37] Karageorghis A. and Fairweather G., 1999, The method of fundamental solutions for axisymmetric potential problems, *Int. J. Numer. Methods Engng.*, Vol. 44, pp. 1653-1669.

[38] Keller J. B., 1953, The scope of the image method, *Commun. Pure Appl. Math.*, Vol. 51, pp. 505-512.

[39] Keller J. B., 1979, Progress and prospects in the theory of linear wave propagation, *SIAM J. Numer. Anal.*, Vol. 21, No. 2, pp. 229-245.

[40] Kita E. and Kamiya N., 1995, Trefftz method: an overview, *Adv Engng. Softw.*, Vol. 24, pp. 3-12.

[41] Kupradze V. D., 1964, A method for the approximate solution of limiting problems in mathematical physics, *Comput. Math. Math. Phys.*, Vol. 4, pp. 199-205.

[42] Lafe O. E., Montes J. S., Cheng A. H. D., Liggett J. A. and Liu P. L. F., 1980, Singularity in Darcy flow through porous media, *J Hydraulic Div*, Vol. 106, pp. 977-997.

[43] Lebedev N. N., Skalskaya I. P. and Uflyand Y. S., 1979, Worked Problems in Applied Mathematics, Dover Publications, New York.

[44] Lee D. K., 2000, Image singularity system to represent two circular cylinders of different diameter, *ASME J. Fluids Eng.*, Vol. 122, pp. 715－719.

[45] Lee Y. T. and Chen J. T., 2008, Analysis of two-spheres radiation problems by using the null-field integral equation approach, 32nd National conference on theoretical and applied mechanics, Taiwan.

[46] Li Z. C., Lu T. T., Hu H. Y. and Cheng A. H. D., 2007, Trefftz and collocation methods. Boston-Southampton: WIT Press.

[47] Ling C. B., 1947, Torsion of a circular tube with longitudinal circular holes, *Q. J. Math.*, Vol. 5, pp.168-181.

[48] Melnikov Y. A., 1977, Some application of the Greens' function method in mechanics, *Int. J. Solids Struct.*, Vol. 13, pp. 1045-1058.

[49] Melnikov Y. A. and Arman A., 2001, The fields of potential generated by a point source in the ring-shaped region, *Math. Engng. Ind.*, Vol. 8, no. 3, pp. 223-238.

[50] Mills R. D., 1977, Computing internal viscous flow problems for the circle by integral methods, *J. Fluid Mech.*, Vol. 73, pp. 609-624.

[51] Morse P. M. and Feshbach H., 1953, Method of Theoretical Physics, PartⅠ, McGraw-Hill, New York.

[52] Muskhelishvili N. I., 1953, Some basic problems of the mathematical theory of elasticity, Noordhoff: Groningen, pp. 175-179.

[53] Riley K. F., Hobson M. P. and Bence S. J., 2006, Mathematical methods for physics and engineering, Cambridge, New York.

[54] Schaback R., 2007, Adaptive numerical solution of MFS systems. A plenary talk at the first Inter Workshop on the Method of Fundamental Solution, Ayia Napa,

Cyprus, June 11-13.

[55] Sometani T., 2000, Image method for a dielectric plate and a point charge, *Eur. J. Phys.*, Vol. 21, pp. 549-554.

[56] Terras R., 1980, Image methods for constructing Green's functions and eigenfunctions for domains with plane boundaries, *J. Math. Phys.*, Vol. 21, no. 8, pp. 2140-2153.

[57] Thomson W., 1848, Maxwell in his treatise, quotes a paper in the Cambridge and Dublin Math. Journal of 1848, Vol. I., Chap. XI.

[58] Timoshenko S. P. and Goordier J. N., 1972, Theory of Elasticity, New York: McGraw-Hill, pp. 196-202.

[59] Wu M. S. and Wang H. Y., 2007, Solutions for edge dislocation in anisotropic film-substrate system by the image method, *Mathematics and Mechanics of Solids : MMS*, Vol. 12, pp. 183-212.

作者簡歷

中文姓名：謝宏治(謝祥志)

英文姓名：Hung-Chih Shieh

出生日期：民國 73 年 04 月 21 日

籍　　貫：台灣省桃園縣

聯絡地址：桃園縣平鎮市湧豐里 2 鄰中豐路山頂
　　　　　段 90 巷 29 號

聯絡電話：(03) 4690962

行動電話：0928751657

電子信箱：*M96520027@mail.ntou.edu.tw*

學　　歷：

　　　國立台灣海洋大學河海工程研究所碩士 (2007.09 ~ 迄今)

　　　國立宜蘭大學土木工程學系學士 (2004.09 ~ 2007.06)

　　　國立宜蘭技術學院土木工程學系 (1999.09 ~ 2004.06)

著作目錄：

(A) 期刊論文

1　Chen J. T., Lee Y. T., Shieh S. C., (2009): Revisit of two classical elasticity problems by using the Trefftz Method, Engineering Analysis with Boundary Elements, Vol. 33, pp. 890-895.

2　Chen J. T., Lee Y. T., Yu S. R., Shieh S. C., (2009) Equivalence between Trefftz method and method of fundamental solution for the annular Green's function using the addition theorem and image concept, Engineering Analysis with Boundary Elements, Vol. 33, pp. 678-688.

3　Chen J. T., Lee Y. T., Shieh H. C., (2009): Image method and method of fundamental solution with optimal location of sources, Submitted.

4　Chen J. T., Shieh H. C., Lee Y. T., Lee J. W., (2009): Bipolar coordinates, image method and the method of fundamental solutions for Green's functions of Laplace problems with circular boundaries, Submitted.

5　Chen J. T., Shieh H. C., Lee Y. T., Lee J. W., (2009): Image solutions for boundary value problems without sources, Submitted.

6　Chen J. T., Lee J. W., Shieh H. C., (2009): A Green's function for the domain bounded by non-concentric spheres, Submitted.

7　Chen J. T., Shieh H. C., Tsai J. J., Lee J. W., (2009): Equivalence between Trefftz method and method of fundamental solution for the Green's function of concentric spheres using the addition theorem and image concept, Submitted.

(B) 會議論文

1 Shieh, H. C.; Lee, Y. T.; Chen, J. T. (2008): Image method for the Green's functions of annulus and half-plane Laplace problems, 垚淼研討會, 宜蘭大學.

2 Shieh H. C., Lee Y. T., Yu S. R., Chen J. T. (2008): A linkage of Trefftz method and method of fundamental solutions for annular Green's functions using addition theorem, 32 屆力學會議, 嘉義中正大學.

3 Chen J. T., Shieh H. C., Tsai J. J., Lee J. W., Equivalence between Trefftz method and method of fundamental solution for the Green's function of concentric spheres using the addition theorem and image concept, BEM 31, New Forest, 2009